DESIGN, FABRICATION, AND ANALYSIS OF BROADLY TUNABLE ASYMMETRIC MULTIPLE QUANTUM WELL COUPLED CAVITY DIODE LASERS.

By

FERDOUS KARIM KHAN

A Thesis

Submitted to the School of Graduate Studies

in Partial Fulfillment of the Requirements

for the Degree

Doctor of Philosophy

McMaster University

BROADLY TUNABLE AMQW
COUPLED CAVITY DIODE LASERS

DOCTOR OF PHYLOSOPHY (2010) McMaster University

(Engineering Physics) Hamilton, Ontario

TITLE: Design, Fabrication, and Analysis of Broadly Tunable Asymmetric Multiple Quantum Well Coupled Cavity Diode Lasers.

AUTHOR: Ferdous Karim Khan.

M.Sc. (University of Ulm, Germany)

B.Sc. (Chittagong University of Engineering and Technology, Bangladesh)

SUPERVISOR: Professor Daniel T. Cassidy

NUMBER OF PAGES: XIII; 154

Abstract

A detailed analysis of coupled cavity semiconductor lasers with asymmetric multiple quantum well (AMQW) active regions is presented in this thesis. The analysis involved design, fabrication, characterization, and simulation of these devices. Although the coupled cavity devices can be multi sectioned, the devices discussed in this thesis are two sectioned.

A below threshold model for an AMQW coupled cavity device is developed. Non-linear fits of the below threshold spectral data to that obtained from the model were used to extract optimized device parameters. These fits helped to create an understanding of the operation of the devices and paved the way for improved device performance. Optimized device parameters obtained from the below threshold model were later used as input parameters in the development of an above threshold model. This model verified the wavelength selection mechanism employed by coupled cavity diode lasers and predicted the longitudinal modes for sets of injection currents.

Optical coherence tomography (OCT) is an application where much interest has recently been drawn. The coupled cavity devices fabricated in this work applied with proper modulation of the injection currents and followed by subsequent time averaging have demonstrated short coherence length (~15 μm) and can be an excellent source for synthesized OCT. Rapid wavelength switching (~70 ns, the measurement was limited by detector response time) over the whole range has also been experimentally shown. Because of the high speed (relative to mechanical) wavelength switching ability, AMQW coupled cavity devices have the potential for applications requiring real time measurements including real time synthesized OCT.

Acknowledgements

The past few years of my study here at McMaster was great. I need to thank a lot of people who helped me finish this huge task. I owe to so many people that a proper acknowledgement for all of them would require a large chapter.

The first person that comes into my mind whom I should acknowledge my gratitude is my supervisor Dr. Daniel T. Cassidy for his time, expertise, encouragement, moral support and enthusiasm. He was always there whenever I had a question and never backed away from guiding me to the right direction. He has given me the confidence when I needed it and I cannot imagine a better mentor for graduate studies.

Special thanks to Doug Bruce for taking his time in those long discussions and helping me with various issues related to the experimental set ups. Thanks to Dr. Zhilin Peng and Doris V. Stevanovic for training me with the clean room facilities and the related safety procedures. Thanks to Graham Pearson for helping me with the PL measurements and lending me equipments whenever I needed them.

Thanks to Maxim Poirier from CMC, Canada for his assistance with the CVD growth of the laser structures and the help he provided in the optical mask design. Dr. Brad J. Robinson also deserves some special appreciation for the excellent MBE growth of the laser structures.

I owe a great deal to Dr. Jingcong Wang for helping me with many issues. She had been like a sister to me. Thanks to my other lab mates Hesham M. Enshasy, Dr. Huiling Wang, Chadwick Hall and Jia Huiwen for their constant support. They always extended their helping hands when necessary.

Thanks to Dr. LaPierre and Dr. Xu, my other committee members for their time, effort and suggestions that helped me move along the right direction.

My parents deserve a lot of credit. Their encouragement and respect for education have helped me travel this far.

Finally, the biggest thanks goes to my wife Razia Sultana for her unconditional support during the whole time. Thanks for believing in me.

Table of contents

List of figures

List of Tables

1. Introduction

This thesis is concerned with the design, fabrication, and testing of coupled cavity InGaAsP/InP AMQW semiconductor diode lasers. Coupled cavity AMQW lasers are broadly tunable and are wavelength agile, which means the output wavelengths can be rapidly switched over a broad range of wavelengths. My major contributions to this field are twofold: I developed a below threshold model for two section coupled cavity lasers taking into account the non verticality of the gap facets. In addition, I also have experimentally demonstrated the ~100 nm wide tuning together with the high speed wavelength switching ability of these lasers. These simulation results as well as experimental data are summarized in two publications[1, 2]. This thesis starts with a brief introduction of wavelength agile tunable lasers. In this chapter, I discuss the types of wavelength agile tunable lasers, their pros and cons, and the various tuning mechanisms they adopt. The advantages of coupled cavity tunable semiconductor lasers over other tunable devices are also discussed.

1.1. Wavelength agile and tunable lasers

A tunable laser can be tuned to different lasing wavelengths discretely or continuously within a range mainly determined by the composition of the active

region material and the length of the laser. Agility of these tunable lasers is defined by their rapid wavelength switching ability. There are many types and categories of tunable lasers with gain media of gas, liquid, or solid state. Excimer lasers[3], $C0_2$ lasers[4], free electron lasers[5], dye lasers[6] (liquid and solid state), transition metal solid state lasers[7], and semiconductor diode[8] lasers are examples of tunable lasers. Here I restrict the discussion to different forms of tunable semiconductor diode lasers.

Realization of wavelength tunable semiconductor diode lasers became an important issue in the early 1980s after the successful development of InGaAsP/InP single mode laser diodes with emission wavelengths around 1300 nm and 1550 nm. Increased demand on transmission capacity in optical communication systems was the main driving force behind the ongoing research with advanced transmission-receiving techniques, with wavelength division multiplexing (WDM) and coherent optical detection techniques being the main focii[9]. All these advanced communication techniques require single mode wavelength tunable diode lasers on both transmitting[10] and receiving[11] sides. Besides optical communication, tunable diode lasers have numerous applications in bio-chemical sensing[12], spectroscopy[13], and distance measurements[14].

1.2. Basic wavelength tuning mechanism

A Fabry-Perot (FP) laser can be pictured as an amplifying medium bounded by two plane–parallel reflectors of reflectance *R*. The distance between the reflectors is termed the length of the laser. Center wavelengths of the longitudinal modes that can fit into this cavity are given by

$$\lambda_m = 2n_{eff}L/m \tag{1.1}$$

where n_{eff} is the effective refractive index, *L* is the cavity length, and *m* is an integer denoting the longitudinal mode number. The magnitudes of the m^{th} mode intensities at the surfaces of the symmetric FP resonator are[15] calculated as

$$I_m^{\pm} = \frac{\left\langle |\delta_m|^2 \right\rangle}{1 - RG_m} \tag{1.2}$$

where $\langle|\delta_m|\rangle^2$ is the total amount of spontaneously emitted light coupled into the m^{th} mode and G_m is the single pass gain of the m^{th} mode and is defined as[16]:

$$G_m = \exp\left[\frac{g_m NL - 2g_m \sum_i \frac{\delta_i}{g_i}\left[I_i^+(z) - I_i^+(0) + I_i^-(0) - I_i^-(z)\right]}{S - 2\sum_i \sigma_i c_i}\right] \tag{1.3}$$

In Eq. 1.3 g_m is the gain coefficient of the amplifying medium, *N* is the pumping rate per unit length, *S* is the saturation intensity, taken as the inverse of the total lifetime of the upper state, σ_m is the line shape factor of the m^{th} mode, and c_m expresses the coupling of the spontaneous light in the m^{th} mode.

From the denominator of Eq. 1.2 it is evident that $RG_m \approx 1$ will cause I_m to have a very large value which denotes the onset of lasing operation. This condition ($RG_m \approx 1$) is termed as the laser threshold condition. By changing either R, G_m, or both, the mode reaching threshold can be controlled. Wavelength tuning of the laser is achieved as different modes reach threshold for different RG_m values. Material gain g_m which is the main contributor to the G_m is wavelength dependant and usually has a wide enough gain peak so that multiple longitudinal modes can lase simultaneously. Single mode operation can be achieved by making the mirror loss R wavelength dependant.

1.3. Widely tunable diode lasers

The amount of wavelength tuning required is application specific but in general, the more the better. Consider the application of optical communication where a tunable laser can be used as a transmitting source. Before the advent of tunable lasers, service providers used fixed wavelength lasers, which meant holding expensive inventory to support each wavelength. The overhead associated with the management of this inventory was difficult at all levels of the supply chain. Since wavelength activity could not be predicted, providers would often face supply storages for specific wavelengths, compromising the capacity of the network. Tunable lasers provide dynamic reconfigurability by allowing network operators to switch from one wavelength to another on demand, easing the cost of purchasing, storing, and managing

spare devices for wavelength management. Today, a tunable laser can cover hundreds of channels in a dense wavelength division multiplexing (DWDM) system. Tunable lasers can either be used as a universal source to support a particular application, or can be switched to support different wavelengths on demand.

Tunable lasers with at least a 30 nm tunable range are described as widely tunable[17]. These widely tunable lasers are very attractive components for application domains where the wavelength parameter provides an additional degree of freedom leading to functionality, increased performance, and flexible operation. Due to the advantages inherent to their use a great number of structures have been proposed over the years for a variety of applications. The key issues for wavelength agile widely tunable diode lasers are tuning range, side mode suppression ratio (SMSR), rapid wavelength scanning, and manufacturability.

Various widely tunable semiconductor lasers are available today and can be differentiated by the tuning mechanism adopted. Tunable semiconductor lasers can mainly be divided into two groups: (1) mechanically tunable lasers; and, (2) electronically tunable lasers. Mechanically tunable diode lasers are sub grouped into conventional external cavity diode lasers and micro-electro-mechanical systems (MEMS) tunable diode lasers.

1.3.1. Mechanically tunable diode lasers

In this scheme a tunable laser system consists of a semiconductor diode laser with one or more optical elements forming an external cavity. The tuning mechanism depends on the mechanical movement of the optical elements. A portion of the output light is fed back into the lasing cavity by the optical elements changing the phase and amplitude balance of light inside the cavity. Wavelengths with highest single pass gain-reflectivity (RG) product, when fed back into the cavity, will be enhanced further and become the enforced mode of the system.

1.3.1.1. External cavity tunable diode lasers

The first experiments on laser diodes coupled to an external cavity were reported in 1964 by Crowe and Craig[18] soon after the first successful demonstration of diode lasers. Tunable external cavity diode laser systems consist primarily of a semiconductor diode laser with or without antireflection coatings on the two facets, a collimator for coupling the output of the diode laser, and an external mode selection filter. The coupling of a diode laser to an external resonator affects the emission spectrum of the diode in addition to producing changes in threshold current and total output power. The length of the external cavity can be of long or short form and for both cases wavelength selectivity is obtained by the interference effects between the resonances of the laser cavity and the external cavities.

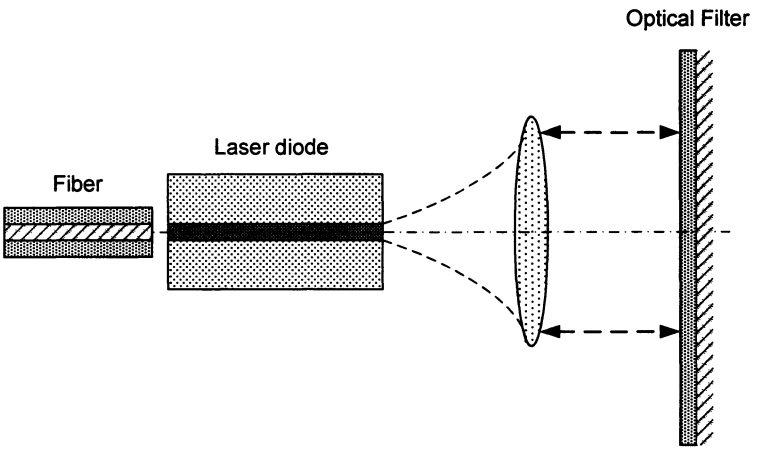

Figure 1-1 Schematic of an external cavity diode laser

Feedback in short external cavities is provided by a plane or a spherical mirror. The distance between the inner diode mirror and the external reflector has the same order of magnitude as the active region optical length[19]. Long external cavities are formed by one diode mirror, a lens system and a plane or spherical external mirror. The resonator length is typically one to two orders of magnitude larger than the length of the active region. A second possibility to produce wavelength selective loss is to replace the external mirror with a dispersive element like a reflection grating or a Fabry-Perot (FP) etalon. These approaches were first used by Edmonds and Smith[20] to achieve reduced spectral width. A non-dispersive element like a mirror presents little wavelength filtering to the laser beam and if there is no wavelength selection mechanism within the laser cavity, the output normally consists of multiple longitudinal modes. Competition between these longitudinal modes will eventually cause mode hopped wavelength tuning. Figure 1-1 shows a

schematic of an external cavity diode laser of the long form where the optical filter can be a dispersive element like a diffraction grating. The lens-grating combination in the long external cavity case can be replaced by a diffractive optical element (DOE)[21]. Both diffraction gratings and DOEs have wavelength selective reflectances. A DOE is more advantageous than a lens-grating combination because it replaces the angular rotation required for a grating by a simple linear motion and also eliminates the requirement of a lens. This creates the possibility of monolithic fabrication of a DOE external cavity tunable laser.

1.3.1.2. MEMS tunable lasers

MEMS tunable lasers are similar to external cavity tunable lasers except the optical elements in this case are miniature in size. The strong promise of miniaturization shown on optical elements like movable mirrors and rotary gratings led to tunable lasers with higher tuning speed compared to the conventional ones. MEMS technology also provides high compactness and batch fabrication capability. With the progress of fabrication capability from wet etching, surface micromachining to deep reactive ion etching (DRIE) together with MEMS photolithography processes, these devices have not only decreased in size but also improved their performance. Short external cavities varying from 100 μm to 10 μm have already been demonstrated[22]. Berger et al.[23] demonstrated a MEMS tunable diode laser using a rotary micro mirror

and a diffraction grating in a Littman[24] configuration. A 40 nm tuning range with a 55 dB SMSR was obtained. Littrow[24] and Littman schemes are most popular among MEMS tunable lasers and are schematically shown in Figure 1-2 and Figure 1-3. In the Littrow scheme, light is diffracted only once in the external cavity. The wavelength tuning is obtained by rotating the grating about a remote pivot. The Littman scheme has one more mirror compared to the Littrow scheme. Here the laser beam is diffracted twice in a roundtrip of the external cavity. In this case, the grating is fixed and the mirror is rotated about a remote pivot.

Although MEMS tunable lasers provide numerous advantages over conventional external cavity tunable laser diodes, it faces many technical challenges. For example, the optical quality of the micro machined mirrors/gratings is not comparable to conventional ones and three-dimensional (3D) optical structure fabrication is also very difficult using current MEMS technology[25]. Packaging and integration of the MEMS fabricated tunable lasers face extreme difficulties as not all the components used in the device, i.e., diode lasers, gratings, and lenses, are exactly monolithic and hence face problems in optical alignment. In addition, due to the movable micromechanical structures, they often face mechanical, electrical, and thermal stability/reliability problems[25].

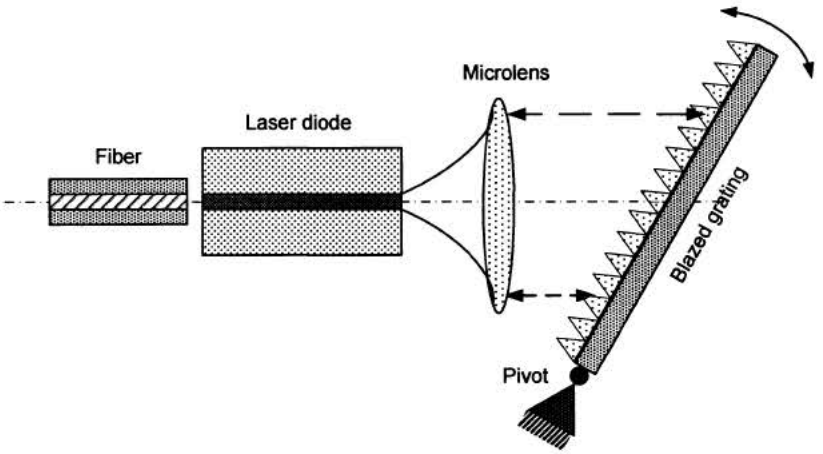

Figure 1-2 Schematic of MEMS tunable diode laser in Littrow configuration.

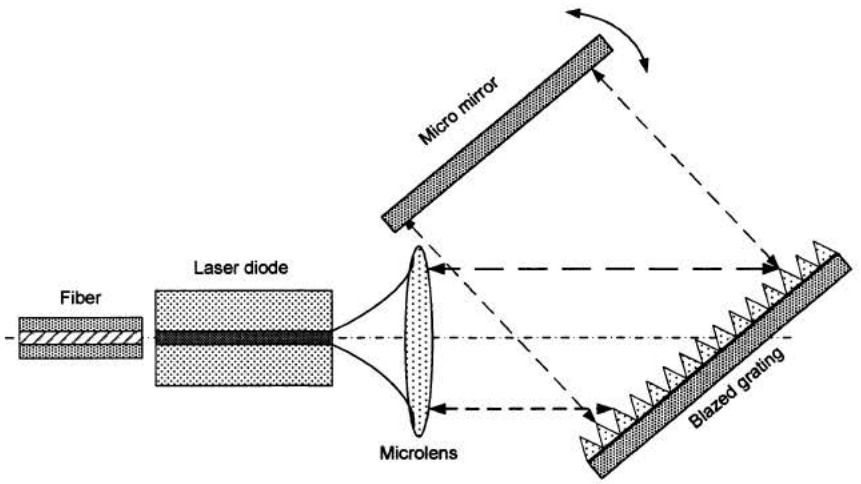

Figure 1-3 Schematic of MEMS tunable laser in Littman configuration.

Diode lasers operated in an external cavity configuration can provide both tunability and single mode emission but because of the bulky optical elements, broad wavelength scanning is only possible at a slow rate. For MEMS tunable lasers, there is a trade-off between tuning speed and tuning range. The speed of tuning is determined by the dimensions of the mechanical structure. The

maximum tuning speed of a MEMS tunable laser is directly proportional to stiffness and inversely proportional to the mass of the structure[26]. Since the maximum stiffness is a material property and cannot be changed, the mass of the mechanical structure needs to be reduced to increase the speed of tuning. For example, by decreasing the thickness of the micro actuator, a large increase in resonance frequency can be achieved. Recently[27], a high speed tunable MEMS vertical cavity surface emitting lasers (VCSEL) structure was demonstrated with a tuning speed of ~16 MHz but the tuning range was merely ~3 nm. Tunable edge emitting MEMS lasers are readily available from various sources with a maximum tuning range of ~40 nm but in this case the scanning speed is in the range of 50 Hz[28].

1.3.2. Electronically tunable lasers

From Eq. 1.1, it can be observed that the longitudinal mode positions can be shifted either by changing the length L or n_{eff} of the laser. In mechanically tuned lasers, the physical dimension L is changed by varying the position of the optical elements. For electronic tuning, n_{eff} is changed either by the application of a varying electrical field or by changing the injection current. Although the index change with the application of an electric field enables high speed tuning, the index shift is small[29] offering limited tuning range. Index change by changing injection carriers is the most frequent method used in wavelength tuning. Carriers injected into the waveguide by an external current

source reduce the effective index. The refractive index change due to the injected carriers into a semiconductor is due to the effects of free carrier absorption, band filling, and band-gap shrinkage[30]. Joule heating due to the injected current also causes a decrease of the bandgap and hence changes the refractive index. In addition, an injected carrier density also causes a refractive index change at the peak gain energy because of a strong asymmetric shape of the semiconductor gain curves and can be calculated with the Kramers-Kronig dispersion relations[31].

Several types of electronically tunable single mode lasers have been proposed over the years and put to operation. Since tunable lasers need to operate on a single mode from an application point of view, this qualifier will be dropped from now on. Distributed feedback (DFB) lasers, distributed Bragg reflector (DBR) lasers, and coupled cavity semiconductor lasers all employ electronic tuning of the cavity refractive index.

1.3.2.1. Distributed feedback (DFB) lasers

A DFB laser combines an active and grating region over the length of the laser cavity. A simple sketch of a DFB laser is shown in Figure 1-4. DFB lasers were originally developed as single mode lasers and were not intended for tunability. The transverse integration of the wavelength selective grating and gain functionality allows for relatively simple fabrication with no active/passive interface. In a periodically varying index grating, the reflection

coefficient for different modes will be wavelength dependant. Distributed feedback occurs at the wavelengths for which all the feedback or reflections from the grating add in phase. This is near the Bragg wavelength, which is given as

$$\lambda_B = 2n_{eff}\Lambda \tag{1.4}$$

where Λ is the grating pitch. The modes closest to the Bragg wavelength (λ_B) will have constructive reflection as they are in phase. Modes away from λ_B will be out of phase and will be suppressed.

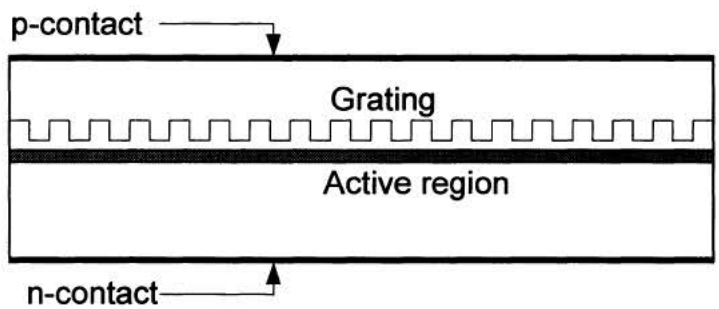

Figure 1-4 Schematic of a DFB laser.

Some of the first electronic tunable lasers were multi section DFB based with a complicated operation scheme having a very modest tuning range of ~3 nm[32]. Thermally controlled DFB tunable lasers were also proposed but they also offered 3-4 nm tuning range for a 30-40 °C temperature variation[33]. To increase the tuning range some vendors used a selective array of DFB lasers. Either optical coupling[34] or a MEMs mirror[35] was used to couple the light produced by each laser to an output fiber. The main problem of the former

technique is the power loss associated with the coupler and that of the latter, packaging an extra MEM device makes the fabrication complicated in addition to the slow wavelength switching speed caused by the MEM mirror.

1.3.2.2. Distributed Bragg reflector (DBR) laser

Like DFB lasers, DBR lasers were also originally intended as single frequency lasing sources. In its basic form, there is a grating instead of the cleaved facet at one or both ends of the laser structure. Figure 1-5 shows a schematic of a DBR laser with a grating at one end. Separate active and passive regions provide better control of the refractive index of each region which in term improves the wavelength tuning[8]. Much work has been done on tunable DBR lasers and the structure has been evolved from multisection form to more recent sampled grating DBR (SGDBR) lasers and super structure grating DBR (SSGDBR) lasers. While various research groups have reported tuning ranges of 40-60 nm, a high speed wavelength scanning of ~8 ns over 12 nm was also demonstrated[36]. The main drawback of this structure lies in the complex fabrication procedure. A device with a simpler fabrication process retaining all the virtues of DBR laser would be ideal.

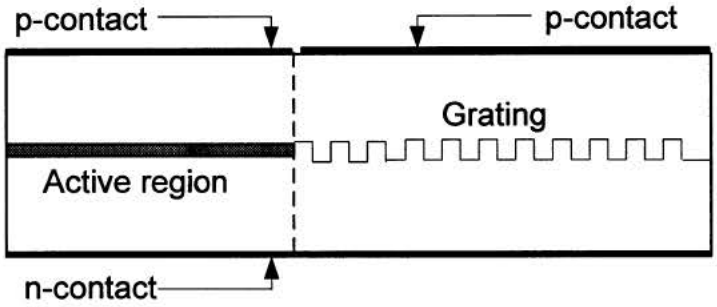

Figure 1-5 Schematic of a two section DFB laser.

1.3.2.3. Coupled cavity semiconductor laser

Coupled cavity lasers were also introduced as a single frequency source as single frequency lasers were receiving considerable attention in view of their potential for high speed optical communications system. The single longitudinal mode selection using a coupled cavity scheme was first shown[37] on gas lasers. Since then an extensive amount of work was carried out on semiconductor lasers coupled to an external cavity with several research groups involved in monolithically coupled cavity lasers. In the 1980s Bell labs patented the cleaved coupled cavity (C^3) laser[38] as a tunable single frequency source. The C^3 laser was never used commercially in optical communication systems as distributed feedback (DFB) lasers were ultimately developed and found to be better suited as single frequency sources and also because commercial production of C^3 lasers was not stable. DFB lasers possess a large side mode suppression ratio (SMSR) but the SMSR is achieved at the expense of tunability. There are applications where a diode laser is required

to be tuned over a broad range. Coupled cavity lasers have the potential to provide tunability together with wavelength stability. Early work[39] on coupled cavity lasers showed a wavelength tuning range of ~30 nm. A broader tuning range should be advantageous for applications like optical coherence tomography (OCT), wavelength division multiplexing (WDM), surface roughness measurement, speckle interferometry, and distance measurement, to name a few applications.

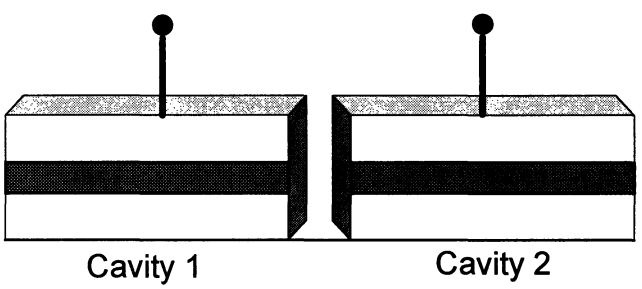

Figure 1-6 Schematic of a two section coupled cavity diode laser.

Due to the advancement of fabrication and etching techniques together with the need for a low cost, simple operation device for applications where wide tuning range is required, a rebirth of coupled cavity lasers has been observed. Several groups have reported working on coupled cavity diode laser structures of different forms and various emission wavelengths[40, 41, 42]. Figure 1-6 shows the schematic of a two section coupled cavity semiconductor laser. It consists of two laser cavities separated by an air gap. The sections

have separate electrical contacts allowing individual adjustment of the cavity refractive index and gain with a change of the injection current. Typically the air gap is of the order of the wavelength of operation of the coupled cavity laser. The planarity and parallelism of the facets of the air gap affect the operation of coupled cavity devices.

1.4. Thesis outline and objective

This thesis is organized into six chapters. Chapter 2 describes the design and fabrication procedures used by previous research groups and by me for the fabrication of coupled cavity semiconductor lasers. Asymmetric multiple quantum well (AMQW) active regions, which are used in the work reported in this thesis, are also described in brief. Chapter 3 introduces the below threshold transfer matrix model for the coupled cavity semiconductor lasers. This model takes into account the planarity and parallelism of the facets of the air gap and shows that the facet angles play an important role in the coupling between the sections and hence affect the operation of the laser. An above threshold simulation for AMQW coupled cavity semiconductor laser is described in Chapter 4. The model verified the tuning mechanism employed by a two section coupled cavity laser and indicates limits on the performance that can be expected from broadly tunable coupled cavity lasers. Chapter 5 describes the results of measurements on AMQW C^3 lasers. The possible application of this device as a broadly tunable source having a short time

averaged coherence length in optical coherence tomography (OCT) is also explored in this chapter. Finally, Chapter 6 contains the summary of the work reported in this thesis and some suggestions for future work.

2. Design and Fabrication of AMQW coupled cavity lasers

2.1. Introduction

In this chapter, the design and the fabrication of coupled cavity diode lasers with AMQW active regions are discussed. The design part of the work consists of designing layer structures, cavities, air gaps, and the electrodes. The fabrication part of the work includes the creation of the air gap between the two sections in a way that the two sections remain aligned.

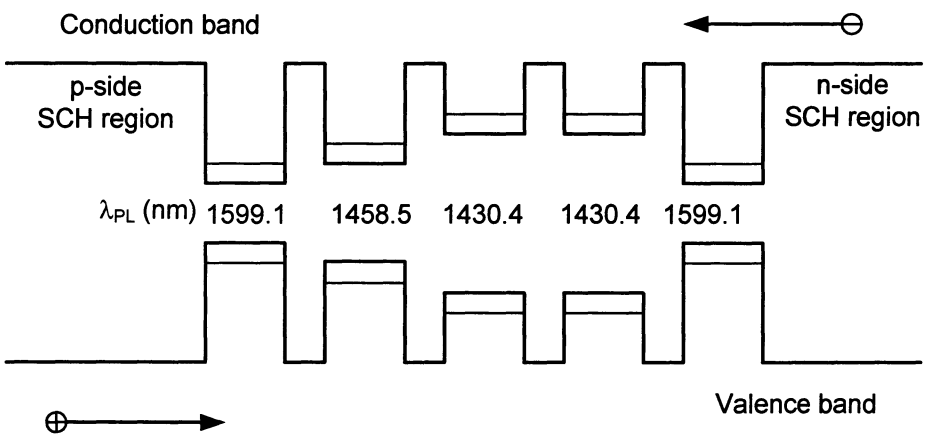

Figure 2-1 Energy profile of the active region of an AMQW laser

2.2. AMQW active region structure

The design and the optimization of AMQW lasers have been performed over the years in our group. Asymmetric QWs can be of two types, i.e. (1) dimensionally asymmetric QWs (DAMQWs), where the QWs in the active

region vary dimensionally; and, (2) compositionally asymmetric QWs (CAMQWs) where the QWs have varying composition. The advantage of using compositionally asymmetric structure lies in the fact that optical confinement factor and hence gain for short and long wavelength QWs remains similar. Optical gain for each longitudinal mode is a function of the optical confinement factor, which is defined as the overlap between optical modes and the quantum wells. Since the QWs for dimensionally asymmetric devices have different thicknesses, the optical confinement factor and hence the optical modal gain for each well will be different. Additionally, the use of DAMQW will need compensation of carrier capture and escape processes, which is a function of the well thickness.

CAMQW lasers with wells of 10 nm thickness separated by 5 nm barriers were used in the work reported in this thesis. Figure 2-1 shows the schematic energy profile of the active region of a CAMQW laser showing the energy levels of wells and the injection of electrons and holes. The wells used in this design have room-temperature photoluminescence (PL) peaks at 1599.1, 1458.5, 1430.4, 1430.4 and 1599.1 nm from the p-side to the n-side. Figure 2-2 shows the room temperature PL measurement of the molecular beam epitaxy (MBE) grown structure used in this work. PL peaks at 1426, 1458 and 1596 nm are clearly observable.

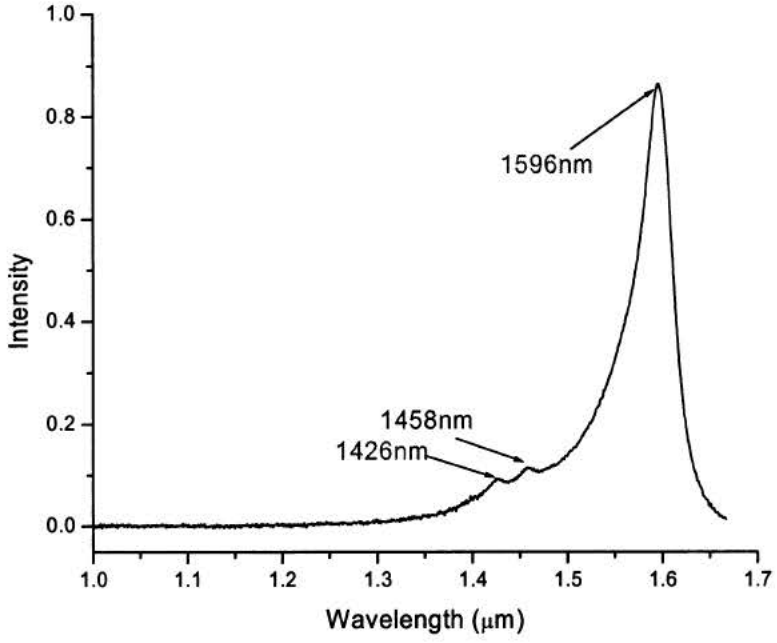

Figure 2-2 Experimental measurement of PL peaks for the AMQW structure.

2.3. Broad gain profile of AMQW structure

The broad tuning range provided by AMQW lasers is associated with a broad gain profile and more specifically, a broad and flat reflectance-gain (RG) product where R and G stand for facet reflectance and single pass cavity gain respectively. Each of the five QWs used in this AMQW layer structure possess a different gain characteristic and the resulting gain can yield a broad net gain curve[43]. This broad gain profile results in an improved wavelength tuning range compared with conventional QW or multiple quantum well (MQW) structures[44]. This improved tuning range is for lasers with no facet coatings.

Figure 2-3 shows the calculated individual gain characteristic for each well of this structure as well as the net gain profile. The compositions of the wells are chosen to provide a broad and flat gain peak. An eight band $k \cdot p$ Galerkin-based simulator[45, 46] was used in the design of the active region. The method takes into account coupling of the electron wave functions between the wells. Simple analytic solutions for the wave functions for each well are taken as basis functions. A weighted sum of these basis functions is the wave function of the entire structure.

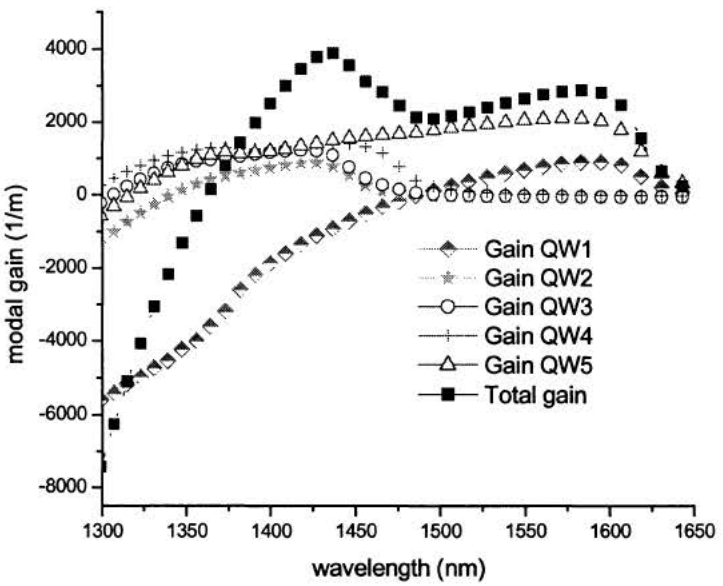

Figure 2-3 Calculated modal gain profile for an AMQW laser.

A partial layer structure of the devices used in this work is given in Table A-0-1 of Appendix A. Structures were grown using both MBE and metal organic chemical vapor deposition (MOCVD).

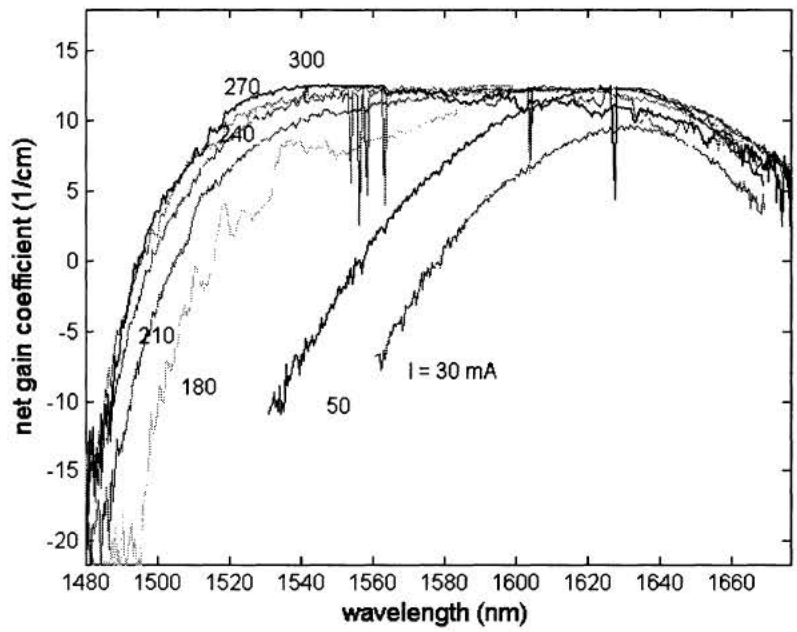

Figure 2-4 Measured net gain coefficient for the AMQW structure with various levels of injection current.

The measured net gain of a device with a cavity length of 900 μm for different values of injection current is shown in Figure 2-4. The method is based on a non-linear least square fitting of the measured Fabry-Perot modes to an Airy function[47]. Each mode that was measured with an optical spectrum analyzer (OSA) was fitted to extract gain-reflectance parameters. The influence of the OSA was taken into account by a convolution of the Airy

function with the response function of the OSA. For low injection current levels (I < 100 mA), only the long wavelength (i.e., red) wells are contributing to the gain while for higher injection currents (I ~ 200 mA), both the red and blue (i.e., short wavelength) wells have contributions to the net gain. As a result, a broad net gain profile can be observed for higher injection currents.

2.4. Design considerations

The design of the active region plays an important role in the performance of AMQW lasers. Wells near the p-side of the active region of InP/InGaAsP diode lasers are more populated with holes than wells near the n-side because of low hole mobility and the impeding effect of larger band discontinuities in the valence band compared to the conduction band. As a result, holes in InGaAsP/InP devices tend to be confined to the wells that are near the p-side, which leads to a large population difference and hence more gain for the p-side wells. This non uniformity of the carrier distribution in AMQW structures can be reduced by reducing the barrier thickness. Optimized layer thicknesses for the active region were obtained from simulation[46] and from experience. The simulations took into account the coupling between the wells and, on a phenomenological basis, the non uniform carrier injection. Experimentally, it was observed[48] that a reduction of the barrier thickness from 10 nm to 5 nm decreases the gain of the wells located near the p-side of the active region by 75%. Thus a more uniform carrier distribution is obtained with

5 nm barriers and this helps to obtain a spectrally flat and broad net gain curve.

2.5. Fabrication techniques for two section AMQW coupled cavity lasers

The devices used in this paper are two-sectioned coupled cavity AMQW InGaAsP/InP ridge waveguide (RWG) lasers. The basic idea behind the fabrication of these devices is to take a single cavity AMQW laser and etch a gap or to cleave at a certain position while bending/stretching afterwards to make the device have two optically coupled but electrically isolated sections. Fabrication of these devices started with the design of the isolated electrodes. An optical mask was designed for the fabrication of a laser with a single cavity having two electrically separated contacts. Figure 2-5 shows a schematic top view of an electrically isolated two section device. The dark gray portion in this figure is an isolation area where the InGaAs contact layer has been etched off after removing the metal, making it an electrically isolated two section device. The gap between the sections is formed at the intersection of the isolation etch and the ridge. The extension of metal on either side of the ridge is to facilitate wire bonding to the two sections. This is needed whenever the length of one of the sections is very small. Figure 2-6 shows a side view of the same device shown in Figure 2-5. More detailed screen shots of the mask are given in Figure B-1of appendix B.

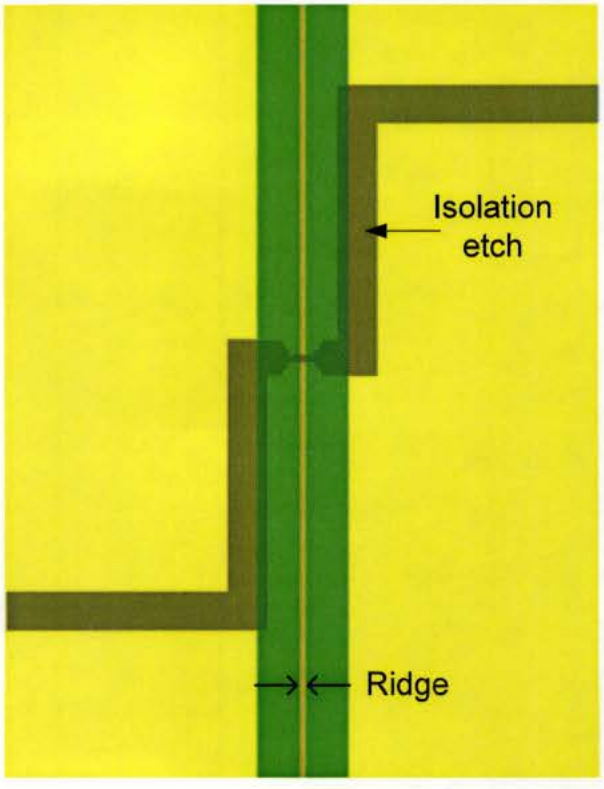

Figure 2-5 Top view of a two section isolated electrode design.

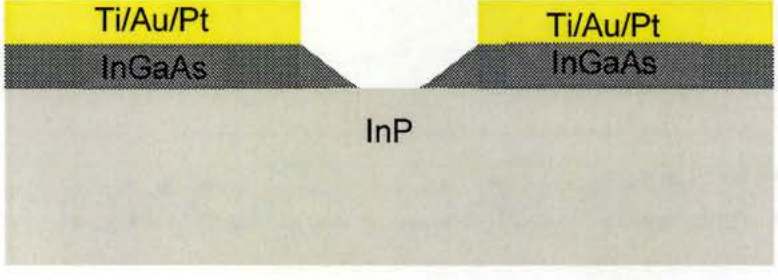

Figure 2-6 Side view of a two section isolated electrode design.

The next step after electrode isolation is to create the gap between the two sections. One method is to etch a gap between the sections. Coldren *et al.*[49] used wet chemical etching (WCE), reactive-ion-etching (RIE), crystallographic wet chemical etching (XWCE), and combinations of XWCE and RIE to etch grooves. While all the procedures were able to etch a groove, none of them produced vertical, mirror quality facets for the walls of the air gap. WCE produced mask undercuts, RIE produced rough wall surfaces (although recent improvements in inductively-coupled plasma (ICP) RIE lead to high quality facets[50]) and a single XWCE mix cannot etch the whole layer structure[49]. Focused ion beam (FIB) milling, which uses Ga^+ for removal of material, is advantageous because it is maskless with a direct writing capability on a sub-micron scale. Therefore, FIB coupled with *in situ* monitoring might be used as a straightforward way for sculpturing sub micron structures. However, energetic Ga^+ beams cause wall damage that affects the active region[51] and a completely vertical sidewall is somewhat difficult to obtain[52]. In the 1980s Tsang *et al.* fabricated cleaved coupled cavity (C^3) devices. Figure 2-7 describes the procedure. Thick Au pads about the size of the laser diodes were electroplated on the substrate side underneath the laser stripes but not in the regions where cleaves to create the facets were to be made. Laser bars were cleaved in the regions with no Au pad. These bars were then cleaved again to make the air gap and hence C^3 lasers. The thick Au pad held the two sections together and the gap could then be increased by

bending the sections back and forth. More recently, inductively coupled plasma reactive ion etching (ICP-RIE) is being used for etching laser facets. Smooth and vertical facets (side wall angles with respect to surface normals can be kept <1°) are obtained[53]. Both etching and cleaving procedures have their pros and cons. In this work both C^3 and FIB milled devices are investigated.

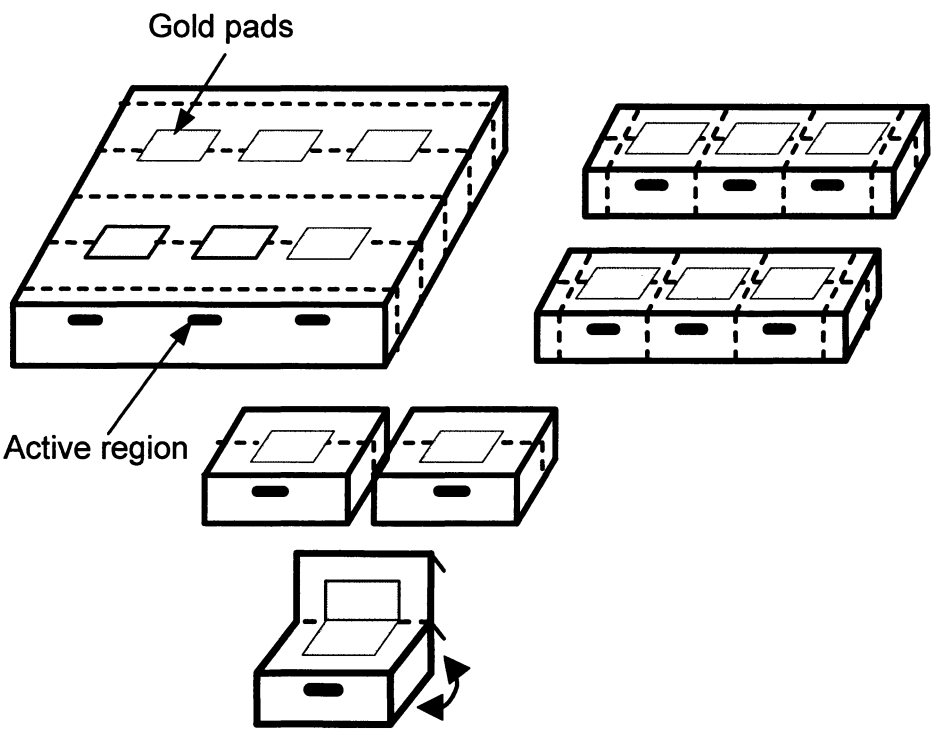

Figure 2-7 Fabrication procedure for cleaved coupled cavity lasers.

For the fabrication of C^3 lasers, I used a slightly different approach. Single section devices of defined cavity lengths were initially cleaved from the

wafer and bonded on thin flexible brass shim stock (nominal thickness of 25 μm) using a two component silver filled epoxy (Epo-Tek H20E), which has a high electrical conductivity and a short curing cycle. After spreading the epoxy on the shim stock, a single section device was placed on the epoxy. The shim stock along with the device was cured in an oven for 15 minutes at 120° C. A light scratch was made at one edge of the laser at the required length ratio and a bending moment was applied to the shim stock. Bending the sheet cleaves the single section device into a two section coupled cavity device and forms a 'V' shaped air gap between the sections as the metal does not bend back completely when the bending moment is removed. The metal sheet can be bent either way to change the width of the air gap.

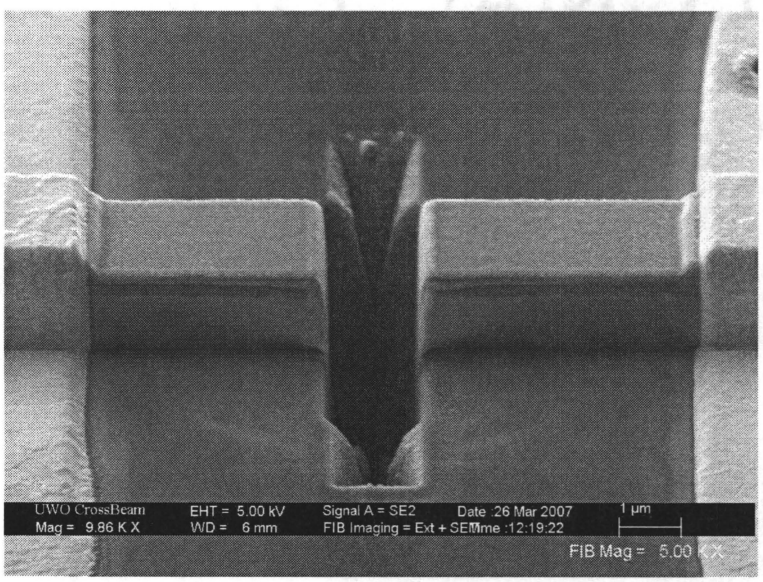

Figure 2-8 Top view of FIB milled air gap.

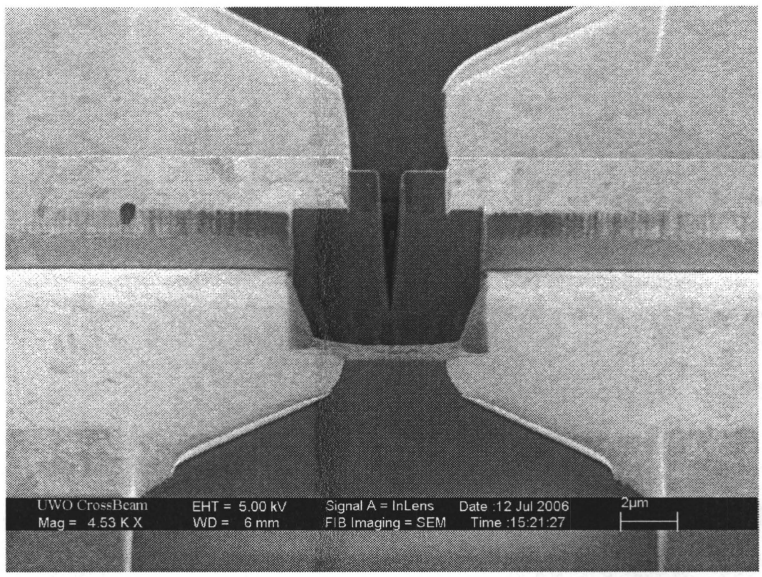

Figure 2-9 Cross sectional view of FIB milled air gap.

For the fabrication of a FIB milled device, the device to be milled is die bonded with silver filled epoxy on a thermally conductive aluminum nitride (AlN) mount, wire bonded, and then the mounted devices were placed in the ion miller and an air gap with a length of ~ 1.5 μm was created by FIB milling. Figure 2-8 and Figure 2-9 show the top and cross sectional view of one of the FIB milled devices. The gap was milled in the isolation area. From a top view, the ion milled air gaps seem to have vertical walls but the cross sectional view provides a different story.

Figure 2-9 shows that the walls of the ion milled air gap are angled. The angled wall may arise from misalignment of the [001] direction of the laser chip with the direction of the ion beam. The Ga^+ beam can be moved

horizontally in only one direction. When the milling is started, cutting the air gap from one side (the ion beam is narrower than the length of the air gap), there will be redeposition of etched materials on the opposite side. To remove these redeposited materials, it is necessary to rotate the sample stage by 180 degrees and repeat the milling procedure. This causes a 'V' shaped groove for an already existing misalignment between the sample stage and the incident Ga^+ beam. In addition, a non uniform aspect ratio of the gap and a Gaussian profile of the focused ion beam would also form angled side walls[54].

2.6. Determination of cavity lengths

Determination of the section lengths is an important issue for coupled cavity lasers with AMQW structures in terms of both mode selection and wavelength tuning mechanisms. The former depends on the section lengths and have been described previously[55]. The basic wavelength tuning mechanism of coupled cavity semiconductor lasers is based on changing the refractive index of either section by changing injection current. While fixing the lasing section (the output light is collected from the end facet of this section) current, the control section current is changed to provide wavelength variation of the output light. To have a broad tunable range with a fixed lasing section current, the maximum control section current, which is equal to the lasing threshold, should be large. This is required because commencement of lasing

action in a control section would cause a constant carrier density in that cavity causing no further changes in refractive index.

Threshold current is inversely proportional to the cavity length, which in turn, for AMQW lasers, is dependent on the transition cavity length (TCL)[56]. The TCL is a custom feature for AMQW lasers. It is defined as the length below which a laser operates on the short wavelength wells and above which the laser operates on long wavelength wells. At the TCL, the gain peak tends to be broad and flat and a maximum tuning range can be obtained. Keeping this in mind, the two section coupled cavity lasers used in this work are of long-short (long lasing-short control) form where the lasing section length is kept just above the TCL and that of the control section is kept well below the TCL. This makes sure that the longer section starts lasing at longer wavelengths and switches to shorter wavelengths with an increase of the injection current while the control section can only lase on short wavelength wells, which have a much higher value of threshold current than that of long wavelength wells.

The main idea of the TCL depends on the gain dependence of the AMQW lasers on carrier density. The quasi-Fermi level of the long wavelength (red) well is lower than that of the short wavelength (blue) well. As a result, red wells reach transparency at a lower carrier density compared to a blue well. With the increase of carrier density (by increasing the injection

current), blue wells reach transparency and contribute to the gain. At some particular carrier density, red and blue wells have approximately equal peak gain and the total gain curve is broad and spectrally flat. At higher carrier densities, the gain from the blue wells dominates.

For this structure, I found the TCL to be around 850 μm. Lasing and control section lengths were taken to be around 960 ± 5 μm and 380 ± 5 μm respectively. Ridge widths of 2.5 μm – 3 μm were chosen for they do not produce multiple spatial modes. As mentioned earlier, after cleaving, these devices were fabricated by bending the two sections, which produces a 'V' shaped gap.

2.7. Summary

Procedures involving the fabrication of two-sectioned coupled cavity diode lasers have been presented in this chapter. Both etching and cleaving techniques were explored for the creation of gap between the cavities. Both FIB milled and C^3 device produce non vertical side walls of the air gap. How this non vertical nature of the air gap side walls affects the operation of coupled cavity devices is explored in the next chapter.

3. Below threshold transfer matrix model for AMQW coupled cavity semiconductor lasers.

3.1. Introduction

I have observed, in agreement with Ref.39, that the walls of the air gap of cleaved coupled cavity lasers are not necessarily vertical. To verify how the non-vertical nature of the walls affects the operation of a coupled cavity device, a below threshold model for a two section coupled cavity diode laser that takes into account tilted walls (facets) for the air gap was created and simulated. A below threshold model is of importance because from fits of the model to measured below threshold spectra one obtains necessary information like the wavelengths and spacing of the longitudinal modes, the index of refraction, the modal gain, and accurate estimates of the lengths of the sections, of the gap, and of the coupling between the sections. These parameters can be used in an above threshold laser model to understand the operation and to optimize the design of coupled cavity devices. In this chapter, details of this simulation along with results verified by the experimentally measured data are discussed.

3.2. Approach towards below threshold model

Previous transfer matrix below threshold models[57, 58] have assumed vertical walls for the air gap located between the two sections. Fits to below threshold spectral measurements of my fabricated devices showed that air gap wall angles affect the coupling between the sections significantly and hence affect the operating characteristics of the devices.

A transfer matrix approach was used to represent a coupled cavity device. The coupling efficiency between the two sections as a function of the angles of the walls of the air gap was calculated by assuming that the spatial mode in each section is a Gaussian beam and by calculating the overlap between the angled and offset sections. The spatial modes in each section are assumed to be the same since they originate from the same laser. Scattering matrix parameters for the air gap were obtained using this coupling efficiency. By using non linear fitting on the experimentally measured below threshold spectra of coupled cavity devices with various wall tilts, I demonstrate that for large wall angles (≥7 degrees), coupled cavity devices work similar to an injection locked laser[59] while for small wall angles (≤ 4 degrees), coupled cavity devices work as a true coupled system.

3.3. Analysis of below threshold model

An analysis of a two section coupled cavity device with different wall angles is presented in this section. Figure 3-1 shows a schematic representation of a two section coupled cavity laser with the field amplitude components. The

incoming/outgoing waves toward/from the end facet of the left cavity are given by $\vec{E}_{01}^{+}$ and $\vec{E}_{01}^{-}$ respectively and those from the right end facet are $\vec{E}_{43}^{-}$ and $\vec{E}_{43}^{+}$. The superscript "+" or "−" signifies the direction of propagation (to the right or to the left) of the electric field. The subscripts "0", "1", "2", "3" and "4" represent different cavities and interfaces. Incoming waves toward the air gap from the left/right sidewalls are given by $\vec{E}_{12}^{+}$ and $\vec{E}_{32}^{-}$ respectively and those outgoing from the air gap are $\vec{E}_{12}^{-}$ and $\vec{E}_{32}^{+}$. The goal of this analysis is to find the below threshold spectrum and to account for the coupling between the two cavities. With the help of a wave scattering analysis[60], the air gap between the two cavities can be represented by a scattering matrix $[S_{ij}]$ where S_{11} and S_{22} are the reflection coefficients and S_{12} and S_{21} are the transmission coefficients.

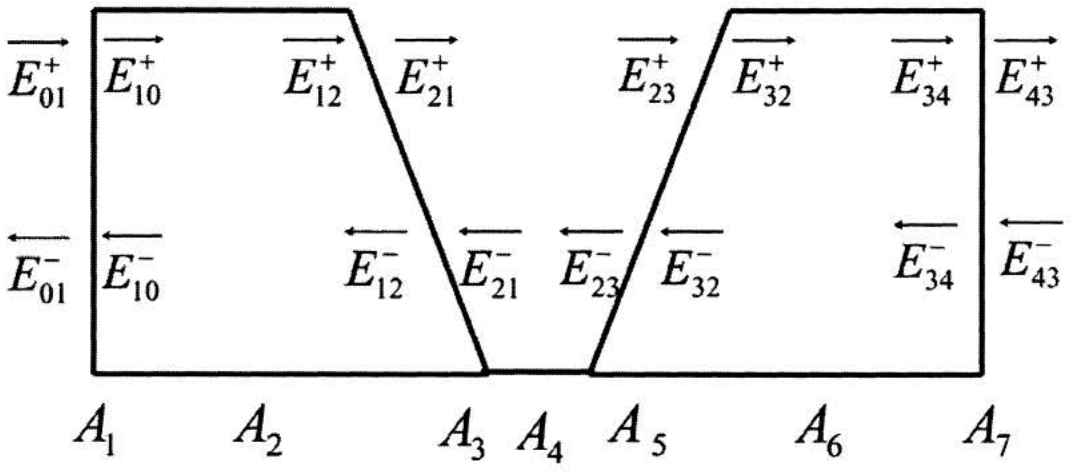

Figure 3-1 One dimensional schematic representation of E-field inside a two section coupled cavity laser.

A_1, A_2, A_3, A_4, A_5, A_6, and A_7 represent the transfer matrices[60] for interfaces and cavities starting from the facet at the left of Figure 3-1. The transfer matrix for the whole system is simply the multiplication of the individual matrices in the correct order and is given by the following equation:

$$A_{final} = A_1 \times A_2 \times A_3 \times A_4 \times A_5 \times A_6 \times A_7 . \quad (3.1)$$

Transfer matrices A_i are represented by 3×3 matrices. The third dimension is used to accommodate spontaneous emission in the cavity transfer matrices (A_2 and A_6). A 2×2 matrix cannot be used because it cannot include the spontaneous emission, which is necessary to predict the below threshold spectral output. Morrison[61] has demonstrated a quantum mechanically correct approach to include the spontaneous emission in a transfer matrix approach. This model treats the emission of a quantum of radiation quantum mechanically and takes into account the probability of each path taken by the emitted quanta and the cross correlation between them. Owing to long section lengths as compared to a wavelength of the light in the cavity, the cross correlation is negligible and hence I adopted this simpler model. The matrices are as follows (see Appendix C for the angled facet transfer matrix parameters):

$$A_1 = \begin{bmatrix} 1/t_{01} & r_{01}/t_{01} & 0 \\ r_{01}/t_{01} & 1/t_{01} & 0 \\ 0 & 0 & 1 \end{bmatrix} \tag{3.2}$$

$$A_2 = \begin{bmatrix} e^{(jK_1L_1)} & 0 & -\delta_{1,m} \\ 0 & e^{(-jK_1L_1)} & \delta_{1,m} \\ 0 & 0 & 1 \end{bmatrix} \tag{3.3}$$

$$A_3 = \begin{bmatrix} A_{11}^3 & A_{12}^3 & 0 \\ A_{21}^3 & A_{22}^3 & 0 \\ 0 & 0 & 1 \end{bmatrix} \tag{3.4}$$

$$A_4 = \begin{bmatrix} e^{(jK_0d)} & 0 & 0 \\ 0 & e^{(-jK_0d)} & 0 \\ 0 & 0 & 1 \end{bmatrix} \tag{3.5}$$

$$A_5 = \begin{bmatrix} A_{11}^5 & A_{12}^5 & 0 \\ A_{21}^5 & A_{22}^5 & 0 \\ 0 & 0 & 1 \end{bmatrix} \tag{3.6}$$

$$A_6 = \begin{bmatrix} e^{(jK_2L_2)} & 0 & -\delta_{2,m} \\ 0 & e^{(-jK_2L_2)} & \delta_{2,m} \\ 0 & 0 & 1 \end{bmatrix} \tag{3.7}$$

$$A_7 = \begin{bmatrix} 1/t_{34} & r_{34}/t_{34} & 0 \\ r_{34}/t_{34} & 1/t_{34} & 0 \\ 0 & 0 & 1 \end{bmatrix} \tag{3.8}$$

where L_i is the length of the i^{th} cavity; r_{ij} is the amplitude reflection coefficient at the ij interface; t_{ij} is the amplitude transmission coefficient at the ij interface; $K_{1,2}=2\pi n_{eff}/\lambda$, with n_{eff} the effective refractive index of the waveguide; $K_0=2\pi/\lambda$;

$\delta_{i,m}$ is the electric field of the total amount of spontaneous emission for the i^{th} cavity that is produced and coupled into the m^{th} longitudinal mode; A_{ij}^{n} is the ij^{th} element of the n^{th} matrix; and, d is the length of the air gap between the two cavities.

A_4 represents the gap transfer matrix. In the gap, free space beam propagation is used assuming Gaussian beam propagation. The beam waist of the Gaussian beam was experimentally determined from near field measurements. The beam shape is elliptical because of differences in mode confinement in the lateral and transverse directions. The initial spot size in the lateral direction is considered the same as the ridge width and that in the transverse direction is given by the thickness of the waveguide from the p-SCH layers to the n-SCH. The waist size after traversing a gap width[62] of d is given by:

$$\omega_{x,y} = \omega_{ox,oy}\left[1 + (2d / k\omega_{ox,oy}^{2})^{2}\right]^{1/2} \qquad (3.9)$$

where (ω_{ox}= 0.55μm, ω_{oy} = 2.8μm) and (ω_x, ω_y) are the initial and final waist sizes after traversing the gap in the lateral and transverse directions respectively. A_3 and A_5 represent the transfer matrices for the angled walls of the air gap. The components of each matrix are determined by finding the coupling coefficients between incident, reflected, and transmitted beams at each interface and are given in Appendix C. The coupling coefficients are

calculated from overlap integrals of the interacting beams. The reflectivity at the air gap interface is calculated using Fresnel's equations.

The analysis is three dimensional with operation on the fundamental spatial mode assumed and $\delta_{i,m}$ is given by[63]:

$$\left\langle \left|\delta_{i,m}\right|^2 \right\rangle = \beta \frac{B_{i,m}}{g_{i,m}} (G_{i,m} - 1) \tag{3.10}$$

where $G_{i,m}$ is the single pass gain for the m^{th} mode in the i^{th} section, $g_{i,m}$ is the modal gain for the m^{th} mode in the i^{th} section, and $B_{i,m}$ is the amount of spontaneous emission produced per unit length in a spectral interval corresponding to the m^{th} mode in the i^{th} cavity. The spontaneous emission factor β provides the fraction of spontaneous emission that couples into the fundamental mode.

Now I am set to calculate the below threshold intensity output from each output facet. The final transfer matrix of the system given is of the form

$$A_{final} = \begin{bmatrix} a_{11} & a_{12} & a_{13} \\ a_{21} & a_{22} & a_{23} \\ 0 & 0 & 1 \end{bmatrix} \tag{3.11}$$

The incoming and outgoing fields at the output facet of the left cavity can be represented by 3×3 matrices as:

$$\begin{bmatrix} E_{01}^{+} \\ E_{01}^{-} \\ 1 \end{bmatrix} = \begin{bmatrix} 1/r_{01} & r_{01}/t_{01} & 0 \\ r_{01}/t_{01} & 1/t_{01} & 0 \\ 0 & 0 & 1 \end{bmatrix} \begin{bmatrix} E_{10}^{+} \\ E_{10}^{-} \\ 1 \end{bmatrix} \tag{3.12}$$

Using Eqs. 3.1, 3.11and 3.12, the field amplitudes at the output facets can be related as follows:

$$\begin{bmatrix} E_{01}^{+} \\ E_{01}^{-} \\ 1 \end{bmatrix} = \begin{bmatrix} a_{11} & a_{12} & a_{13} \\ a_{21} & a_{22} & a_{23} \\ 0 & 0 & 1 \end{bmatrix} \begin{bmatrix} E_{43}^{+} \\ E_{43}^{-} \\ 1 \end{bmatrix} \tag{3.13}$$

As there is no external injection of light into the cavities from the end facets, $\vec{E}_{01}^{+} = \vec{E}_{43}^{-} = 0$.

After simplification of Eq. 3.13 I obtain the field amplitudes from the right and the left side of the system as follows:

$\vec{E}_{43}^{+} = -a_{13}/a_{11}$ and $\vec{E}_{01}^{-} = -a_{21}\vec{E}_{43}^{+} + a_{23}$.

To understand the coupling between two cavities with angled walls, first assume that the walls of the gap are vertical. There will not be complete coupling because of free space propagation. As the laser beam propagates through the air gap, its size and phase front changes. When the beam reaches the other cavity, the overlap integral between the mode in the other cavity and the beam that propagated across the gap is diminished. As both the sections are from the same laser, the beam parameters are taken to be

the same in each section. The coupling efficiency τ along one dimension is the absolute square of the overlap integral of the interacting fields. The coupling efficiency[62] for this aligned case is given by:

$$\tau_i = \frac{2}{\left[(\omega_{oi}/\omega_i + \omega_i/\omega_{oi})^2 + (\lambda/\pi\omega_i\omega_{oi})^2 s^2\right]^{1/2}}, i = x, y; \tag{3.14}$$

where τ_x and τ_y are the coupling efficiencies along the transverse and lateral directions. ω_{ox}, ω_{oy}, ω_x, ω_y are the initial and final spot sizes, s is distance between the initial beam waist of the interacting beams.

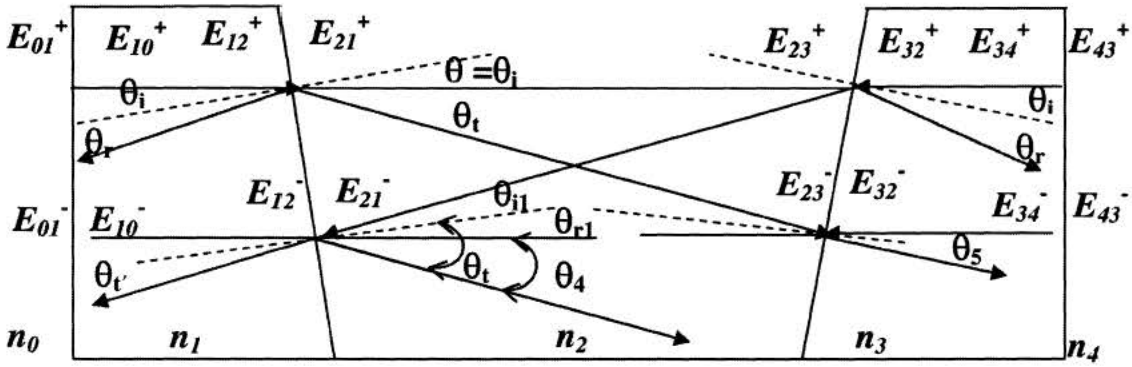

Figure 3-2 Effect of tilted side walls: Beams at air gap/cavity interface will leave an angular offset while overlapping each other.

If the walls are tilted as shown in Figure 3-2, the coupling efficiency will change because of further change in the overlap between the beams. The beams that propagate across the gap will be offset and refracted with an increased waist size. This will reduce the coupling. In addition, the reflected beams at the facets of the gaps will have an angular misalignment with the incident beam, which will reduce the reflectivity of the gap facet. The total

coupling efficiency T, assuming the spatial mode of the laser can be approximated as a Gaussian beam, is given by[62]

$$T = \tau_x \tau_y \exp[-(\theta_x / \theta_{e,x})^2 (\theta_y / \theta_{e,y})^2] \quad (3.15)$$

Here, θ_x and θ_y are the tilt and offset angles; and $\theta_{e,x}$, $\theta_{e,y}$ are the angular tolerances.

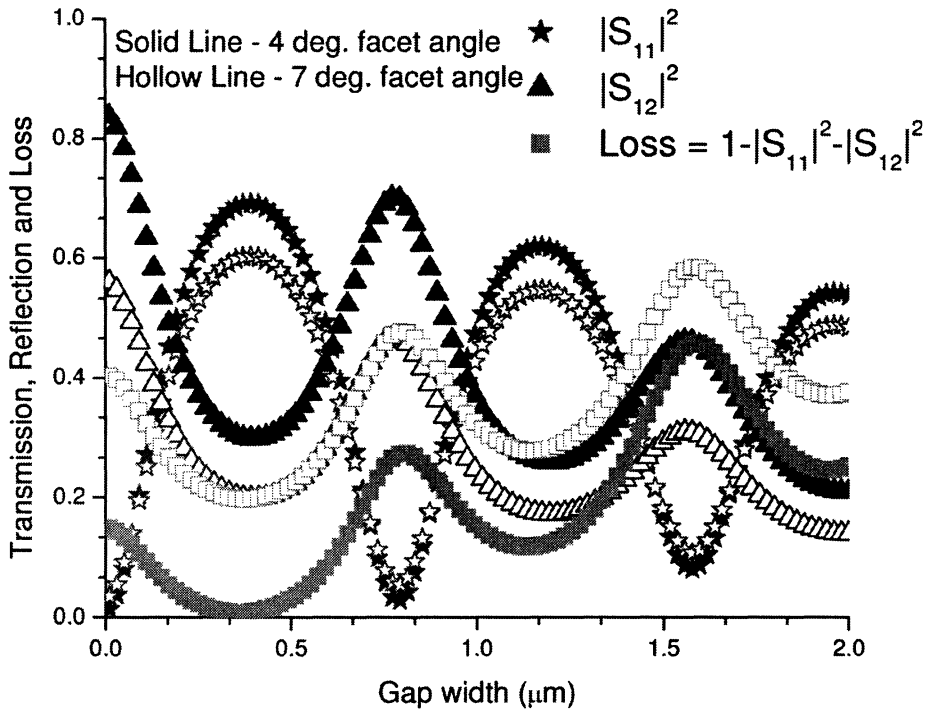

Figure 3-3 Predicted transmission, reflection and loss coefficients as a function of the length of an air gap and facet angle 4° and 7°.

To show how coupling between the two sections changes with facet angles, scattering matrix parameters of the gap were calculated. $A_3 \times A_4 \times A_5$ provides the transfer matrix of the air gap. Figure 3-3 shows the reflection

coefficient $|S_{11}|^2 = |a_{11}|^2$, the transmission coefficient $|S_{12}|^2 = |a_{12}|^2$, and the loss $(1 - |S_{11}|^2 - |S_{12}|^2)$ for various gap widths for air gap wall angles of four and seven degrees. It can be readily seen that the loss increases with the angle of the facet, which means less coupling between the sections.

3.4. Wavelength tuning capability of coupled cavity laser

Before I start analyzing the results from the transfer matrix below threshold model of a coupled cavity diode laser, a description of the wavelength tuning capability and mechanism is required.

The basic principle for wavelength tuning by a coupled cavity laser has been explained previously by several authors[38-39]. Figure 3-4 shows a schematic of the wavelength tuning mechanism in a two section coupled cavity diode laser. Section I and II have lengths L_1 and L_2 respectively with $L_1 > L_2$. The longitudinal modes that can fit in each section depend on the effective refractive index n_{eff} and the length of the section. Initial longitudinal modes in section I and II are shown with solid lines and mode separations for either section are denoted as $\Delta\lambda_1$ and $\Delta\lambda_2$. The modes of a coupled cavity are the ones that are common to both the sections. Stable longitudinal mode operation is obtained as the combined effect of coupled-cavity mode selection and active medium gain roll-off. If the injection current is changed in either of

the sections, n_{eff} will change because it is a function of the carrier density. A change in n_{eff} will change the mode spacing and hence shift the mode wavelengths. When the shift is enough so that the mode coincides with the next available longitudinal mode of the other cavity, the lasing wavelength will change to this new common mode. As shown in Figure 3-4, the initial lasing mode (solid line) is selected by the fact that it is one of the modes of the coupled cavity and is exposed to the highest value of gain. With change in the injection current of section II, the mode spacing $\Delta\lambda_2$ is changed to $\Delta\lambda'_2$ causing a new set of coupled cavity modes. The new lasing mode (dotted line) now has the highest gain value.

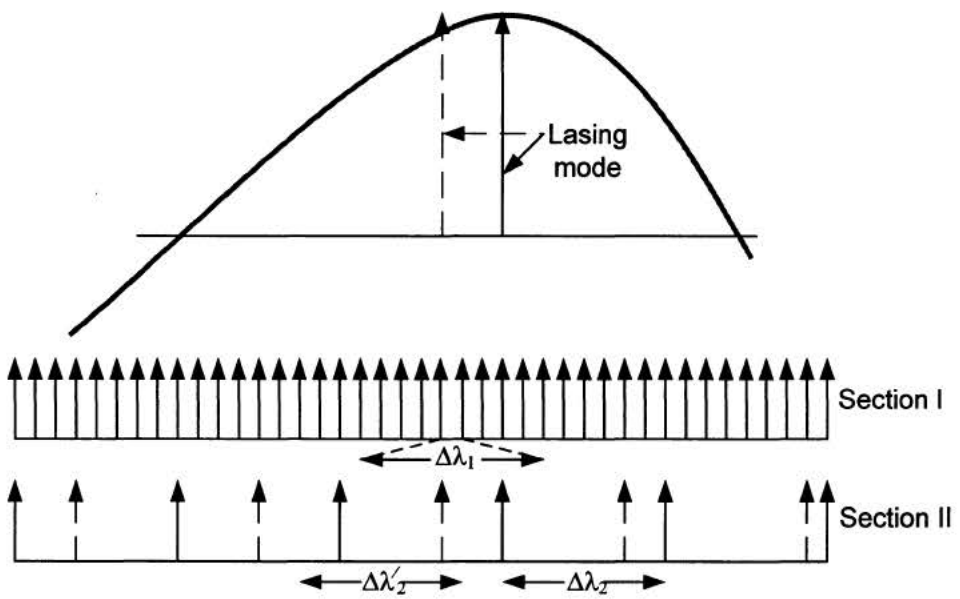

Figure 3-4 Schematic wavelength tuning mechanism in a two-section coupled cavity laser.

Let us consider the injection current in the long (L_1) and short (L_2) section and denote these currents as I_1 and I_2. By fixing I_1 at various values and then changing I_2 for each value of I_1, we can tune over a wide range of wavelengths. Figure 3-5 shows the total spectrum of a FIB milled coupled cavity device obtained by varying I_1 and I_2. The two section lengths were L_1 = 1040 ±10μm and L_2 = 260 ±10μm with a gap of ~1.5 μm. At first, a two sectioned laser was diced from the wafer. The cleaving process was done manually with the aid of a microscope and there could be an uncertainty of ± 10 μm on the lengths of the cleaved sections. The uncertainty of the gap length depends on the resolution of the FIB system. At the normal working distance of 12 mm with Ga ion acceleration energies between 5-30 keV, a resolution of 5 nm can be achieved[64]. Figure 3-6 shows the spectral output for a C^3 device. Note that colors are reused here to accommodate all the wavelengths. The FIB milled device has a tuning range of about 60 nm while that of the C^3 device is about 100 nm. The major difference between the results is the gaps in the spectra. While the C^3 device shows a nearly continuous tuning range, the FIB milled device shows large mode hops.

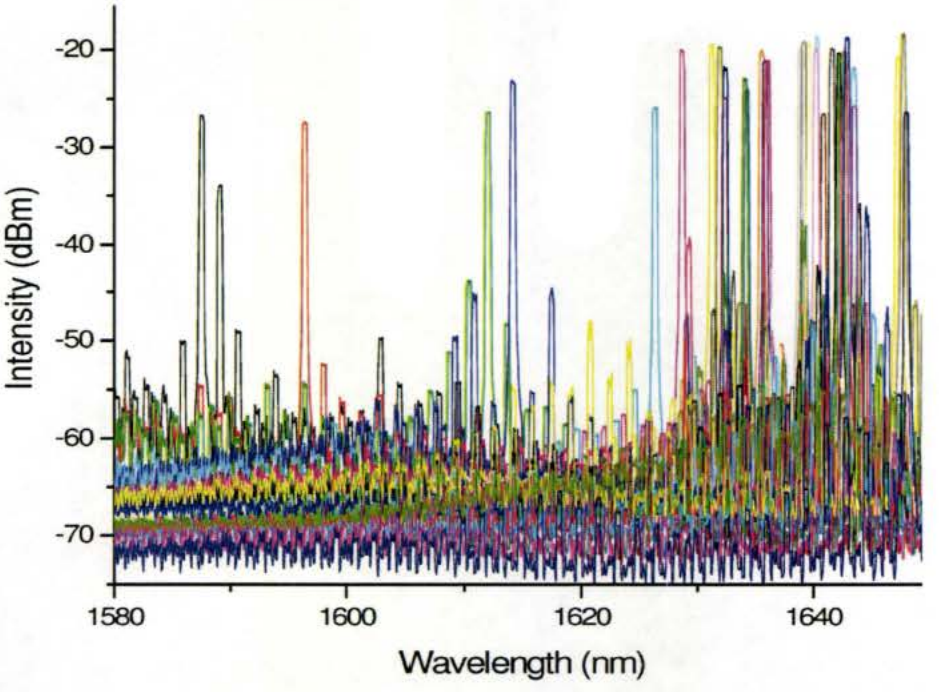

Figure 3-5 Total single mode spectrum for a FIB milled device with various I_1/I_2 ratio.

Figure 3-7 shows the L-I curve of a typical two-section C^3 device for a fixed lasing section and various control section currents while Figure 3-8 shows a single mode spectra. The two section lengths for this device were L_1 = 1000 ± 10μm, L_2 = 350 ± 10μm and gap length ~ 1.5 ± 0.1μm. Precision of gap length in this case mainly depends on the control in applying a bending moment (see Fabrication techniques for two section AMQW coupled cavity lasers). The uncertainty of the air gap length for this particular device was found by fits of the below threshold model to the measured below threshold spectral data. The maximum total power was ~10 mW with a ~30 dB SMSR. A wide area InGaAs photodiode was placed very near to the end facet of the

lasing section (end facet from where the output light is collected) to collect as much emission as possible.

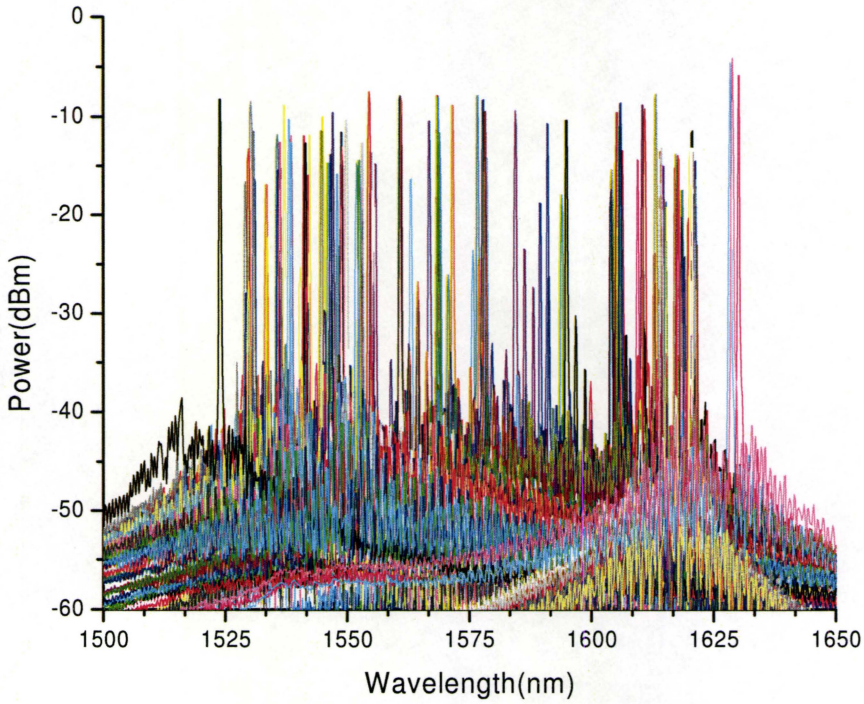

Figure 3-6 Total single mode spectrum for a C^3 device with various I_1/I_2 ratio.

A standard diode laser measurement setup was used for experimental spectral measurements. Two separate p-contacts were used for injecting current into the two sections and a common n-contact was used. A single mode tapered fiber was used for the collection of light from the longer section of the laser. The tapered fiber was connected to an Anritsu MS9710C optical spectrum analyzer (OSA).

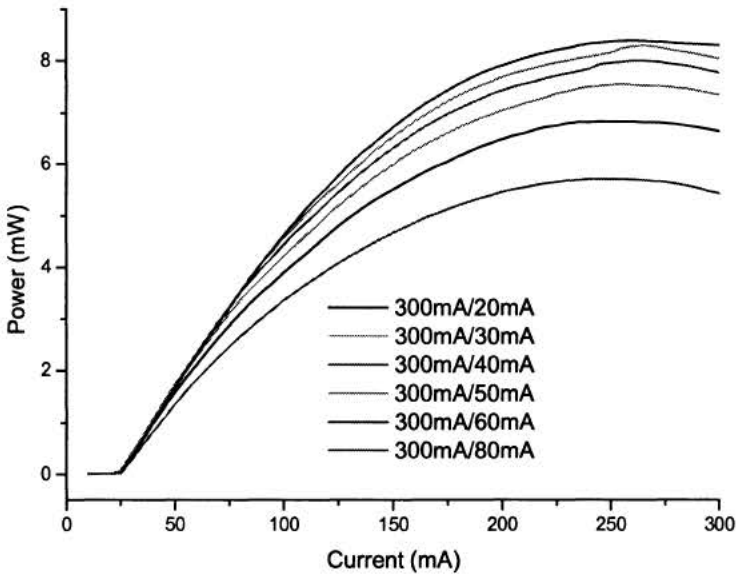

Figure 3-7 L-I measurement for a C^3 device with various I_1/I_2 ratio.

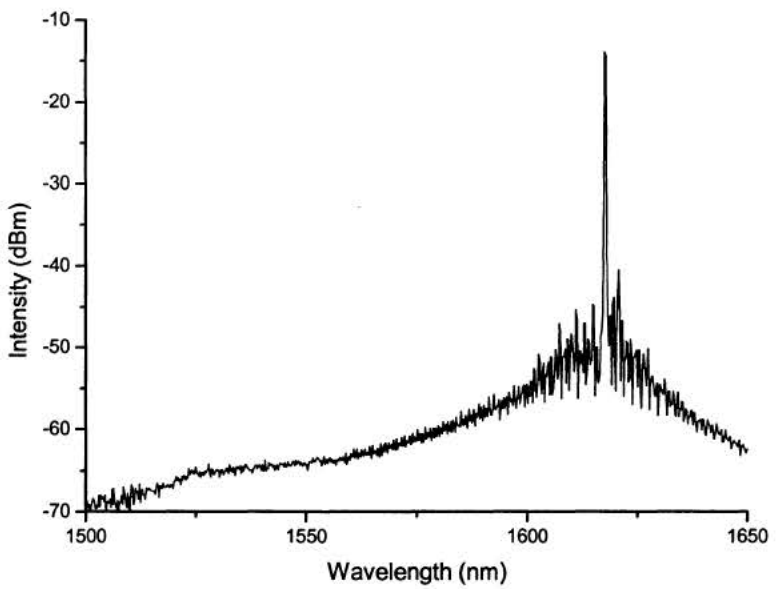

Figure 3-8 Single mode spectra of a C^3 device with ~ 30dB SMSR.

3.5. Non linear fitting of below threshold spectrum

A non linear fitting algorithm was integrated into the below threshold model described in the previous section to find best estimates of device parameters. The Marquardt method[65] was chosen for the fitting algorithm because it has a significant advantage over other non linear fitting methods like grid search method, gradient search method, and parabolic expansion methods. In the grid search method, chi squared is minimized by varying each parameter separately. It requires many successive iterations to locate the minima and hence converges slowly. The gradient search method varies all the parameters simultaneously so that the direction of propagation in the parameter space is along the direction of the steepest descent of chi squared. The main disadvantage of this method is its inability to approach the minima of chi squared asymptotically because of the zero gradient at the minima. In addition, gradient recompilation for each small step size results in slow and hence inefficient searches. In the parabolic expansion method, instead of searching for the chi squared minima with variation of parameters, approximate analytical functions describing the chi squared hyper surface are developed. The approximations will introduce errors into the calculated values of the parameters, but successive iterations of the analytical method will approach the chi squared minima. This method converges much faster than the grid or gradient search method as the required number of computations is

smaller than the previous two. The main disadvantage of this method is its inability to converge from a point outside a nearby region of the minima where the chi square hyper surface is approximately parabolic[65]. The Marquardt algorithm is a combination of the gradient search and expansion methods. During the initial search, it behaves more like a gradient search algorithm, which is best for approaching the minima from a far away point, and in the final stage, when a chi squared minimum is nearby, behaves more like the expansion method. However, poorly selected starting values in the Marquardt method may cause the search to terminate in a local minimum (higher chi square value than the absolute minima) of the chi square hyper surface providing non optimized values of the parameters. I used different sets of starting parameters selected from experience and controlled the termination of the program by a preselected difference of chi squared from one iteration to the next. The lowest chi square obtained from this combination is assumed to be the absolute minimum. The effective index of refraction, lengths of control and lasing sections, air gap facet angles, and air gap length were the main fitting parameters considered in this algorithm. Some typical starting values for these parameters can be obtained from the example code provided in Appendix D.

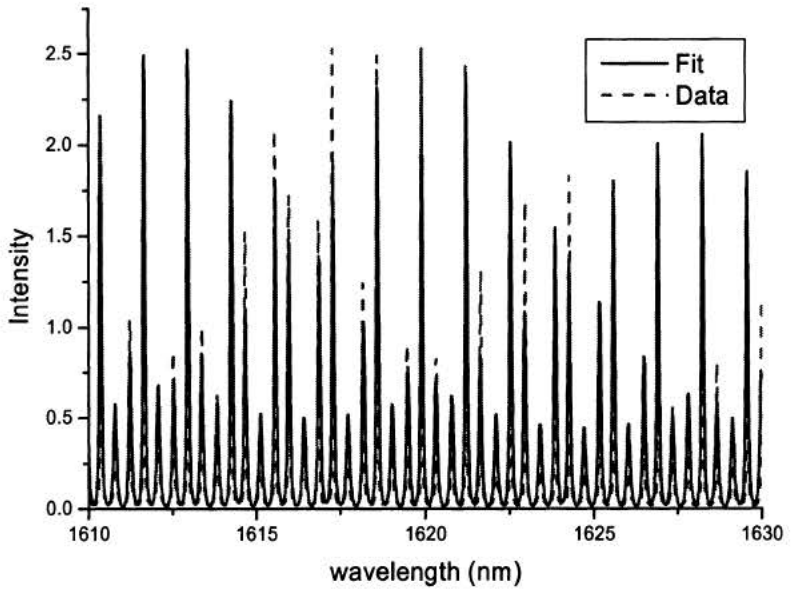

Figure 3-9 Below threshold spectral fit for a FIB milled device (20nm).

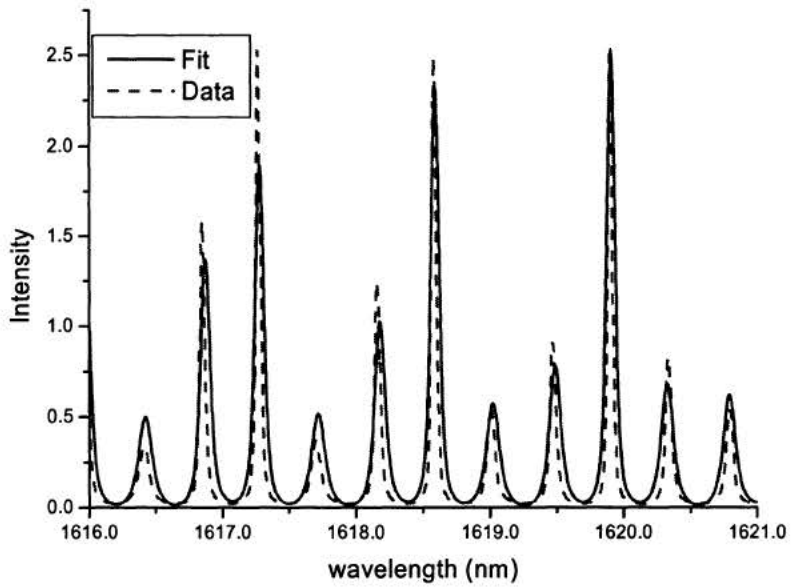

Figure 3-10 Below threshold spectral fit for a FIB milled device (5nm).

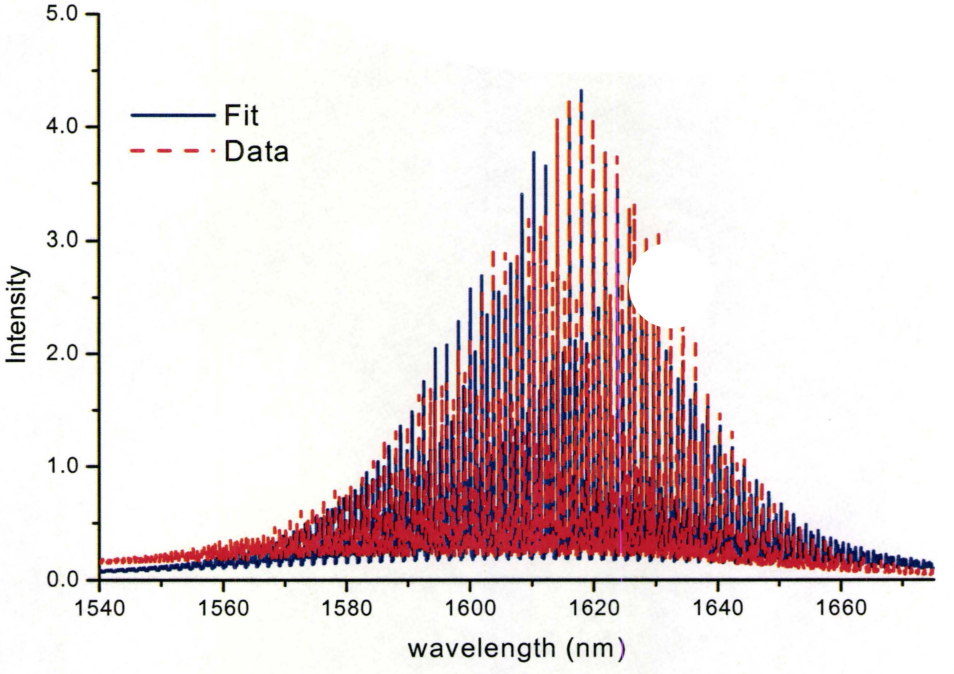

Figure 3-11 Below threshold spectral fit for a C^3 device (100nm).

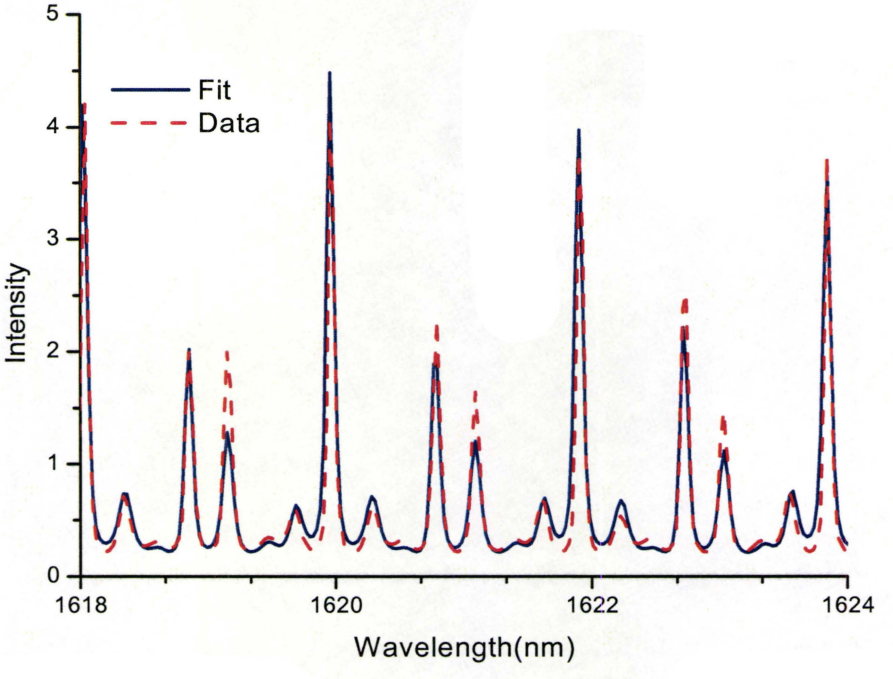

Figure 3-12 Below threshold spectral fit for a C^3 device (6nm).

Figure 3-9 shows the below threshold measurement of a FIB milled coupled cavity device. It also shows the least squares fit of the model to the data for 20 nm with cavity and gap lengths of L_1 = 996.04 ± 0.024 μm, L_2 = 278.96 ± 0.006 μm, and L_g = 1.520 ± 0.002 μm. Figure 3-10 shows a magnified view of Figure 3-9 for a 5 nm window. A good fit for the mode spacing could be achieved. However, the fit for the intensities of the modes is not as pleasing, which could owe to non uniformity of the facet smoothness caused by FIB milling. This fit converges for a side wall tilt θ_x = 7.0 ± 0.1 deg. Figure 3-11 shows the below threshold fit of a C^3 device for a 100 nm spectral window while Figure 3-12 shows a magnified view of Figure 3-11 with a 6 nm span. Lengths and side wall tilt obtained from the fit to the below threshold spectra for this device are L_1 = 967.12 ± 0.034 μm, L_2 = 390.25 ± 0.013 μm, L_g = 1.56 ± 0.08 μm, and 4 ± 0.15 deg. It should be mentioned here that offset angle θ_y, was assumed to be zero in the simulation. The uncertainty calculated for the parameters is obtained by multiplying the mean squared error with the square root of the diagonal elements of the error matrix[65]. This provides an estimate of the precision with a confidence level of 68%. A sample MatLab code for the below threshold transfer matrix model including the non linear fitting method is given in Appendix D.

For a Fabry-Perot laser, the mode spacing is given as $\Delta\lambda = \lambda_o^2/(2N_gL)$ where λ_0 is the center wavelength, N_g is the group effective refractive index, and L is the length of the cavity. From the fit results, it is observed that for FIB milled devices, the mode spacing depends on L_1 only. Changing L_2 does not change the mode spacing while it changes accordingly with a change of L_1. This suggests that the two sections are operating as two separate lasers. This indicates that for a ~7 deg wall tilt, coupling between the two sections is weak (coupling between the two sections, which is the ratio of transmission to reflection coefficient, is calculated to be 69 % for 7 deg of facet angle at λ=1.58 μm and an air gap of 1.55 μm) and the device is working similar to an injection locked laser[66] whereas for the C^3 devices, where the side wall tilt is <~4 deg, the mode spacing is given by:

$$\Delta\lambda = \frac{\lambda_o^2}{2(N_{g1}L_1 + N_{g2}L_2 + L_g)} \tag{3.16}$$

In this case, the mode spacing depends on the combined cavity length. This is understandable as the C^3 device with a smaller wall tilt allows a better coupling of light between the two sections (the coupling between the sections is calculated to be 94% for 4 deg of facet tilt and an air gap of 1.55 μm at λ = 1.58 μm). This causes the sections of the C^3 devices not to act as separate lasers but rather as a true coupled cavity device.

The injection locked behavior of coupled cavity devices has been demonstrated before[38] where two separate diode lasers of nearly equal length lasing at similar wavelengths were coupled together. The output wavelength could be locked and unlocked by direct modulation of the injection current in one diode. A true coupled system is one where the two sections together with the air gap act as a single section laser. In this true coupled device the longitudinal mode spacing is defined by the combined section lengths. Coldren *et al.*[38] *and* Choi *et al.*[55] demonstrated coupled cavity devices with shallow grooves, where the grooves did not penetrate the active region. As expected, the shallow groove devices showed higher couplings between the sections and the mode spacings were determined by the total cavity length.

To show how side wall tilt affects the mode spacing of the device, a below threshold simulation was compared for a C^3 device with 7 and 4 deg side wall tilts. The lengths of the two sections used in this case were L_1 = 967.12μm, L_2 = 390.25 μm, and L_g = 1.55 μm. For a side wall tilt of 7 deg., as shown in Figure 3-13, the mode spacing was found to be 0.38 nm which corresponds to a cavity length of 967 μm (L_1) at a center wavelength λ = 1.6 μm and a refractive index of 3.5. Similarly for a side wall tilt of 4 deg., the mode spacing was 0.27 nm, which corresponds to a cavity length of 1357.3 μm = (L_1 + L_2 + L_g) for the same center wavelength and refractive index.

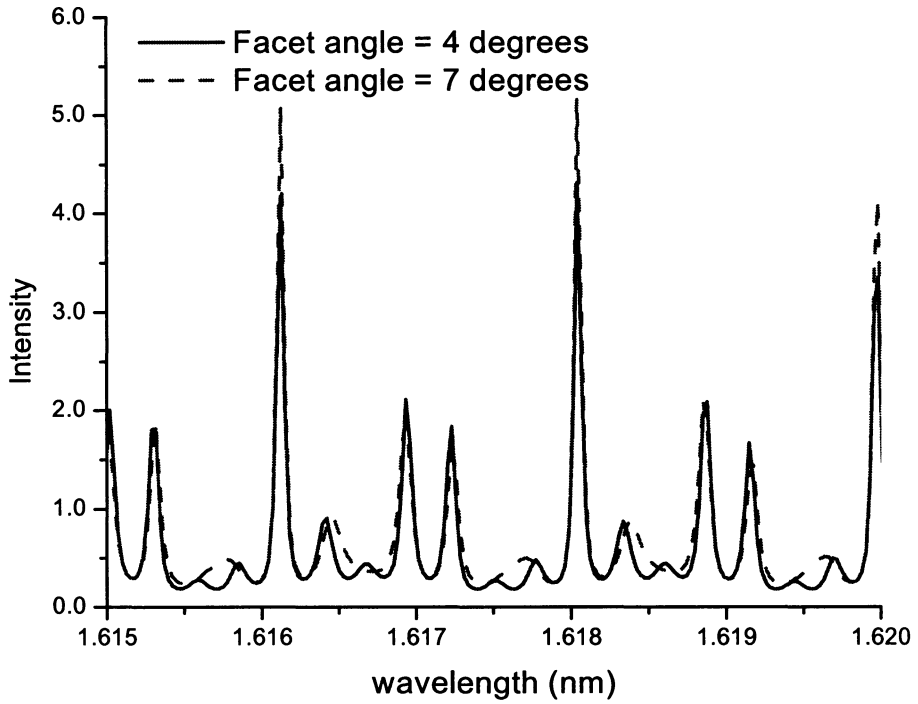

Figure 3-13 Effect of facet angles on below threshold spectrum.

Better tuning capability as shown in Figure 3-6 can also be explained in terms of the enhanced coupling in C^3 devices. For both FIB milled and C^3 devices, the lasing modes depend on the position of the gain peak, gain roll-off, the wavelength dependant reflectivity, and coincidences of modes from both sections. Increasing I_2 will decrease N_{eff} in the second section due to an increase in the carrier density. For injection locked lasers, the below threshold output spectrum will not undergo any change in mode spacing for changes in the current in the second section I_2 as the sections are operating as two separate lasers and the output light is collected from the first section. But for a C^3 device, as the two sections are working as a combined cavity, any increase of carrier density in the first or second section results in a change of refractive

index for the whole cavity and hence a change in mode spacing is observed. Increasing the carrier density will cause a blue shift of the gain peak owing to band filling and additional heating of the device causing a red shift of modes. As the heating effect is more prominent at low frequencies an overall red shift of modes is observed. The combined effect of the band filling and thermal changes causes the lasing mode to switch. Unlike FIB milled devices where each wavelength switch requires a new set of modes to coincide, modes in a C^3 device shift together. Hence big mode hops are not observed for devices with small tilts of the walls of the gap.

3.6. Summary

I have presented the analysis of two section coupled cavity lasers having a gap with walls (facets) that are tilted. A transfer matrix formulation was used to represent the system. Each facet and section was represented by a transfer matrix. Using the transfer matrices of the angled facets and air gap, the scattering matrix parameters for "V" shaped grooves were calculated. The coupling efficiency at each tilted facet was found by calculating the overlap integral of the two beams incident on the tilted facet. A below threshold model for the coupled cavity two section laser was formed which predicts the modes of the system and non linear fits were performed on the experimental data to extract parameters necessary for device optimization. It was observed that tilted walls of the gap have a huge impact on the coupling

of light between the two sections of coupled cavity devices. For walls with tilt angles ~ 7 deg., devices appear to work as injection locked lasers while for walls with tilt angles ~4 deg., the sections are coupled. Previous analyses of coupled cavity diode lasers neglected the effect of tilted side walls and did not develop a fully coupled model with possible mode spacings corresponding to the length of the entire laser structure. I have demonstrated that if the side wall tilt can be kept ≤ 4 deg., a much better tuning capability is obtained. I also have demonstrated a broad, single mode tunable range (~100 nm). This is due to the combined effect of a coupled cavity scheme and the broad gain profile of AMQW lasers. The electronic tunability of coupled cavity devices allows a much faster tuning speed than the tuning speed obtained by mechanical or electro-mechanical schemes. High speed modulation on each section of the device would provide rapid wavelength switching for this broad range. This could be a very attractive source for optical communication especially for WDM. A broad tuning range together with fast wavelength tuning capability can also be a very promising source for real time applications. Some probable applications of this fast, tunable diode laser are explored in Chapter 5. Chapter 4 presents an above threshold model for coupled cavity lasers.

4. Above threshold model for AMQW coupled cavity semiconductor lasers

4.1. Introduction

In this chapter, I present above threshold simulations of a two-section coupled cavity diode laser. Device parameters obtained from comparison of experimental data with below threshold simulations described in the previous chapter were used in this above threshold simulation of the two section coupled cavity semiconductor laser. The model verifies the tuning mechanism employed by a two section C^3 laser and indicates the limits on the performance that can be expected from them.

4.2. Approach towards above threshold model

There are two commonly used approaches for modeling the steady state light versus pumping characteristic for lasers: (1) a rate equation approach; or, (2) a travelling wave or Fabry-Perot (FP) approach. Relationships between the pump rate and the spectral output of a laser are often described by the rate equations. These equations are of differential form and can be used to understand and predict changing experimental conditions. The existing above threshold models[38,55] for coupled cavity lasers used a rate equation approach. The coupled rate equations describe the photon and inversion densities of the active region of a laser and can be solved in steady state condition to provide

analytic solutions. However, simulation of diode lasers with a rate equation approach does not include the effect of the laser cavity properly. The laser cavity in a rate equation approach is described by an equivalent loss ignoring the fact that the laser mode intensities vary along the optic axis of the laser because of the cavity gain. By doing this, the rate equations also ignore the amplification of the spontaneously emitted light traversing inside the laser cavity. In addition, a steady state rate equation approach does not include asymmetric resonators, compound cavities, or feedback[16]. For the travelling wave method, a set of non-linear coupled differential equations describing the amplification of the modes propagating through the amplifying medium are used to simulate the output of an injection laser[16]. Spectral output power in terms of pumping rate, spontaneous, and saturation profile for each mode were obtained using this model. The travelling wave approach predicts the active region gain of the laser, which is exponential in nature, and can easily include asymmetric resonators, compound cavities, laser amplifiers, and the effects of feedback on output spectra. Cassidy compared the rate equation and travelling wave approaches[67] and concluded that both the methods predict identical results in steady state if the rate equation result is scaled to include explicitly the effects of the laser cavity but cautioned that this action lessens the correspondence between theoretical and independently measured parameters.

4.3. Travelling wave model

In the travelling wave model, a single section diode laser is seen as a FP resonator formed by two plane-parallel mirrors containing an amplifying medium. For the case of multi section diode lasers, each section is treated as a single section laser. Coupling between the adjacent sections is considered by taking into account the coupling efficiencies obtained from the below threshold model described in the last chapter. For each section, coupled rate equations describing the interaction of population inversion and photon density are used to describe an infinitesimal section of the amplifying medium. Integration of this infinitesimal gain element over the region bounded by the end reflectors provides the output of a particular section. Unlike in the rate equation model, the cavity is explicitly defined by boundary conditions used at the position of the end reflectors.

The goals of these simulations were to demonstrate the mode selection mechanism in a coupled cavity laser, to determine the optimum parameters, and to understand the limits to the performance of the devices. The role of spontaneous emission is very significant in a FP model in determining the laser field. It was assumed that the rate of spontaneous emission was uniformly distributed throughout the laser volume and that the laser output is the coherent amplification of the spontaneous light.

The following equations were used to describe the amplifications of the modes and the population inversion $n(x)$ in an infinitesimal of gain material in the cavity.

$$\frac{dn(x)}{dt} = N - An(x) - Bn^2(x) - Cn^3(x) - \sum_{i=1}^{N_{modes}} g_i n(x)(\vec{I}_i(x) + \overleftarrow{I}_i(x)) \tag{4.1}$$

$$\frac{d\vec{I}_i(x)}{dx} = +g_i n(x)\vec{I}_i(x) + \frac{\beta Bn^2(x)}{N_{modes}} \tag{4.2}$$

$$\frac{d\overleftarrow{I}_i(x)}{dx} = -g_i n(x)\overleftarrow{I}_i(x) + \frac{\beta Bn^2(x)}{N_{modes}} \tag{4.3}$$

The meanings of the variables are listed in Table 4-1.

Equation 4.1 describes the rate of change of population inversion in terms of pumping rate N, spontaneous emission, nonradiative recombination, and stimulated emission. Equation 4.2 and 4.3 describes the rate of change of the optical mode intensity after light propagates an infinitesimal distance dx through gain material in the positive and negative directions respectively.

Table 4-1: Description of variables used in the travelling wave model.

N	Pumping rate (/cm^3/s)
$n(x)$	Population inversion as a function of cavity position (/cm^3)
A	Nonradiative coefficient (/s)
B	Radiative coefficient (cm^3/s)
C	Auger coefficient (cm^6/s)
N_{modes}	Number of longitudinal modes.
β	Spontaneous emission factor
g_i	Differential gain coefficient of mode i.
$\vec{I}_i(x),\overleftarrow{I}_i(x)$	Local irradiance of mode i for travelling in the positive and negative directions (/cm^2/s)

Figure 4-1 shows the schematic of the device structure used in the simulation. The light intensity propagating in the positive direction and at position x is represented by $\vec{I}(x)$ and the light intensity propagating in the negative direction is represented by $\overleftarrow{I}(x)$. The lengths of the lasing section, the control section, and the air gap are denoted by L_1, L_2 and L_g, respectively. A position just to the left of x is represented by x^-. Similarly, a position just to the right of a position L is indicated by L^+. This notation allows distinction of fields immediately before or after a plane.

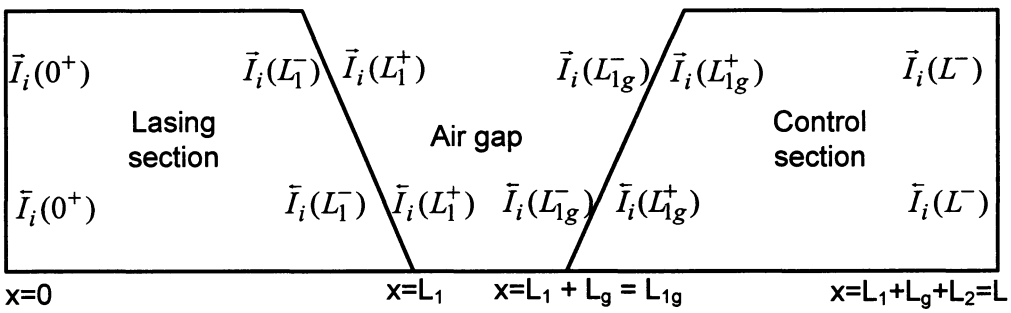

Figure 4-1 Schematic representation of the two section coupled cavity laser.

For the calculation of the mode intensities propagating in either direction inside the cavity, Cassidy[16] considered electric fields inside the resonator. The resulting expression for intensity was then integrated as a function of frequency over a region corresponding to one free spectral range of the laser resonator. Equations 4.2 and 4.3, the differential equations describing the growth of the individual modes within an infinitesimal section of the cavity length, are obtained by considering a flux of quanta of radiation in each mode that undergo a gain as they traverses the infinitesimal gain section. The mode intensity is further magnified by the addition of spontaneously emitted quanta as the mode traverses through the cavity.

A Runge-Kutta method is a numerical solution for integrating ordinary differential equations by using a phantom step at the midpoint of an interval to cancel out lower-order error terms. A second order Runge-Kutta[68] method

was employed to solve numerically the differential equations 4.1, 4.2, and 4.3. The second order formula is:

$$k_1 = hf(x_n, y_n) \tag{4.4}$$

$$k_2 = hf(x_n + \frac{h}{2}, y_n + \frac{k_1}{2}) \tag{4.5}$$

$$y_{n+1} = y_n + k_2 \tag{4.6}$$

Here $f(x_n, y_n)$ is the right hand side of Eq. 4.2 where x_n and y_n are the population inversion and light intensity respectively and h is the step distance, which is 30 μm in this case. Each laser cavity is divided into a number of sections, each of length h. The method starts by solving for the steady state population inversion at the left most position of the starting section considering spontaneous emission as the initial light intensity. To find the steady state solution, the right hand side of Eq. 4.1 was set to zero, i.e., $dn(x)/dt = 0$. A Newton root finding method was used to find the population inversion. This population inversion was used to calculate the light intensity at the midpoint of the next section using Eqs. 4.5 and 4.6. To be accurate, the population inversion is again calculated at this middle step using the newly found light intensity. The intensity of the next section is then calculated and the steps are repeated until the light intensity at the last section is obtained.

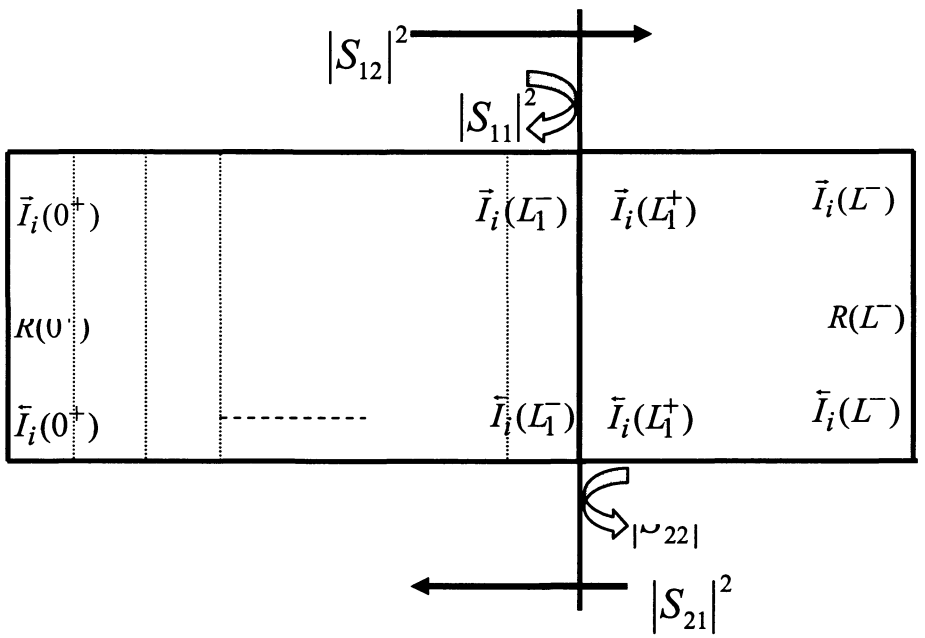

Figure 4-2 Schematic of the gap scattering matrix and boundary condition employed in the travelling wave method.

Figure 4-2 shows the same schematic of Figure 4-1after replacing the air gap with the *S*-parameters where S_{11} and S_{12} represents the reflection and transmission coefficients for the electric field of a mode looking from the lasing section while S_{22} and S_{21} represents the same looking from the control section. The scattering matrix parameters for the air gap were calculated by taking the facet angles into account. In the air gap, free space beam propagation is used assuming Gaussian beam propagation. Figure 4-2 is the schematic of the device structure that is used in this simulation. Spontaneous emission is considered as the initial light intensity $\vec{I}(0^+)$. In one round trip,

light travels from the back facet to the air gap, from the air gap to the front facet, from the front facet to the air gap and from the air gap to the back facet to complete one round trip. The reflectance of the back facet at $x = 0$ as seen by the light propagating in the negative direction is $\tilde{R}(0^+)$ and that of the front facet seen by the positive propagating light at $x = L$ is $\vec{R}(L^-)$. At each interface, boundary conditions have to be applied, which are given as follows:

$$\vec{I}_i(0^+) = \tilde{I}_i(0^+) \times \tilde{R}(0^+) \tag{4.7}$$

$$\begin{aligned} \vec{I}_i(L_1^+) &= |S_{12}|^2 \times \vec{I}_i(L_1^-) + \tilde{I}_i(L_1^+) \times |S_{22}|^2 \\ &+ 2\sqrt{\vec{I}_i(L_1^-)|S_{12}| \times \tilde{I}_i(L_1^+)|S_{22}|} \cos(\Delta\varphi_i(L_1)) \end{aligned} \tag{4.8}$$

$$\begin{aligned} \tilde{I}_i(L_1^-) &= \tilde{I}_i(L_1^+) \times |S_{21}|^2 + \vec{I}_i(L_1^-) \times |S_{11}|^2 \\ &+ 2\sqrt{\tilde{I}_i(L_1^+)|S_{21}| \times \vec{I}_i(L_1^-)|S_{11}|} \cos(\Delta\varphi_i(L_1)) \end{aligned} \tag{4.9}$$

$$\tilde{I}_i(L) = \vec{I}_i(L) \times \vec{R}(L^-) \tag{4.10}$$

The third term on the right hand sides of Eqs. (4.8-4.9) is the interference between the electric fields of the two beams. This interference accounts for the mode selectivity of the coupled cavity laser. The $\Delta\varphi_i(L_1)$ term represents the phase difference at position L_1 between the electric fields for mode *i* that interfere.

At the lasing section-air gap interface, a portion S_{11} of the electric field is reflected back into the lasing section while the remaining portion enters the

air gap. At this point, for these two fields, the phases of the electric fields associated with the longitudinal modes are assumed to be the same and can be taken as a reference phase. The $\vec{I}(L_1^+)$ beam travels through the air gap and enters into the control section. After one round trip through the control section, this beam adds with the reflected beam at the lasing-section air-gap interface. The phase of the electric field of this beam will undergo change because of its travel through the air gap and control section. The phase change due to the travel in the air gap is taken into account by the air gap *S*-parameters. The phase change due to the round trip travel in the control section is taken into account by adding a phase term $\phi_i = 2k_i\eta_i L_c$ to the reference phase components of each mode. Here k_i, η_i and L_c are the wave vector of the i^{th} mode, the refractive index of the i^{th} mode, and the length of the control section, respectively.

The addition of the beams with different phases for the electric fields will result in wavelength dependencies for each mode. The effect of the control section on the mode selectivity can also be treated by an effective reflectivity[60] which replaces the air gap and the control section with a single surface. The travelling wave method that I employ does not use an effective reflectivity for the air gap and control section, and is accurate since it explicitly takes into account in a self consistent manner the effects of the control cavity, including gain and loss of the beam as it propagates through the control

section. An effective reflectivity model does not include self consistently the gain or loss for propagation through the control section.

After the application of boundary condition at the back facet, i.e., after one round trip, a chi-squared (χ^2) criterion was used to determine whether the simulation had reached steady state or not. χ^2 was defined as $\chi^2 = \sum_{i=1}^{N_{modes}} (\bar{I}_{i,m} - \bar{I}_{i,m-1})^2$ where $\bar{I}_{i,m}$ stands for the light intensity in the negative direction for the i^{th} mode of the m^{th} iteration. χ^2 is compared to a precision value (10^{-4} in this calculation) and iteration continues until the precision is met.

A flow chart for solving the travelling wave equations used for the simulation of a two-section coupled cavity semiconductor laser is given in Table 4-2. Initial guesses for the optical power at the beginning of the simulation are taken to be the spontaneous emission. Pumping rates for lasing and control section are defined as K_1 and K_2. For a fixed K_1, K_2 is varied in order to look for the change in emission wavelength.

Table 4-2: Flowchart of travelling wave method for the simulation of two-section coupled cavity laser.

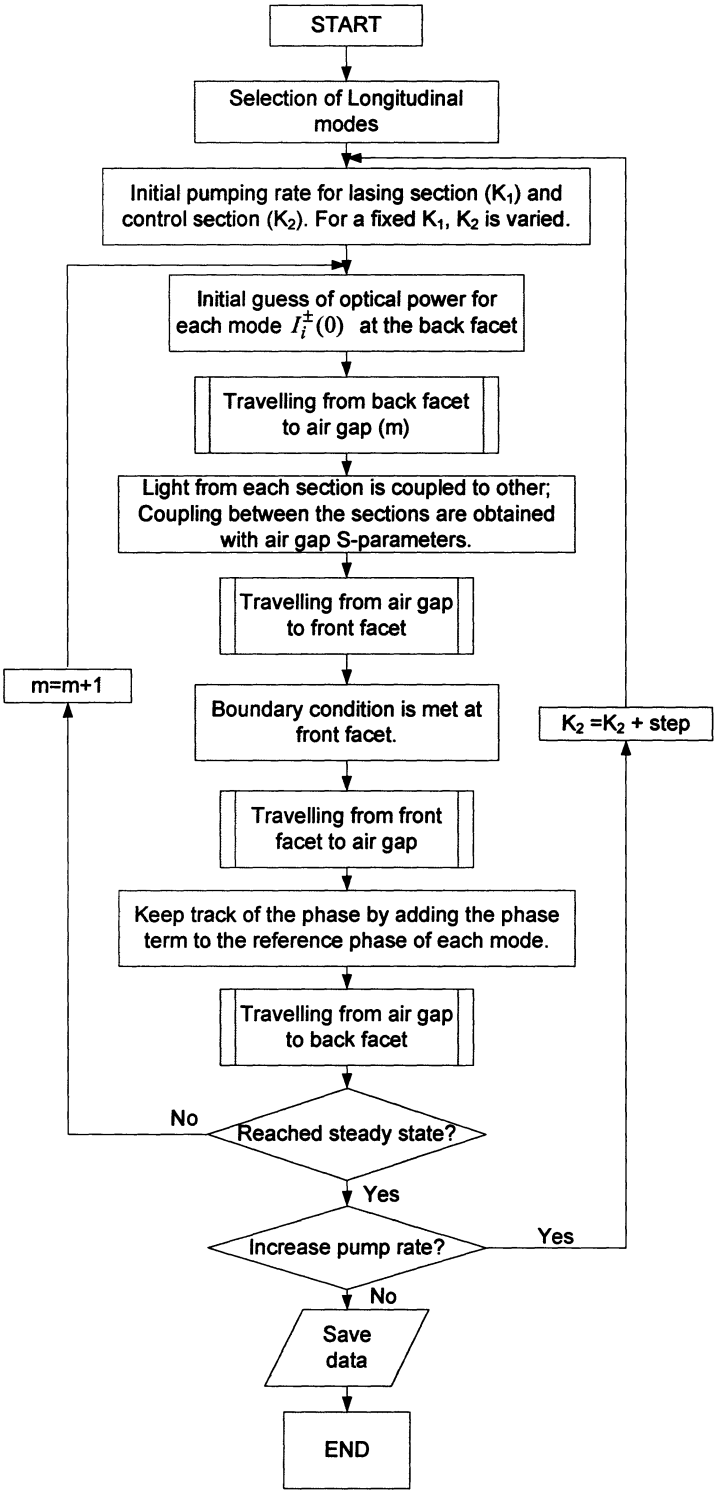

4.4. Simulations results and discussion

To imitate the electronic tuning mechanism in a coupled cavity laser, the lasing section was biased with an injection current above the threshold current (I_{th}) value while the control section was biased below I_{th}. For various fixed lasing section currents, the control section current was varied. The variation of control section current resulted in shifts of the gain peaks and hence changes in refractive indices in the control section. Light passing through the control section will undergo different phase changes for different refractive indices and as a result various sets of wavelength dependant light intensities are obtained. Figure 4-3 shows the wavelength tuning for a fixed lasing section current (I_L) while the control section current (I_C) was varied. By varying I_C only, not all the modes could be selected, but by varying both I_C and I_L, all possible modes could be selected as shown in Figure 4-4. Note that the colors were reused in this case to accommodate all the modes. For each fixed I_L, I_C was increased in 20 equal steps and the gain peak followed with a red shift for each of the increments, but the selection of coupled cavity modes did not necessarily always follow the direction of the shift of the gain peak. The numbers above the selected modes in Figure 4-3 shows the step number of I_C for which that mode is reinforced by the coupled cavity resonator and is dominant. Calculation shows that the selected mode has the highest RG product for that

particular I_C. Similar tuning behavior with changes of the currents was also observed experimentally.

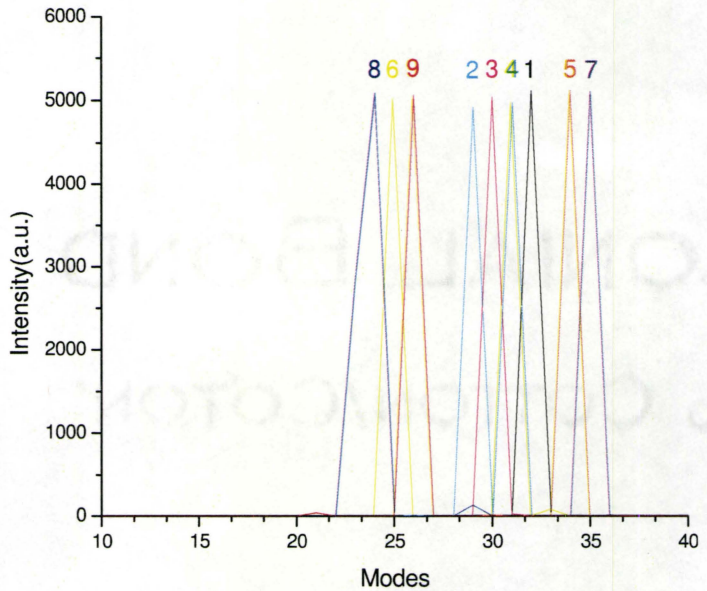

Figure 4-3 Simulation of wavelength tuning by a coupled cavity laser with varying I_C and fixed I_L.

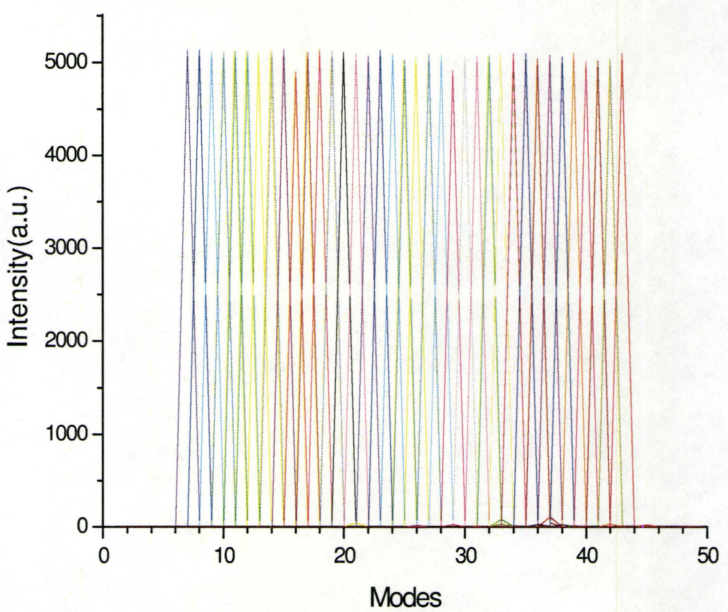

Figure 4-4 Simulation of wavelength tuning by a coupled cavity laser (whole range).

Figure 4-5 shows the selected wavelengths of a cleaved coupled laser when I_C was varied for a fixed I_L. Note that the modes do not appear in sequence, similar to the results of the simulations.

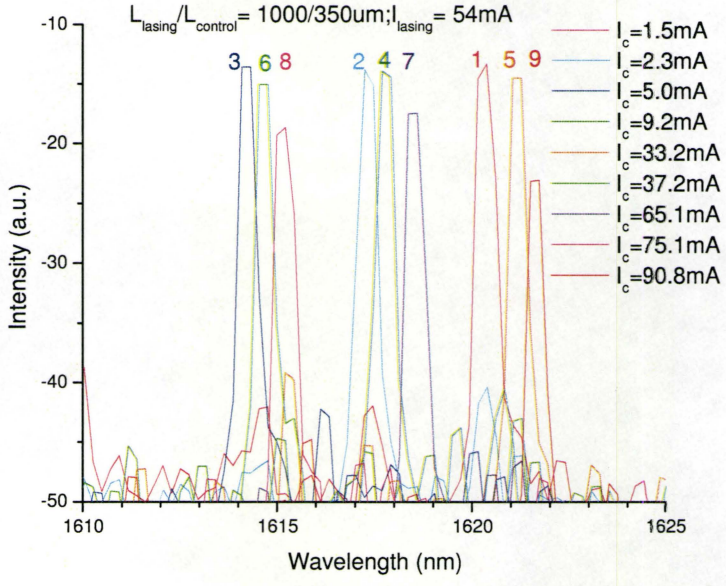

Figure 4-5 Experimental wavelength tuning by a coupled cavity laser with varying I_C and fixed I_L.

From the simulation it was observed that when the control section current was changed to a new value, the new mode can reach its steady state value in ~100 roundtrips which means that switching is possible in the ~1 ns range. Fast electronic wavelength switching together with broad tuning range allows AMQW coupled cavity lasers to achieve fast sweeps of wavelength over a broad tuning range.

Figure 4-6 shows the comparison between the simulated and measured L-I curve of a two section coupled cavity diode laser. The dotted curve refers to the measured L-I curve. For the simulation of the L-I curve, fifty one longitudinal modes were considered and the total power for all the modes was calculated as a function of pumping rate. The lasing section current was varied for a fixed control section current.

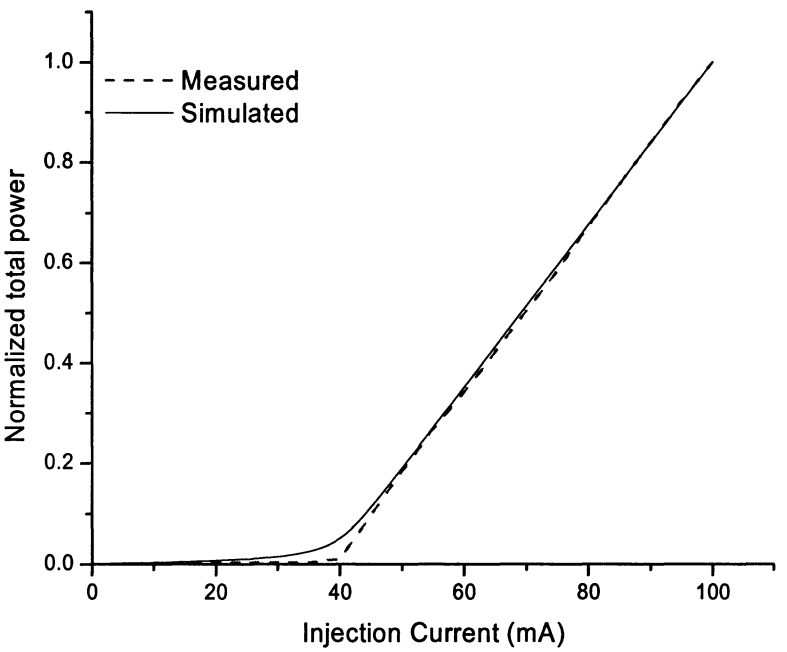

Figure 4-6 Comparison of simulated and measured L-I curves.

The goal of the model was not to estimate the total output power hence the total power is shown in a normalized form. Lengths of the lasing and control sections were taken as 900 and 300 μm respectively. Ridge widths of

the laser used in the experiment and simulation were 3.4 μm and 3.0 μm respectively. From the figure, it can be observed that both cases produced similar threshold currents and conversion efficiencies.

4.5. Summary

In this chapter, I have presented the above threshold simulation of two-section coupled cavity semiconductor diode laser and have applied this to cleaved coupled cavity (C^3) AMQW lasers. The simulation uses a travelling wave approach for calculation of the lasing mode intensities. Device parameters were taken from fits to a below threshold model, which calculates the coupling between the two cavities and takes into account the non vertical nature of the walls of the air gap. The travelling wave approach explicitly includes the effects of both cavities, which includes both amplification/loss and mode selectivity, and hence is more realistic than other models that use only a rate equation method or effective reflectivity in predicting the optical power. The simulations verified the electronic mode selection mechanism for a coupled cavity laser and showed that the proper adjustment of injection current in either section allows every possible mode to be selected as well as predicts the minimum switching time between modes. These agile and broad wavelength tunable sources offer numerous applications. Some applications with a particular focus on OCT are described in chapter 5.

5. Widely tunable C^3 lasers for synthesized OCT and other applications

5.1. Introduction

In this chapter, widely tunable coupled cavity semiconductor lasers with sub-microsecond switching times between modes over the operating range of ~ 100 nm are described in detail. With appropriate modulation of injection currents and time averaging of the output light intensity, these devices provide short coherence lengths and can become an excellent source for synthesized optical coherence tomography [69](SOCT). The measured depth resolution was found to be ~15 μm for a 100 nm wavelength tuning range centered at 1580 nm. High-output power and brightness together with a short coherence length confer on these AMQW coupled cavity lasers some advantages over conventional sources for OCT. Also, a rapid wavelength switching capability allows theses lasers to be used in real-time OCT and other applications needing wavelength agile sources.

5.2. Optical coherence tomography

This section provides a brief description of the different OCT schemes available and describes how a tunable laser can be a used as a potential source for OCT.

OCT is a technique for cross-sectional imaging of biological tissues and materials. There are mainly two types of OCT, (1) time domain OCT (TD-OCT)[70] which uses a broad spectral width light source like a light emitting diode (LED) or a super luminescent diode (SLD); and, (2) Fourier domain OCT (FD-OCT)[71], which is again divided into two sub-categories depending on the light source and detection mechanisms used. One of the FD-OCT techniques is a spectral interferometric technique OCT[72] which uses a broadband light source like an SLD with a detection system consisting of a diffraction grating and a CCD array. The other FD-OCT technique[71] uses a broadly tunable laser as the light source and a normal detector for the detection of the interference fringes.

A simple OCT apparatus consists of a free space or fiber-optic-based interferometer illuminated by a light source. The two arms of the interferometer are called the sample arm (contains the sample) and the reference arm (usually a mirror). Backscattered light from the sample arm and light from the reference arm produce an interference pattern only if the optical path difference for the two arms are within the coherence length of the source. By scanning the mirror in the reference arm, depth resolution is obtained from the interference fringes as only reflectors for pathlength differences that are within the coherence length will produce fringes. Depth resolution, in both TD-OCT and FD-OCT cases, increases as the coherence length of the light source decreases. For an LED or an SLD, the depth

resolution is inversely proportional to the total spectral width whereas for a tunable laser the depth resolution is inversely proportional to the total tuning range[73]. While TD-OCT uses a broad spectral width source with a short coherence length and scans the position of a reference mirror, FD-OCT requires single frequency tuning over a broad spectral width to obtain depth resolution. An FD-OCT system with a tunable laser source can be favoured over a TD-OCT system mainly because the OCT system does not require any moving optical elements (these have been transferred to the source) like the reference mirror in a TD-OCT system and the laser source has higher brightness compared to that of an LED or an SLD and hence can be coupled efficiently to a fiber. FD-OCT systems with high scanning speed (between 25 and 38 μs) have already been commercialized by several companies[74]. In addition, the FD-OCT systems are known to have higher signal to noise ratios (SNR) than that of TD-OCT systems[75]. However, an FD-OCT laser system is difficult to construct because it requires mode hop free wavelength tuning.

There is another technique called synthesized optical coherence tomography (SOCT). SOCT belongs to the time domain OCT class and is based on the principle of synthesis of a short optical coherence function[76]. SOCT converts a coherent source with a long coherence length into an incoherent source with a short coherence length. A tunable diode laser is used in this scheme. By modulating the output wavelength over a broad spectral range and by appropriate averaging, the time-averaged optical

coherence function is delta-function-like in depth and allows for depth resolution in an imaging system[77]. While mode hopping is not a problem for SOCT as it is in the case of Fourier domain OCT, the laser source for SOCT also provides a higher power spectral density and higher brightness compared to SLDs used in time domain OCT. My goal was to develop coupled cavity sources for OCT that exhibit a short coherence length, a broad tuning range, high speed wavelength scanning, and high output power and brightness.

5.3. Synthesizing an incoherent source from a coherent source

Figure 5-1 shows the process of synthesizing an incoherent source from a coherent source. Figure 5-1 shows single mode emission for a specific set of lasing and control section currents I_{L1}, I_{C1}. This emission is in the long wavelength region of the broad emission spectrum of my cleaved coupled cavity AMWQ laser. Figure 5-2 shows the single mode emission for the same laser with a different set of injection currents (I_{L2}, I_{C2}). This time the emission is in the short wavelength region of the spectrum. By choosing many different combinations of I_L and I_C between the sets (I_{L1}, I_{C1}) and (I_{L2}, I_{C2}), the missing longitudinal modes between the extremities of Figure 5-1 and Figure 5-2 can be obtained. This is shown in Figure 3-6 where a total tuning range of about 100 nm with nearly 100 single longitudinal modes is shown. Rapid modulation

of I_L and I_C followed by subsequent time averaging allows one to obtain effectively a broad spectral output shown in Figure 5-3.

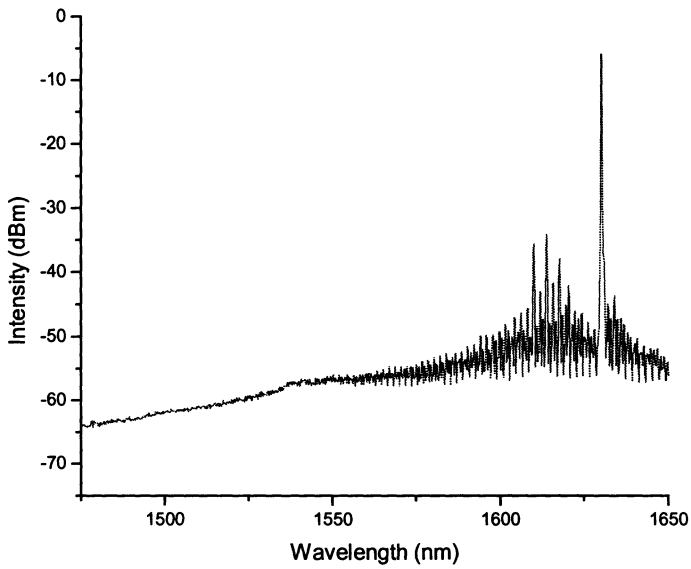

Figure 5-1 Process of synthesizing an incoherent source: single mode emission in the long wavelength region.

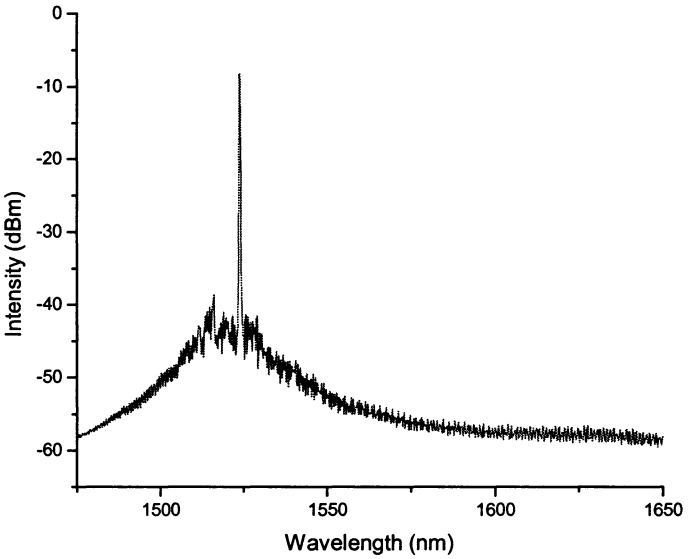

Figure 5-2 Single mode emission in the short wavelength region.

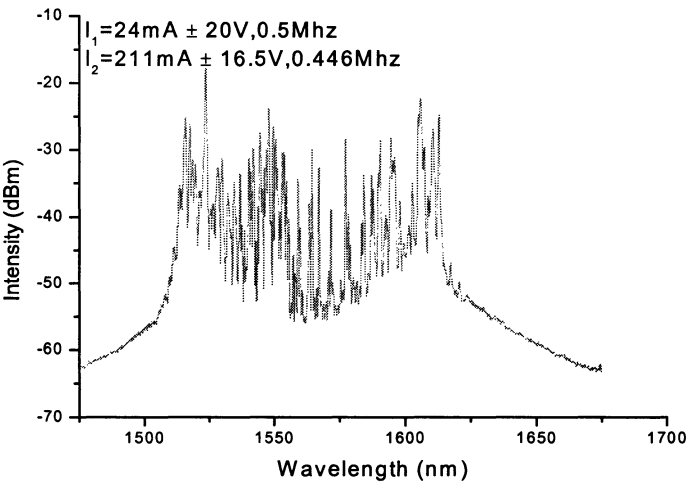

Figure 5-3 Modulation of I_L and I_C followed by subsequent time averaging.

For each section, a triangular modulation voltage was applied on top of a dc bias. The time averaging must be performed over a time much longer than the period of the modulation voltage. The spectral width of this synthesized source is now much broader than a single wavelength emitting source like the one shown in Figure 5-1 or Figure 5-2. In fact, this new source has a time averaged broad spectral width similar to that of an SLD or LED, but the synthetic source has a much improved optical power and brightness enabling one to construct a TD-OCT system without worrying much about the optical power and brightness of the source. The next two sections describe the experimental details for fast switching of longitudinal modes and measurement of coherence length respectively.

5.4. Fast wavelength switching

A time resolved spectral measurement technique based on a monochromator and a fast detector was used for studying the wavelength switching behavior of the widely tunable AMQW C^3 lasers. Figure 5-4 shows a schematic diagram of the experimental setup for time resolved spectral measurements. The control section was ac modulated about a dc bias.

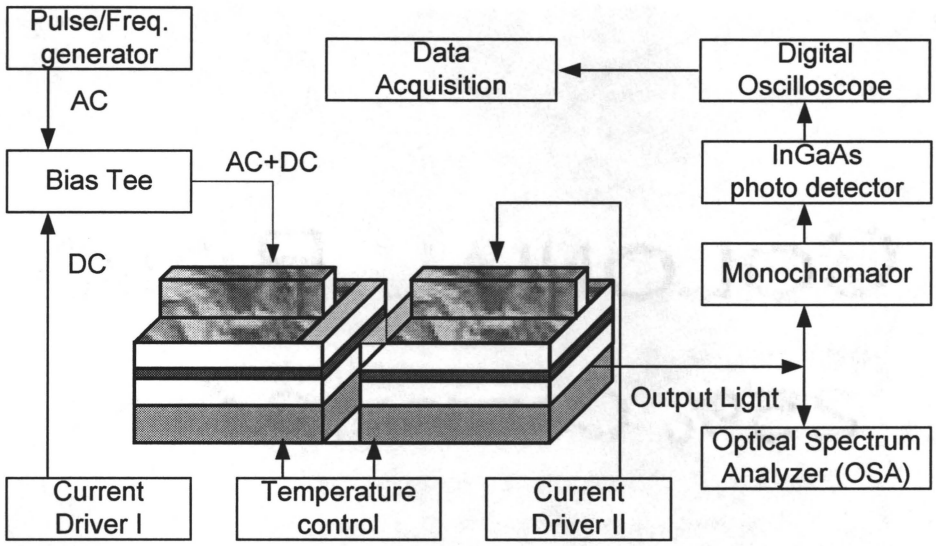

Figure 5-4 Schematic block diagram of the experimental set-up for time-resolved spectral measurement.

A bias tee (Picosecond pulse model 5555) was used to combine the ac and dc current. A function generator (Fluke PM5139) was used to supply the ac current while a current driver (ILX LDC 3900) was used for the dc current. A thermoelectric cooler was used to keep the temperature of the laser mount at 14°C. Output light from the lasing section was fed into a Jarrell Ash half meter monochromator. The wavelength dispersed light was collected by a high speed InGaAs photo detector (Thorlabs PDA 400). The electrical signal from the photo detector went into a 100 MHz digital oscilloscope (HP 54600 A). Finally, the oscilloscope output was fed into a computer for data acquisition. The output light could also be collected by an Anritsu MS9710C Optical Spectrum Analyzer (OSA) through a single mode tapered fiber.

For given lasing and control section dc currents (I_{L1}, I_{C1}), a longitudinal mode is selected by the coupled cavity structure. Changing I_{C1} to I_{C2} ($I_{C2} > I_{C1}$) with fixed I_{L1} will change the lasing mode. At first, two lasing modes λ_1 and λ_2 were selected for sets of currents (I_{L1}, I_{C1}) and (I_{L1}, I_{C2}) respectively. Then the control section dc current was set to a mid value between I_{C1} and I_{C2}, i.e., $I_{mid}=(I_{C1}+I_{C2})/2$. A square wave current pulse of amplitude $I_{ac}=I_{C2}-I_{mid}$ was then applied at the ac terminal of the bias tee. This allowed the control section to be modulated with a square wave pulse train with amplitude levels $I_{mid}+I_{ac}=I_{C2}$ and $I_{mid}-I_{ac}=I_{C1}$. Hence, the output light switches between λ_2 and λ_1. As the laser output is passed through a monochromator, the diffraction grating inside the monochromator introduces an angular dispersion between λ_1 and λ_2. The photo detector collects light of one of the two wavelengths for two different angular positions of the diffraction grating. The detector output for the two grating positions are saved and when combined, results in a time resolved spectral measurement of the coupled cavity laser.

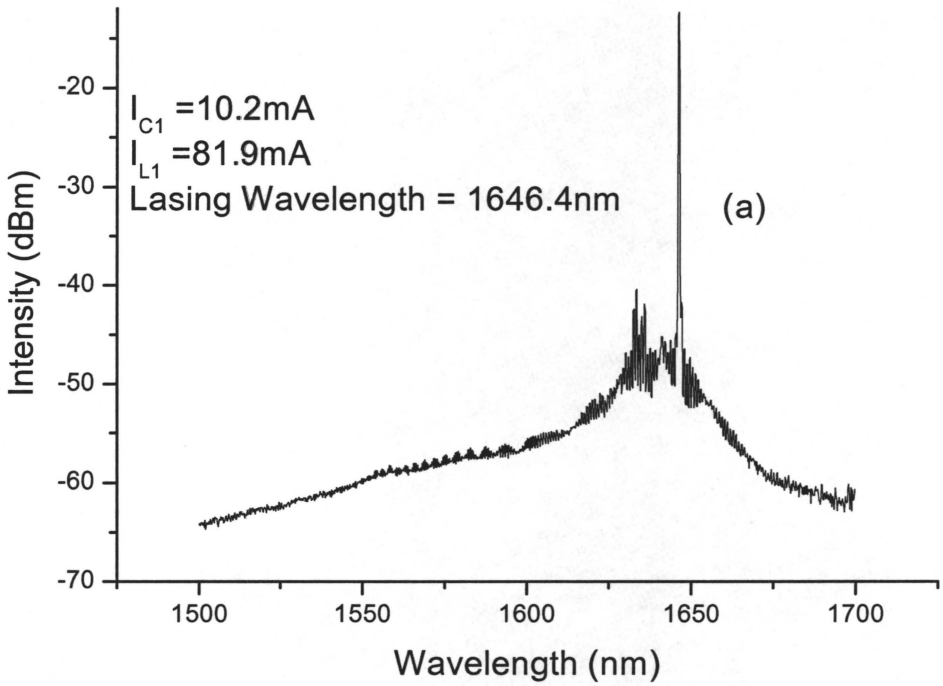
I_{C1} =10.2mA
I_{L1} =81.9mA
Lasing Wavelength = 1646.4nm
(a)
Intensity (dBm)
-20
-30
-40
-50
-60
-70
1500
1550
1600
1650
1700
Wavelength (nm)

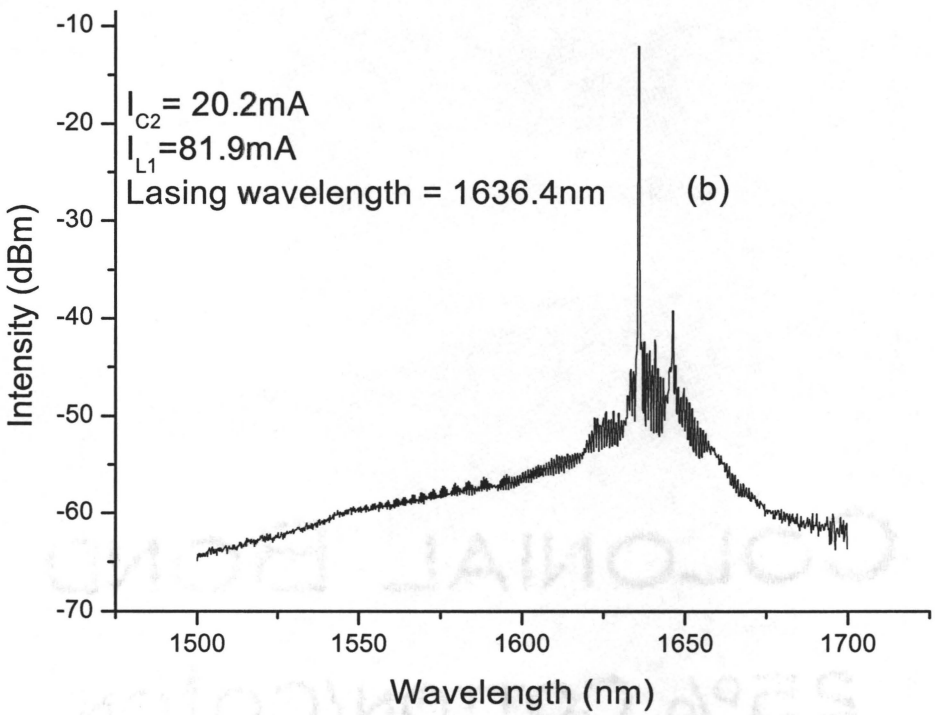
I_{C2}= 20.2mA
I_{L1}=81.9mA
Lasing wavelength = 1636.4nm
(b)
Intensity (dBm)
-10
-20
-30
-40
-50
-60
-70
1500
1550
1600
1650
1700
Wavelength (nm)

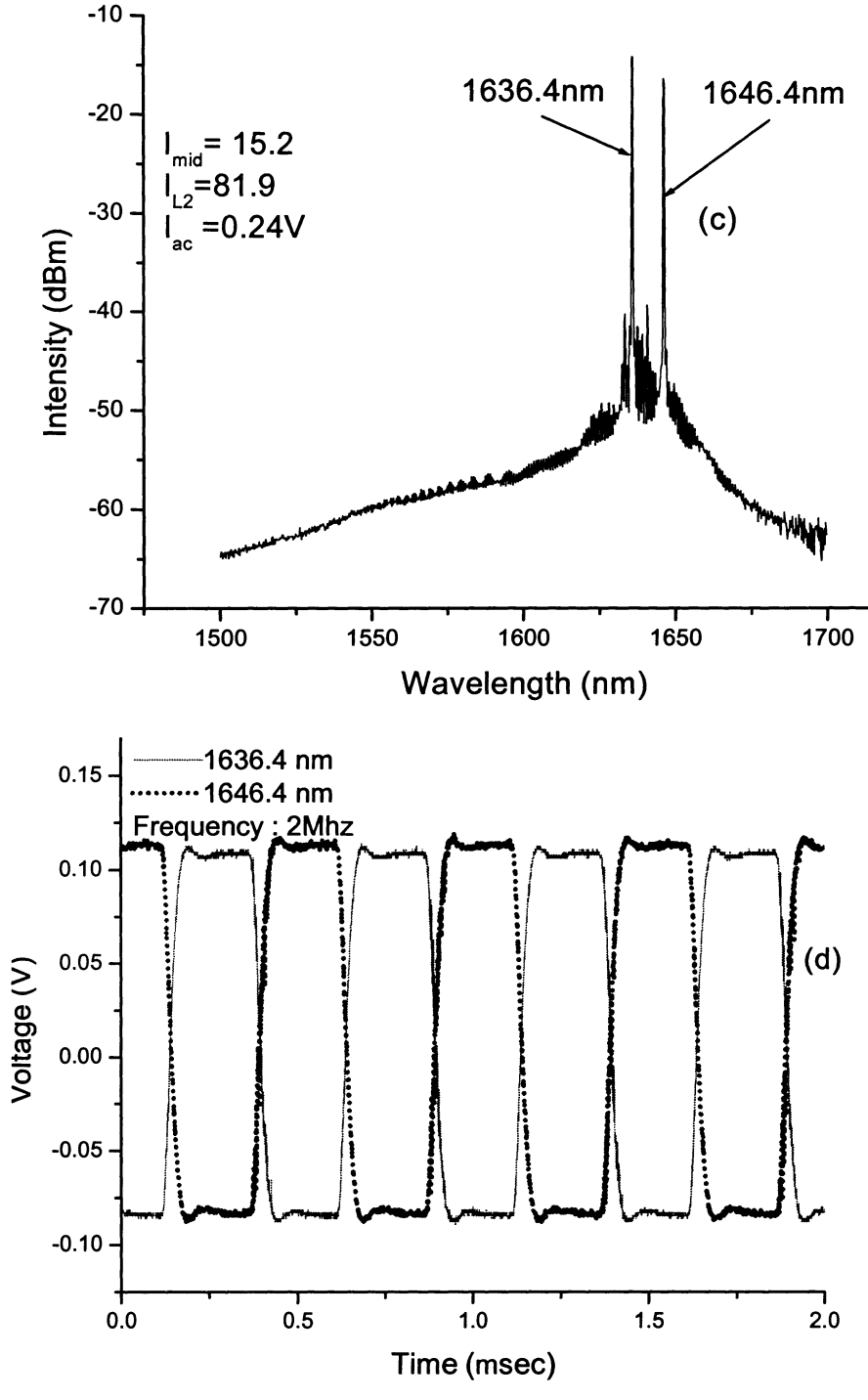

Figure 5-5 Spectral measurement (a), (b), (c) and (d) time resolved spectral measurement at 2 MHz for a 10 nm wavelength switch.

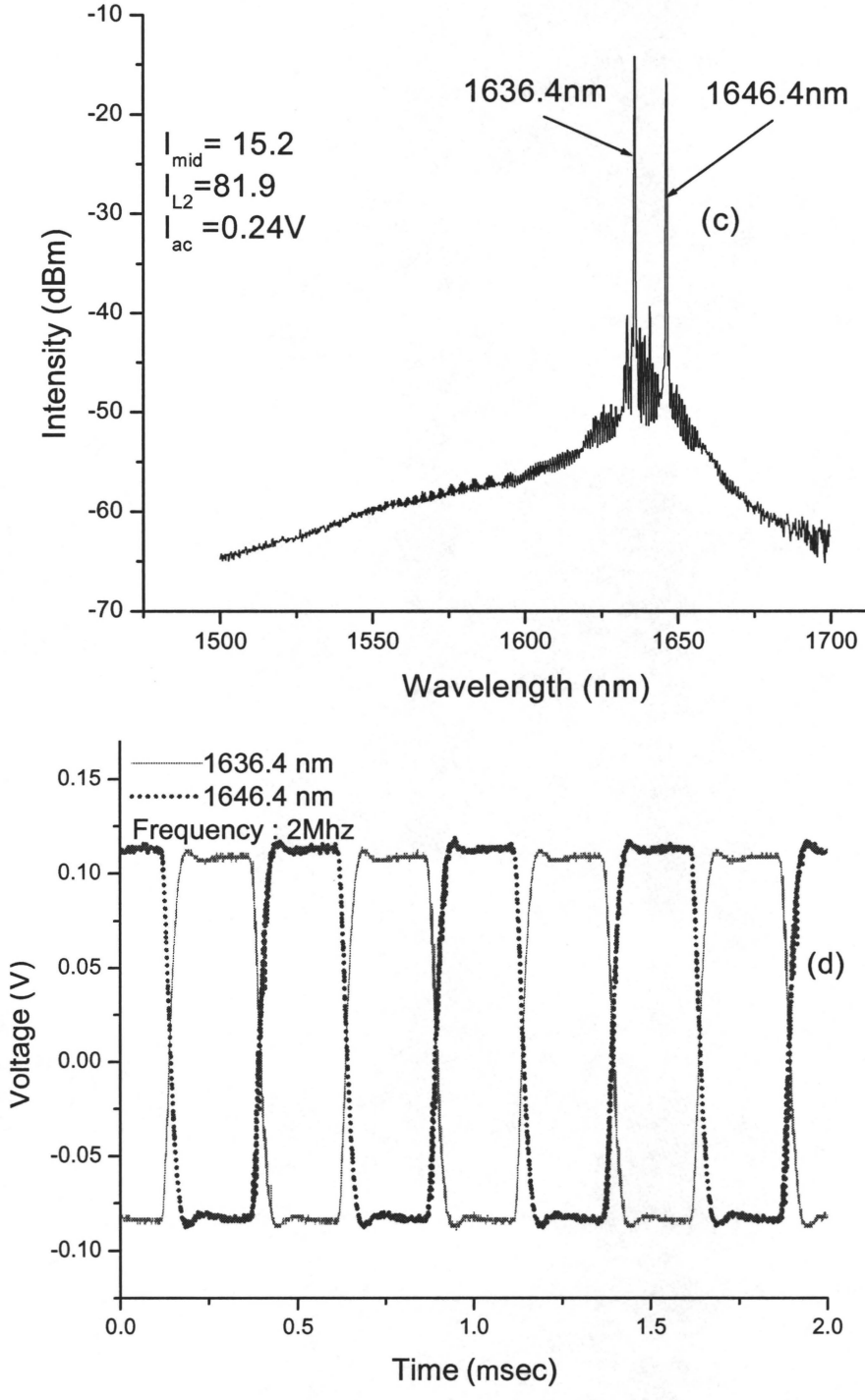

Figure 5-5 Spectral measurement (a), (b), (c) and (d) time resolved spectral measurement at 2 MHz for a 10 nm wavelength switch.

Figure 5-5 (a) and (b) show the spectral measurement for two sets of control and lasing section current with no ac component. Each set produces a single mode output spectrum. Figure 5-5 (c) shows the spectrum when the injection current of the control section is modulated with a 2 MHz square wave pulse on top of the dc bias. Only the two wavelengths are observed in this situation with a SMSR of ~ 30 dB. Figure 5-5 (d) shows the time resolved spectral measurement when modulated at 2 MHz. The voltage pulse used for modulation in this case has a peak to peak value of 0.24 V causing a 10 nm wavelength switch.

Figure 5-6 (a) and (b) show the time averaged spectrum and time resolved spectral measurement for a wavelength switch of 55 nm (1600 nm – 1545 nm) corresponding to the red and blue QWs used in this laser structure. A switching time of < 100 ns was observed, and this measurement was limited by the rise and fall time of the photo detector. It should be mentioned that the C^3 device used here has a total tuning range of ~100 nm (1625 nm – 1525 nm) and hence I expect that a >55 nm wavelength switch can easily be achieved simply by increasing the modulation voltage amplitude. A couple of transient modes are observed while the injection current goes from high to low but in the opposite direction the transient modes are not present. At the rising edge of the pulse, there is a rapid band filling effect that causes the gain peak to blue shift to 1545 nm. At the falling edge, shifting of the mode selection in

the coupled cavity is dominated by the slow dissipation of the heating caused by the large value of the current pulse.

The switching speed was measured to be ~70 ns. The measurement of switching speed was limited by the bandwidths of the detector and of the signal generator. This switching speed is an upper limit of the switching time, and is slow compared to the several GHz modulation frequency response achieved from AMQW lasers[78]. The bandwidth of the detector (~15 MHz at the lowest gain setting of the detector) set the maximum measurable wavelength switching ability of this experiment.

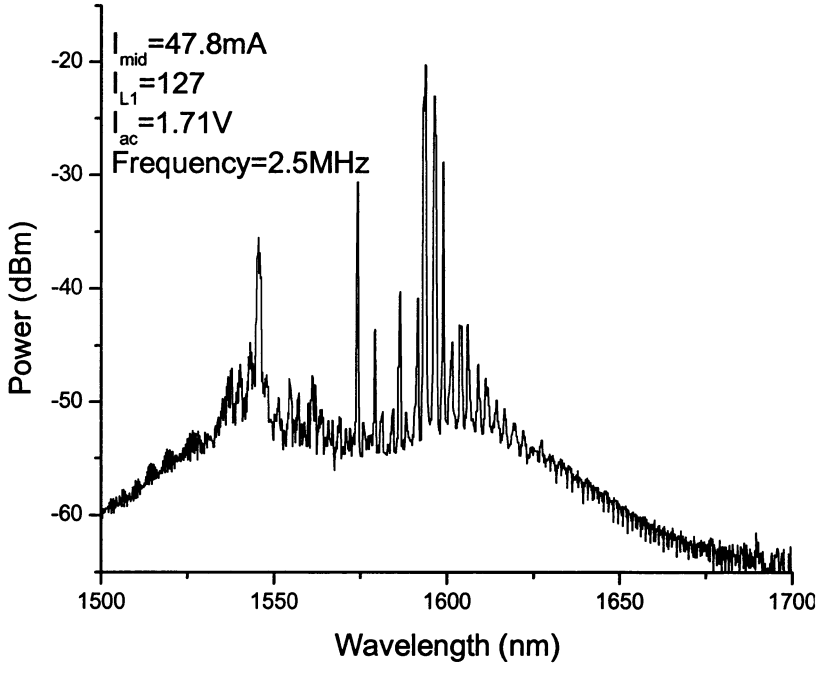

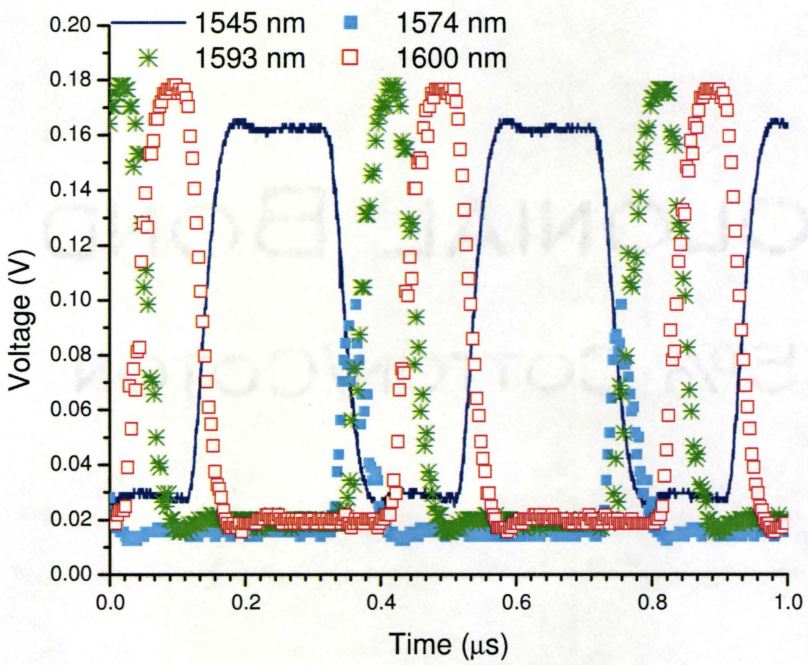

Figure 5-6 (a) Time averaged and (b) time resolved spectral measurement with 2.5 MHz modulation obtaining 55 nm wavelength switch.

5.5. Measurement of coherence length

The test bed for OCT measurements, which was used to measure the coherence length and the suitability of the SOCT AMQW C^3 source, is schematically shown in Figure 5-7. The set up mainly consists of the source, an interferometer with a reference and an object mirror, a photo detector, and a lock-in amplifier. The lock-in amplifier was used as a low pass filter to time average the signal from the detector. Here both sections of the laser are modulated in order to obtain as broad a spectral output as possible. Each section uses a bias-tee to combine ac and dc current components.

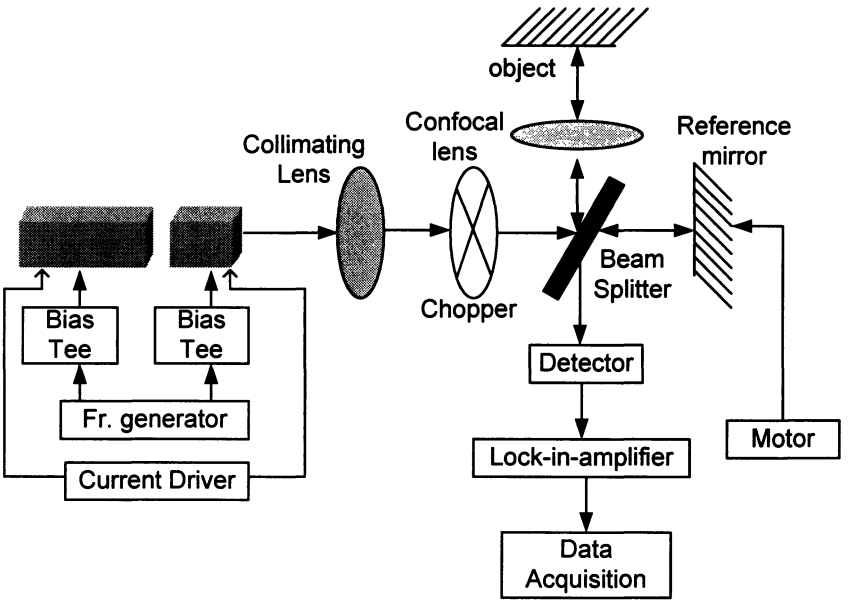

Figure 5-7 Schematic experimental set up of SOCT with widely tunable coupled cavity laser.

A triangular modulation was used on each laser section to create an approximately linear change of the injection current. This was found to provide the many different combinations of lasing and control section currents necessary to achieve as many lasing modes as possible and hence broad time averaged spectra. To fill in the gap between the short and long wavelength emissions, both sections were modulated, which results in a broad time averaged spectrum as shown in Figure 5-3. Note that each set of control and lasing section currents does not necessarily produce a single mode emission. While this simple modulation scheme is good for SOCT, a much more stringent scheme is required for Fourier domain OCT where each set of lasing and control section currents must produce single mode emission.

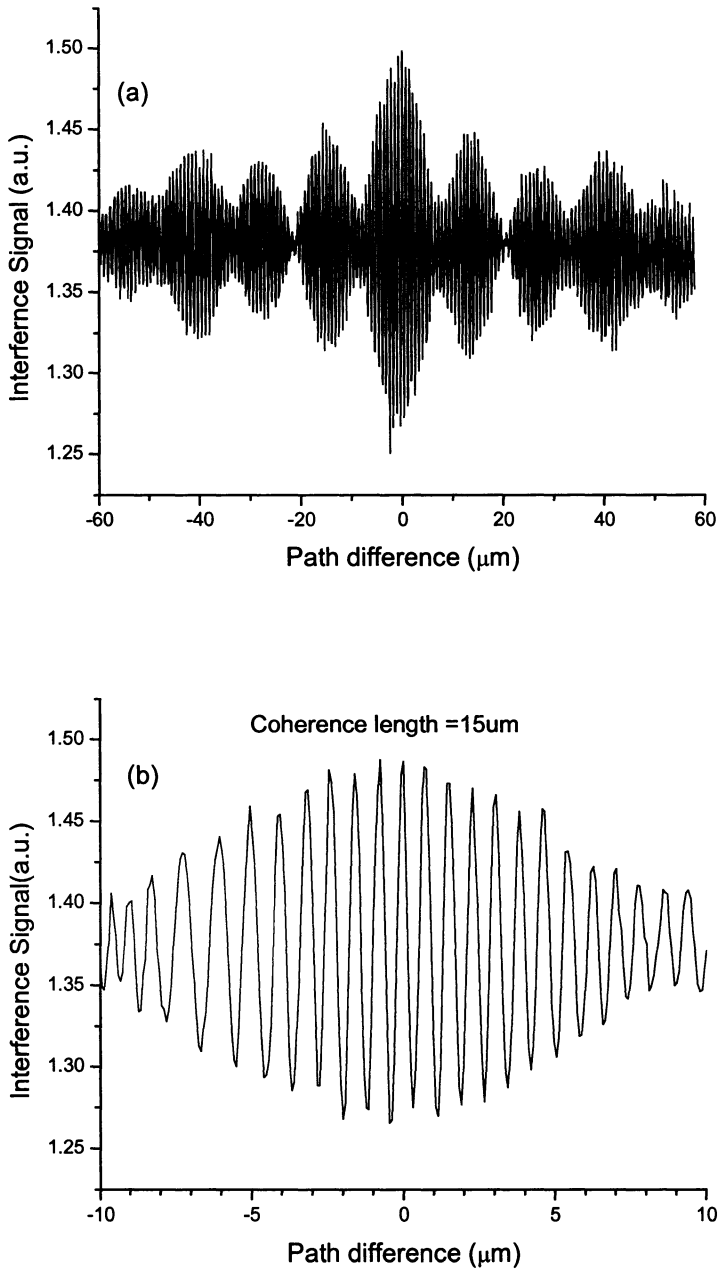

Figure 5-8 (a) (a) Interferogram over a path difference of ± 60 μm (b) Interferogram over a path difference of ± 10 μm.

In time domain OCT and SOCT, the depth information is obtained by scanning the reference mirror and by recording the interference signal. The depth resolution δz for OCT is the physical distance between two just resolvable reflectors and is given by[77]

$$\delta z = \frac{c}{n_g}\frac{\delta\tau}{2} \tag{5.1}$$

where n_g is the group refractive index of the sample, which in this case is air, $\delta\tau$ is the coherence time and is given by[73]

$$\delta\tau = \int_{-\infty}^{\infty} |\gamma(\tau)|^2 d\tau \tag{5.2}$$

Here $\gamma(\tau)$ is the complex degree of coherence and is defined as the normalized autocorrelation of the analytic field that describes the output of the source:

$$\gamma(\tau) = \frac{\Gamma_{11}(\tau)}{\Gamma_{11}(0)} \tag{5.3}$$

The autocorrelation function $\Gamma_{11}(\tau)$ is the Fourier transform of the power spectral density (PSD) of the source and equals $\Gamma_{11}(\tau) = \int_0^{\infty} 4S(\nu)e^{-2j\pi\nu\tau}d\nu$ where $S(\nu)$ is the PSD of the source. From Eq. 5.1 it is evident that depth resolution is proportional to the coherence length. $\delta\tau$ depends on the shape of the PSD. $\delta\tau$, as calculated from Eq. 5.2, is given by $\delta\tau = 0.664/\Delta\upsilon$ for a Gaussian shaped PSD and $\delta\tau = 1/\Delta\upsilon$ for a rectangular PSD, where $\Delta\upsilon$ is the FWHM of

the source. For a AMQW C^3 laser with a total tuning range of 100 nm centered at 1580 nm, the theoretical coherence length for a source with a Gaussian shaped PSD is about 9 μm while that of rectangular PSD is about 13 μm.

Table 5-1: Parameters for different light sources used in OCT.

Light Source	Center Wavelength (nm)	Bandwidth (nm)	Coherence length (μm)	Coherent power (mW)
SLD	675	10	20	40
SLD	820	50	6	30
SLD	1300	35	21	10
SLD	1550	70	15	5
LED	1300	40	17	0.1
ASE fiber sources	1550	80	13	40

OCT systems require the emission of the light source to be in the near infrared region, which stems from the need for adequate penetration of light into tissue, absorption of the sample, and the maximum possible light exposure at this wavelength. Table 5-1 lists the characteristics of some of the light sources used in OCT systems[79]. Emission wavelengths vary from 600

nm – 1800 nm depending on the type of tissues to be scanned. However, based on the absorption characteristics, high irradiance and low cost, the most commonly used sources to date are SLDs with emission wavelengths at 800 and 1300 nm[80].

Figure 5-8 shows an interferogram with mirrors in both the object and reference arms. The lasing and control sections were modulated with triangular waves at frequencies of 0.446 MHz and 0.5 MHz respectively, limited by the frequency generator capability. Figure 5-8 (a) shows the interferogram which is the Fourier transform of the PSD of the spectral output of the source with a path length difference of ± 60 μm and Figure 5-8 (b) shows the measured coherence length to be about 15 μm, if one takes the FWHM of the main lobe in Figure 5-8 (a) as a measure of the coherence length of the AMQW C^3 SOCT source.

For a rectangular PSD, as shown in Figure 5-9 (a), the envelope of the interferogram, which is the inverse Fourier transform of the PSD, has the form of a sinc function, as shown in Figure 5-9 (b). From a comparison of Figure 5-8 (a) and Figure 5-9 (b), it is observed that the interferogram of Figure 5-8 (a) does not have the form of a sinc function; the side lobes of the interference fringes have values comparable to the main lobe. Ideally one would like to have an interferogram in the form of a delta function, which would provide one reflection from each reflector in the depth scanned by the OCT system. In our

case, side lobes associated with the interferogram will also cause additional reflections for each reflector and this will produce 'echoes' of the original reflection.

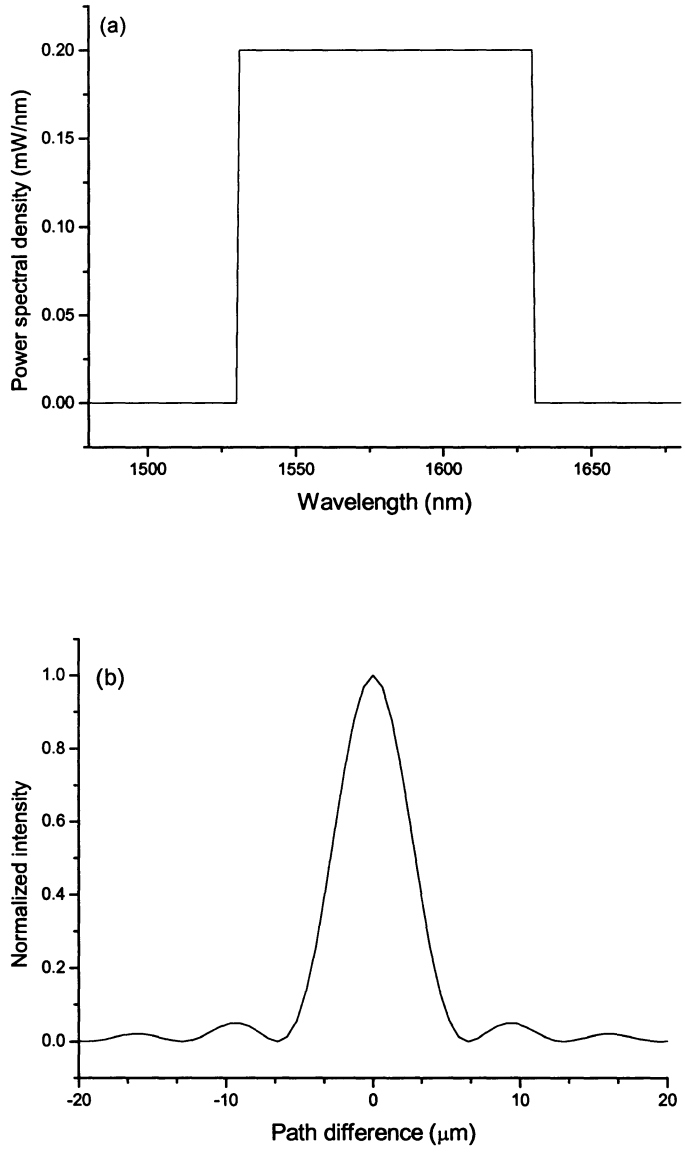

Figure 5-9 (a) PSD with an ideal rectangular shape (b) Magnitude squared of the Fourier transform of the rectangular PSD in (a).

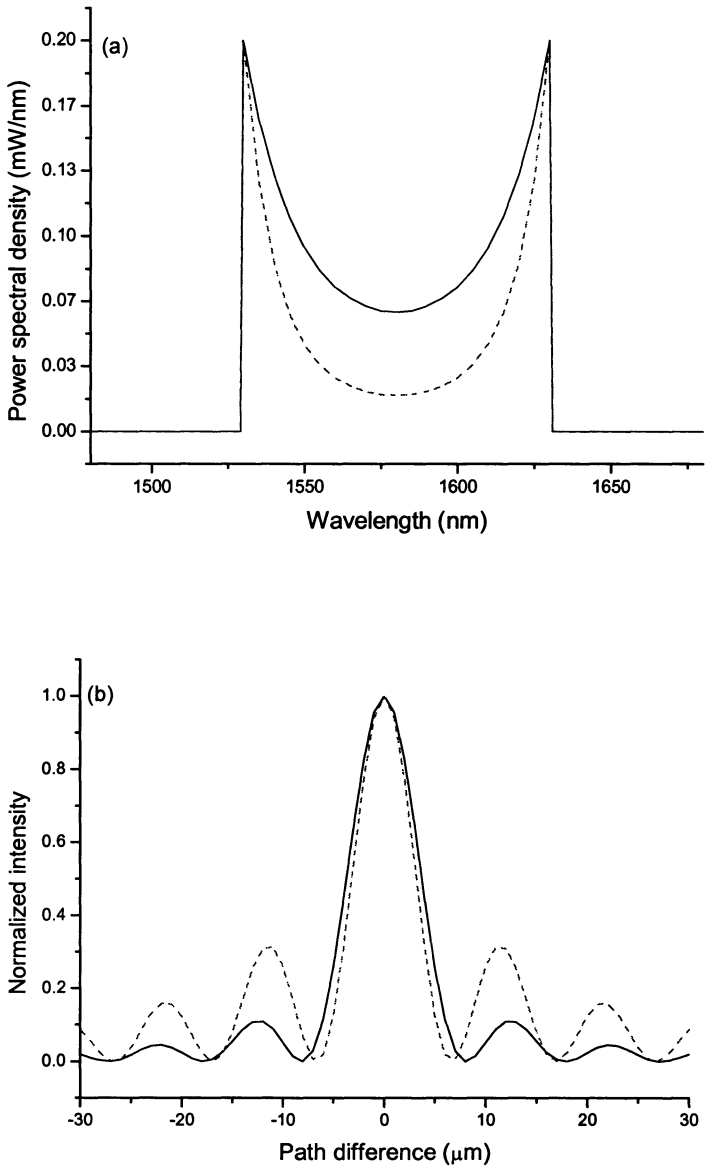

Figure 5-10 (a) PSD with non rectangular shapes (b) Magnitude squared of the Fourier transforms of the PSDs in (a).

Reconstruction of the image is possible by OCT image processing using blind[81] or non-blind[82] deconvolution techniques. Both methods require the point spread function (PSF) of the OCT system, which can be determined by

replacing the sample with a mirror, recording the interferogram, and then taking the envelope of the interference fringes. In general the degraded image $H(x)$ is written as the convolution of the object $W(x)$ and the PSF $P(x)$, i.e., $H(x) = W(x) \otimes P(x)$. Both techniques rely on iterative procedures to recover the object based on the measured image. For OCT, a blind deconvolution technique is favored because of its ability to adapt to any uncertainties that are included in the measured PSF or that are introduced by non-perfect alignment of the interferometer arms, phase front distortion by large scale index variations, inhomogeneous refractive index, and unexpected noise in the OCT system[83].

To obtain insight about what causes the side lobes of the interferogram recorded with the SOCT source, a rectangular PSD with a dip in amplitude in the middle as shown in Figure 5-10 (a) was simulated. The shape has the same basic form of the PSD as obtained experimentally with the SOCT source, as shown in Figure 5-3. Figure 5-10 (b) shows the magnitude squared of the Fourier transform of the simulated PSD. It can be readily observed that the dip in the PSD values causes an increase of the side lobe values in Figure 5-10 (b). To estimate the intensity change of the side lobes, the total power was changed by 20 % (dotted curve in Figure 5-10 (a)) which caused a ~30 % increase of the side lobe intensity.

To determine the cause of the dip, look at Figure 3-6, which shows the spectra under dc current of the same widely tunable C^3 device with various combinations of lasing and control section dc currents resulting in different single mode emissions. The figure does not show a significant dip in the middle of the tuning range. When compared to the time averaged spectrum under modulation shown in Figure 5-3, I conclude that the dip in the PSD must originate from the modulation scheme. A different modulation waveform such as a waveform where the amplitude increases slowly for small values and increases more rapidly near the turning points of the modulation would decrease the time averaged output power for modes near the turning points of the modulation waveform and increase the time averaged output power for modes in the middle region of the tuning range.

The dip in the PSD of the SOCT is not seen as an insurmountable problem. In addition to altering the modulation scheme, the AMQW active region could be redesigned to give more gain to modes in the middle of the tuning range and thus fill in the dip, or a gain flattening optical coating on the output facets of AMQW laser could be used. Multiple layers coatings provide a wavelength dependant variation of the facet reflectance and if designed properly can enhance[84] the tuning range.

Equation 5.2 has a form similar to the equivalent noise bandwidth[85] (ENBW) of a filter where the ENBW is the bandwidth of a rectangular filter that

passes the same amount of noise power as the real filter and that has the same maximum transmittance as the real filter. In equation form,

$$ENBW = \frac{1}{|H_o|^2} \int_{-\infty}^{\infty} |H(f)|^2 df \tag{5.4}$$

where H_o is the maximum value of the transfer function $H(f)$ of the filter. To calculate the coherence time $\delta\tau$ one would replace $H(f)$ with $\gamma(\tau)$ and note that the maximum of the autocorrelation function occurs for $\tau = 0$. Here $\gamma(\tau)$ is the normalized autocorrelation of the analytic representation of the E-fields as defined by Eq. 5.3. From Eqs. 5.2 and 5.4, I conclude that a source with a dip in a rectangular PSD requires a larger FWHM than that with a flat PSD to obtain the same coherence length. From Figure 5-10, it also can be noted that a reduction of the dip (shown in Figure 5-3) will decrease the side lobes relative to the main lobe of the interferogram.

5.6. Side lobe intensity reduction

From the previous section it is apparent that in order to decrease the side lobe intensities of the coherence function, it is necessary to increase the gain for the middle wavelengths of the tuning range. First, a different modulation waveform as suggested earlier was tried. Figure 5-11 shows the schematic of the waveform used. The initial linear portion of the waveform is for generating emissions in the long wavelength region of the tuning range, the staircase

region in the middle provides various combinations of lasing and control section currents responsible for lasing emissions in the middle of the tuning range. The use of a staircase form instead of linear as was used previously is for providing the emission wavelengths of this region with more gain. The third linear portion of the waveform is for lasing emissions in the short wavelength region. The resultant coherence function obtained with this modulation waveform was not much different from that obtained using a triangular modulation waveform. This suggests that gain increment in this method is not satisfactory and an alternate method is required that will cause significant improvement of gain for the targeted wavelengths.

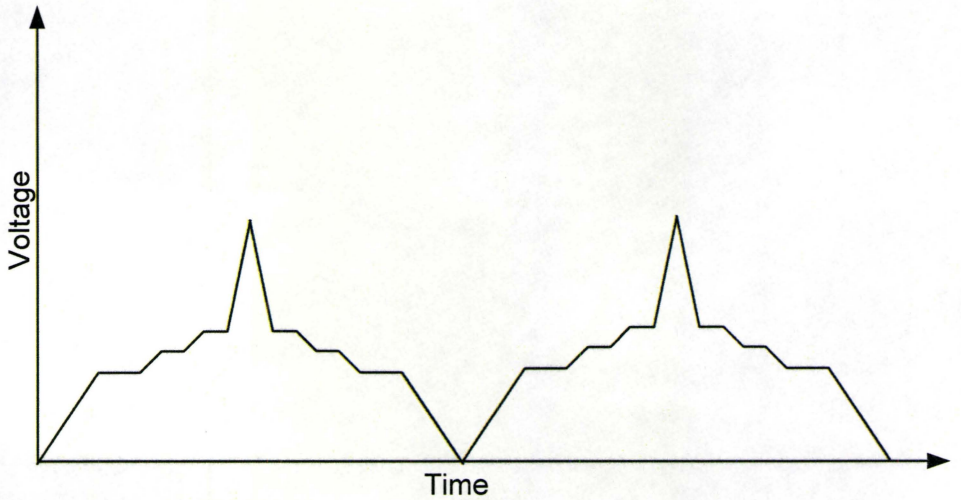

Figure 5-11 Suggested modulation waveform for increased gain to the middle wavelengths of the tuning range.

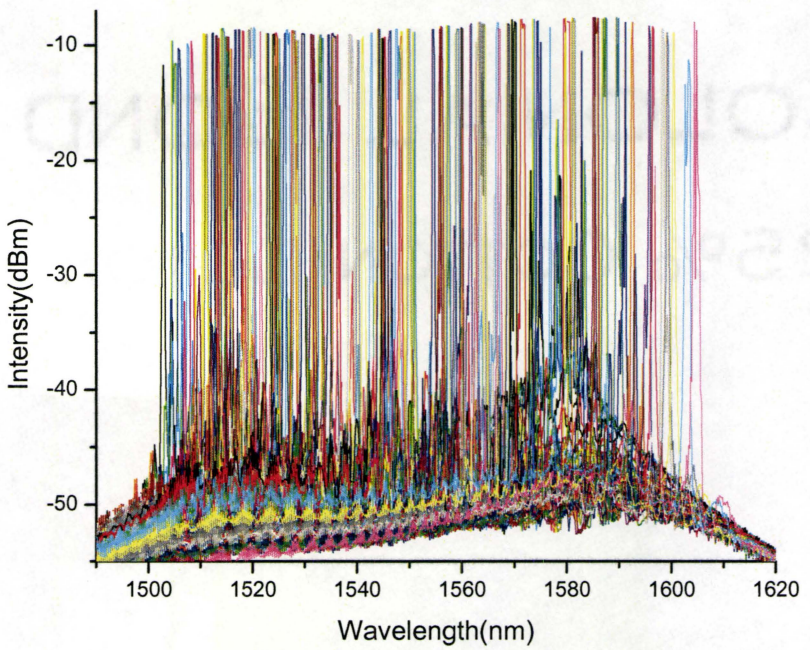

Figure 5-12 Total single mode spectrum for a AMQW laser, tuned with a DOE.

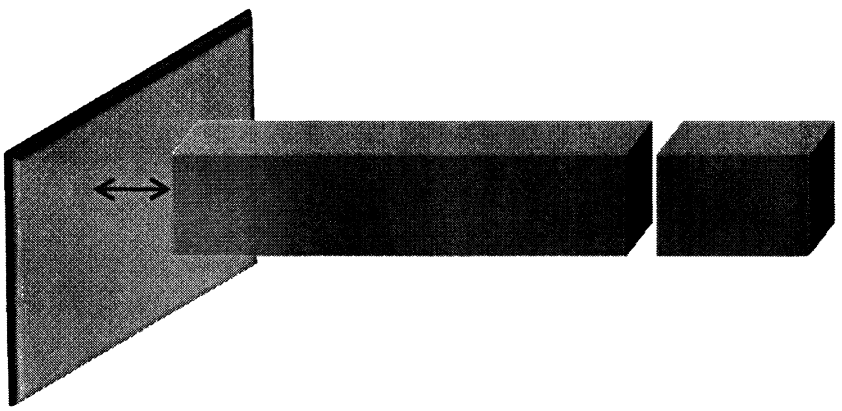

Figure 5-13 Schematic of the C^3 laser with a SXC formed by a glass slide.

Figure 5-12 shows the single mode tuning range of an AMQW laser. The length of the lasing cavity was 900 μm with a 3.0 μm ridge width. A DOE was used for the tuning of the laser. The DOE used in this work is a reflective Fresnel element with a 0.25 cm focal length centered at λ=1400 nm. It was placed at ~0.5 cm behind the back facet of the laser forming a short external cavity (SXC) with the laser cavity. The DOE SXC worked as a focusing element with high coupling efficiency into the active region as well as provided the wavelength selectivity for single longitudinal mode operation. The total tuning range in this case was also ~100 nm. Linear movement of the DOE along the optic axis produced these single longitudinal mode emissions. Comparing the electronically tuned single mode spectrum of an AMQW C^3 device as shown in Figure 3-6 and that of a mechanically tuned AMQW laser shown in Figure 5-12, I observe that whereas the modes of Figure 5-12 have nearly constant intensity, some regions in Figure 3-6 have a dip in mode

intensity. In addition, there are some regions in Figure 3-6 with missing modes. This comparison leads to believe that the RG product for the missing modes were lower than that of the adjacent ones restricting them from showing up as the emitting mode. Emission of the missing modes can be obtained by forcing an increase of reflectivity of the missing mode wavelengths.

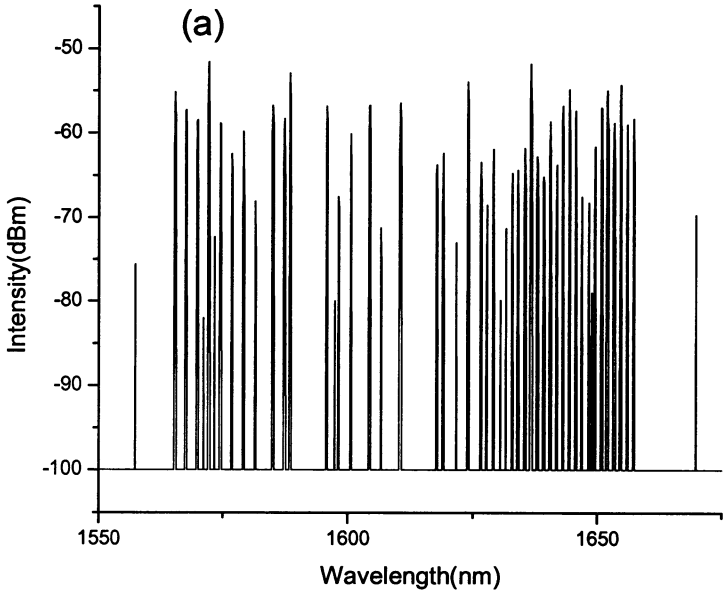

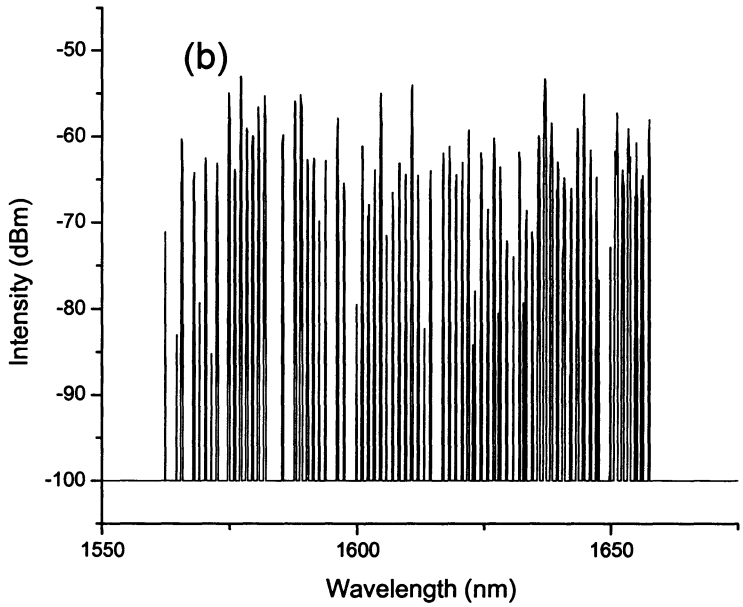

Figure 5-14 Time averaged spectrum for a C^3 laser (a) without SXC (b) with SXC.

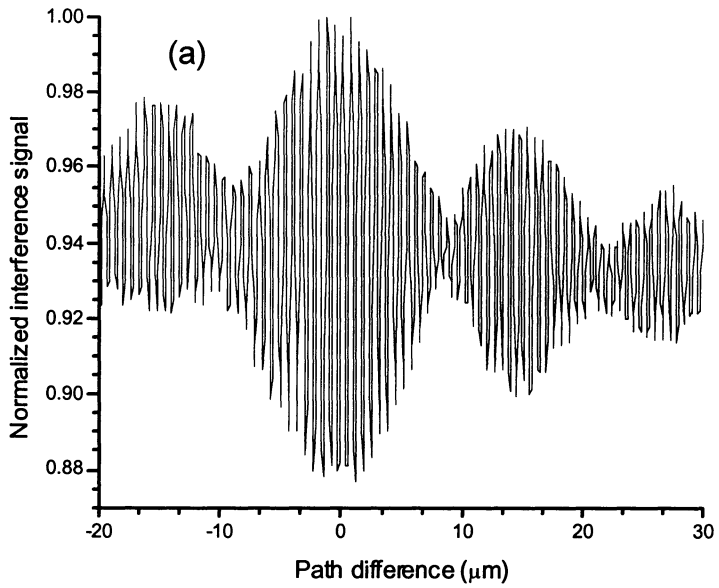

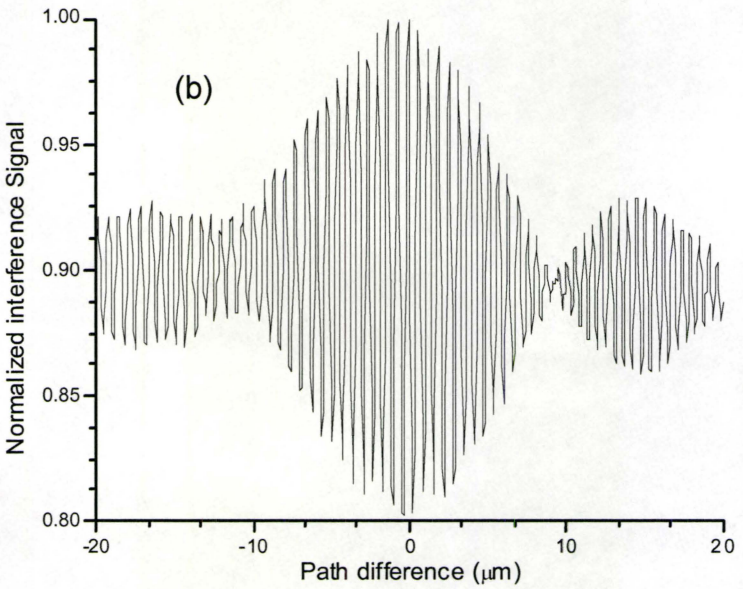

Figure 5-15 Interferogram with C^3 laser as light source (a) without SXC (b) with SXC.

An experiment was designed for the forced emission of the missing modes. A simple glass slide with ~4% reflectivity per surface was placed very close (< 10 μm) to the end facet of the lasing cavity as shown in Figure 5-13. Light coming through the slide can either be fed to an OSA or the setup that determines the coherence length of the laser. The glass slide forms a SXC with the lasing section. The modes that are common to both the SXC and the C^3 laser will have their reflectivity enhanced. For a 10 μm SXC cavity, spacing between allowed longitudinal modes is 128 nm whereas for a C^3 laser (device corresponding to Figure 3-6) with a combined cavity length of 1350 μm, the mode spacing is calculated to be 0.26 nm. Owing to the large difference in mode spacings and for reinforcing all the modes of a missing region, the glass

slide was moved along the optic axis. Figure 5-14 shows the time averaged spectrum of a C^3 laser (with modulated injection current for both sections) with or without the glass slide forming the SXC. It can be readily observed that a number of regions with no lasing emissions in Figure 5-14 (a) are now filled up with lasing modes when the glass slide is used as an SXC as shown in Figure 5-14 (b). The next step was to observe whether this improvement in the total spectral power has any effect in improving the coherence function. Similar to Figure 5-8, Figure 5-15 shows the interferograms with mirrors at both object and reference arms with the C^3 laser being used as the light source. However, in this case, the interferograms were measured with or without the presence of the glass slide forming the SXC. A 30% decrease of the side lobe intensity is observed when the external cavity was used.

5.7. Other real time applications

High speed modulation together with fast wavelength switching capability of this device should allow real time data processing in OCT and many other applications. Two applications that require a rapid and broad tunability are described in the next paragraphs.

Enshasy and Cassidy[14] described a sub micrometer distance measurement technique using a widely tunable SXC AMQW laser where the

resolution of the measurement depended on the tuning range and the number of single frequency measurements available within the tuning range of the laser. Note that continuous tuning over wavelength is not required for measurement of distance. Only measurements at selected wavelengths are required and these wavelengths can be at the modes where the AMQW C^3 laser operates single frequency. The wavelength tuning range of the SXC device that was used to measure distance was also ~100 nm on discrete modes and a resolution of 0.05 μm using 989 data points (resolution increases with number of data points) was achieved. While a higher number of data points increases resolution, measurement speed might become too slow for a real time system. Fortunately the technique is not limited to a large number of data points and as few as 7 data points can be used for a resolution of 0.55 μm. The authors used a mechanical wavelength tuning system, which resulted in a very slow wavelength scanning rate. Because of its high speed (relative to mechanical) wavelength switching ability, an AMQW C^3 device might be very useful in this regard when fast or real time distance measurement is required. By pre selecting the sets of control and lasing section currents for which a single mode is emitted, a control circuit can be made which switches the current drivers to the pre selected values. This will allow rapid switching to single mode operation over a broad spectral region.

Tiziani *et al.*[86] showed surface topology measurement using wavelength shifted speckle interferometry. They used a mechanically tunable external

cavity laser with a tuning speed of 25 nm/sec. This is again not a real time measurement. With a C^3 AMQW device one can have an increase in both scanning speed and tuning range which will enhance measurement speed and resolution respectively. This can be very useful in automotive or aircraft manufacturing industries where high resolution real time surface profilometry is required.

5.8. Summary

Results on the spectral output and coherence length of a widely tunable AMQW C^3 laser were presented in this chapter. The AMQW C^3 laser can be tuned over ~100 nm by stepping over the modes of the coupled cavity laser and by setting the injection current in the sections of the laser. Under triangular modulation, this device provided a broad time averaged spectrum, which means the source effectively functions as an incoherent source with a short coherence length. A coherence length of ~15 μm was shown, which allows the device to be used as a source for SOCT. Optical power in the range of ~15 mW together with brightness and hence ability to couple easily into fiber give this device an edge over traditional SOCT sources like an SLD or an LED. Also shown in this chapter is the wavelength switching capability of widely tunable coupled cavity semiconductor lasers. An upper limit, which was set by the response time of the photo detector, of 100 ns for the switching speed between modes of the AMQW C^3 laser was determined. As the

scanning speed can be kept higher than the video refresh rate, fast data acquisition is possible for applications such as real time surface profiling and distance measurement.

6. Conclusion

This chapter provides some suggestions for possible future work along with a summary of the work reported in this thesis.

6.1. Suggestions for future work

Although a number of studies have been carried out over the last decade on coupled cavity semiconductor lasers, none of the work has ever combined coupled cavity semiconductor lasers with asymmetric multiple quantum well (AMQW) active regions. AMQW active regions provide a much broader tuning range compared to MQW or single QW active regions.

I believe AMQW coupled cavity semiconductor lasers can become a potential choice for systems requiring broad wavelength tunability because most of the applications ask for wider tuning range from a cost effective monolithic laser without a complicated fabrication procedure. However, more work must be done to improve the understanding of these devices and to improve the functionality of these devices.

This section suggests work that might be done in the future:

The first task that should be done in the future is to develop a stable fabrication procedure for coupled cavity lasers. The main problem in terms of fabricating these device lies in the fact that while smooth and vertical air gap

walls are hard to obtain with ion milling and the etching techniques that were available to me, devices produced by cleaving technique have vertical and smooth walls but the gap angles and length are very unstable and as a result cleaved coupled lasers are produced with a very low yield. In my opinion, fabrication by etching will be required for commercial production of these devices. Inductively coupled plasma-reactive ion etching (ICP-RIE) followed by some wet chemical etching to remove the roughness of the air gap might solve the problem.

Although AMQW coupled cavity semiconductor lasers provide a broad tuning range, they do not provide stable single wavelength emission which makes them unsuitable for applications like wavelength division multiplexing (WDM) and other optical communication applications where very stable, mode-hop-free light emission is required. Sampled-grating distributed Bragg reflector (SG-DBR) or super structure grating distributed Bragg reflector (SSG-DBR) lasers, a popular implementation of electronically tunable lasers for applications in optical communications, can be fabricated using AMQW structures. They not only will provide stable emission of longitudinal modes but will also possess broad tuning ranges. It therefore would be worthwhile to pursue the development of broadly tunable SSG-DBR AMQW lasers.

In chapter five, I demonstrated the effect on tuning when an SXC was added to a two-section C^3 laser. It was shown that the SXC adds a coarse

tuning capability. Instead of the SXC formed by the glass slide, a three section coupled cavity laser can be formed by etching another slot to the output end of the lasing section. Injection current to all three sections of the laser can be simultaneously modulated to tune the whole range with the third section providing fine coarse tuning.

Finally, some extensions of both the above and below threshold models can be carried out. Addition of more than two cavities will have an effect on the coupling among the sections and can be modeled. The below threshold modes will then have to be fitted to the measured below threshold data of the coupled cavity lasers with more than two sections. The existing above threshold model can be improved by using the measured gain spectrum as its gain parameter. This will help to predict the wavelength of emission for a given set of cleaved coupled cavity (C^3) laser parameters, e.g., section lengths, injection current, and air gap facet angles. A fit of the measured lasing modes can be performed to that of the simulated one and hence some important features of the C^3 laser like total output power and linewidth of the modes can be estimated. The fine tuning feature by the use of an additional section can also be simulated and the three section structure optimized.

6.2. Conclusion

In this thesis a detailed study of coupled cavity semiconductor lasers with AMQW active regions has been carried out. The study included design, fabrication, and simulation along with some experiments demonstrating the performance of these lasers.

The design and fabrication part of the work began with the design of the optical mask used for the processing of the lasers. The lasers were processed from wafers grown with AMQW active regions. Processing the lasers was followed by fabrication of the two-section coupled cavity lasers. The main idea behind the fabrication was to take a single section device and create a slot within the length of the cavity to make the laser two sectioned. Both cleaving and ion milling techniques were used to form the gap between the sections. Both techniques have their pros and cons but they do show a common problem; the air gap side walls are not exactly vertical but are usually slanted by a few degrees.

Non-verticality of the air gap side walls affects the coupling between the sections. It was found that coupling between the sections with air gap side walls tilted by a couple of degrees is significantly different compared to the vertical side wall case. The change in coupling alters the operating characteristics of the laser. A below threshold model for a two section coupled cavity semiconductor laser using a transfer matrix method was created. The

model includes the tilt of the air gap side walls as one of the input parameters. The simulated below threshold spectral output was fitted to the measured below threshold spectral data of two section coupled cavity semiconductor lasers. A non linear fitting algorithm using a Marquardt method was integrated into the below threshold model. From the fitting results it was observed that for air gap side wall angles $\leq 4^{o}$, a two sectioned device works as a truly coupled device where the mode spacing depends on the total cavity and air gap lengths. On the other hand, for air gap side wall angles $\geq 7^{o}$, the device works as an injection locked device where the mode spacing is dependent on the length of the lasing cavity only. It appears that for angles $\leq 4^{o}$, coupling between the sections is large enough to treat the two sections as a single section. It was also shown that for angles $\leq 4^{o}$ a much better tuning capability is obtained compared to when the side wall tilts are $\geq 7^{o}$.

A simulation predicting the above threshold characteristics was also performed. A travelling wave method was chosen because of its more realistic representation of the laser cavities compared to that of rate equation method. The above threshold model takes the optimized device parameters obtained from the below threshold model as input and verifies the tuning mechanism of the widely tunable C^3 lasers. In addition, the model predicts the minimum switching time between the emitted modes as the wavelength is tuned.

Finally some experiments were designed and executed for demonstrating the performance of the C^3 lasers. Simultaneous injection of currents in each section of a coupled cavity device results in single mode emission. Various combinations of injection currents for the two sections cause different single mode emission. A total of 100 nm tuning over 100 longitudinal modes was demonstrated for AMQW C^3 lasers. For various real time applications, these modes need to be switched at a very fast rate. Limited by the detector response time, a 70 ns switching time between two longitudinal modes was demonstrated. The modes that are being switched can be from anywhere within the tuning range, i.e., both of them can be from long wavelength (i.e., red wells) or from short wavelength (i.e., blue wells) wells of the AMQW active region, or one mode can be from blue wells and the other can be from red wells.

These single wavelength emitters with long coherence length can be transformed into a short coherence length source when both sections of these device are current modulated followed by subsequent time averaging. They can be an excellent source for synthesized optical coherence tomography (OCT). Synthesized OCT belongs to the time domain OCT class. C^3 AMQW lasers are brighter and have more power than the existing time domain (TD) OCT sources like light emitting diodes (LEDs) or super luminescent diodes (SLDs). I demonstrated a coherence length of ~15 μm for a C^3 AMQW device

which originally demonstrated a maximum tuning range of 100 nm centered at 1580 nm.

A wide tunable range together with fast tuning capability enables C^3 AMQW devices to be used in many applications where real time data acquisition is required.

The results presented in this thesis are important for designing widely tunable AWQW coupled cavity semiconductor lasers for steady state operation or high speed modulation. Continued advancement in the development of the AMQW structure will result in better performance from the coupled cavity devices with larger tuning ranges and higher output powers. Progress with the design of these multi sectioned device should lead to utilization of these devices in a wide range of practical applications.

Appendix A

Table A-0-1 Partial layer parameters for 5 QW AMQW structure

Layer Type	Thickness, (A)	$In_{1-x}Ga_xAs_yP_{1-y}$		PL peak at 300 K (nm)
		x	y	
SCH	1500	0.042	0.092	
SCH	700	0.109	0.238	
Barrier	218	0.225	0.305	
Well	100	0.225	0.8	1599.1
Barrier	50	0.225	0.305	
Well	100	0.225	0.71	1458.5
Barrier	50	0.225	0.305	
Well	100	0.225	0.69	1430.4
Barrier	50	0.225	0.305	
Well	100	0.225	0.69	1430.4
Barrier	50	0.225	0.305	
Well	100	0.225	0.8	1599.1
Barrier	218	0.225	0.305	
SCH	700	0.109	0.238	
SCH	1500	0.042	0.092	

Appendix B

This is a four layer mask with colors green, black, red and yellow representing mesa, via, isolation etch and metallization mask respectively. The inverted "Z" shaped isolation etches electrically separates the two sections. The position of the isolation etch was varied in order to examine the effect of various ratios of cavity lengths as shown in Figure B-1.The designed ridge widths were 2, 2.5, 2.8, 3, 3.2, and 3.4 μm.

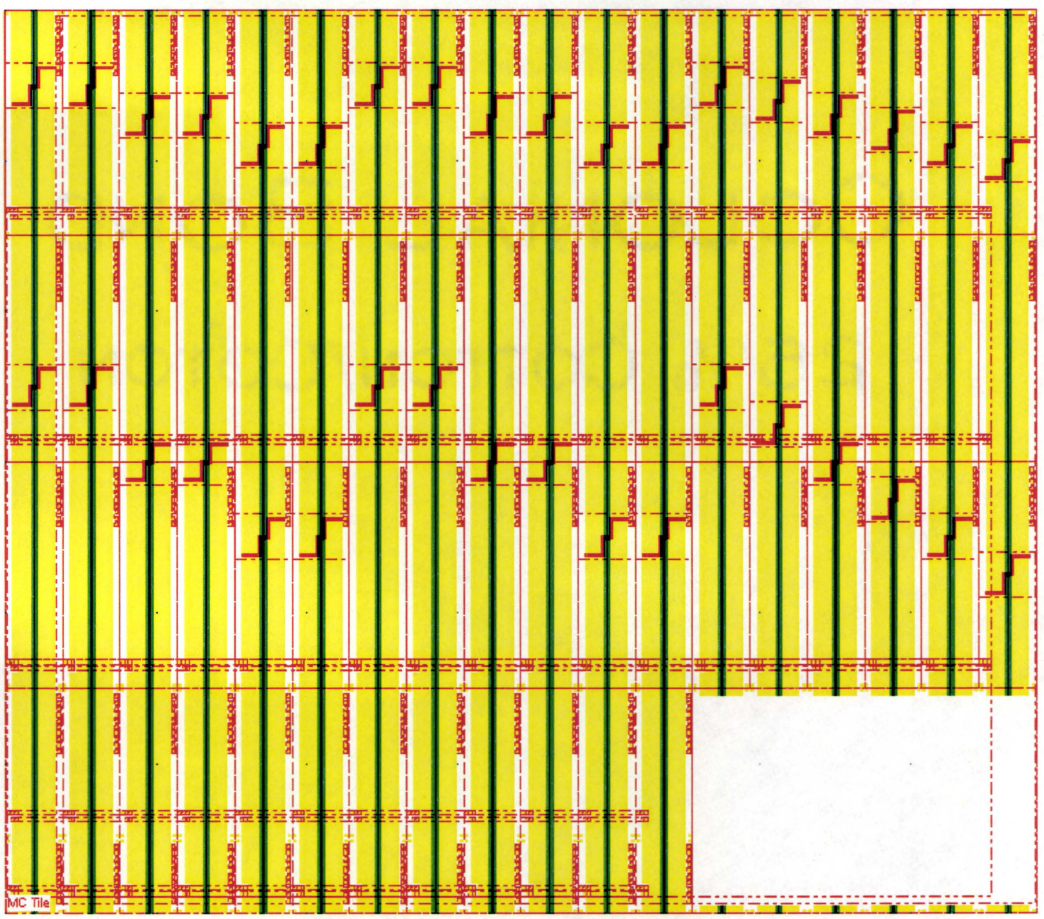

Figure B-1 Four layer optical mask for the two section coupled cavity laser.

Appendix C

The transfer matrix parameters for angled facets are developed here. $\tau_0(\theta)$ is the coupling coefficient of two interacting beams with an angular misalignment and the same waist size.

$$r_{pq}^{\theta_{i1}} = \frac{n_p \cos(\theta_{i1}) - n_q \cos(\theta_t')}{n_p \cos(\theta_{i1}) + n_q \cos(\theta_t')};$$

$$t_{pq}^{\theta_{i1}} = \frac{2n_p \cos(\theta_{i1})}{n_p \cos(\theta_{i1}) + n_q \cos(\theta_t')};$$

$$\theta_4 = 2 \times \theta_{i1};$$

$$\theta_5 = \theta_t' + \theta_i;$$

$$A_{11}^3 = 1/\left(t_{12} \times \tau_o\left(\theta_t - \theta_{x,y}\right)\right);$$

$$A_{12}^3 = -r_{21}\tau_o\left(\theta_{i1} - \theta_{x,y}\right)A_{11}^3;$$

$$A_{21}^3 = r_{12}\tau_o\left(2\theta_{x,y}\right)A_{11}^3;$$

$$A_{22}^3 = t_{21}\ \tau_o(\theta_5) - r_{12}r_{21}\ \tau_o\left(2\theta_{x,y}\right)\tau_o\left(\theta_{i1} - \theta_{x,y}\right)A_{11}^3;$$

$$A_{21}^5 = r_{32}\ \tau_o\left(\theta_{i1} - \theta_{x,y}\right)A_{11}^5;$$

$$A_{11}^5 = 1/\left(t_{23}\ \tau_o(\theta_5)\right);$$

$$\tau_o(\theta) = \sqrt{\tau_x \tau_y} \times \exp[-(\theta_x / \theta_{e,x})^2 (\theta_y / \theta_{e,y})^2];$$

$$\theta_{e,x} = \frac{\sqrt{2}}{\pi \tau_x [(\omega_{ox} / \lambda)^2 + (\omega_x / \lambda)^2]^{1/2}}$$

$$A_{22}^5 = t_{32} \tau_o(\theta_t - \theta_{x,y}) - r_{32} r_{23} \tau_o(2\theta_{x,y}) \tau_o(\theta_{i1} - \theta_{x,y}) A_{11}^5;$$

$$A_{12}^5 = -r_{32} \ \tau_o(2\theta_{x,y}) A_{11}^5;$$

Appendix D

Sample code for below threshold model:

```
function cleaved_dev_fit_new

clear all;

%% Reading measured data from text file %%

[x,I]=textread('below_th_10_30.txt', '%10f %8f');

%'headerlines', 1);
scale=0.001;
loop_step=1;
% defining start and finish of wavelength range for the simulation
wl_start = 1.609943;
wl_end = 1.640015;
%wl_start = 1.540000;
%wl_end = 1.674973;
%lambda_data =x';
lambda_data = x'.*1e-3;
lambda_data = chop(lambda_data,7);
```

```
D1 = diff(lambda_data);

step= sum(D1)/(length(lambda_data)-1);

int_data_log = I';

int_data_lin= 10.^(int_data_log./10);

Npts= round((wl_end-wl_start)/step);

index = find(lambda_data == wl_start);

lambda_data_fin= lambda_data(index(1):index(1)+Npts-1);

%int_data_fin = int_data_log(index(1):index(1)+Npts-1);

int_data_fin = int_data_lin(index(1):index(1)+Npts-1);

ad_conv=1000;

lambda = min(lambda_data_fin)-
ad_conv*step:step:max(lambda_data_fin)+ad_conv*step;

NL=length(lambda_data_fin);

%L2_tmp = L2;

lambda_o=1.58;

k= ((2*pi)./lambda);

max_k= max(k);

min_k=min(k);

k_o = 2*pi/lambda_o;

theta=4.0;

L1=390.2475;

L1_tmp = L1;

theta_i= pi*theta/180;

d = 1.5695;
```

```
a=[d,theta_i];

[int_final,I_right]=get_int(a,lambda,k,lambda_o,step,int_data_fin,ad_conv,NL,lam
bda_data_fin,L1_tmp,theta);

figure(2)

plot(lambda_data_fin,int_final)

hold on;

plot (lambda_data_fin, int_data_fin,'r')

hold off;

xlabel('Wavelength (\mum)')

ylabel('Intensity (a.u.)')

legend('Fit data','Measurement data')

grid on;

axis tight;


%% saving data


poo=lambda_data_fin;

boo=int_final;

too= [poo;boo];


%int_final

fid11= fopen('data11.txt','wt');

fprintf(fid11,'%2.6f        %2.10f \n',too);

fclose(fid11);
```

```
zoo=[lambda_data_fin;int_data_fin];
fid12= fopen('data12.txt','wt');
fprintf(fid11,'%2.6f       %2.10f \n',zoo);
fclose(fid12);
%% end of saving data %%

%% start of Marquardt algorithm %%
%% calculation of the initial chi-square values %%%
%int_data_fin(1:100)
chi_sq= sum((int_final-int_data_fin).^2);
chi_sq_old=chi_sq;
delta_chi_sq = chi_sq;

%% start of while block %%

num = 0;

while abs(delta_chi_sq)>1e-5*abs(chi_sq_old) & num <2
   num
   a
   %delta_chi_sq
    da = a./1000;
   for pp=1 :length(a)
      if (a(pp) == 0)
```

```
        da(pp)=0.001;
      end
    end
  ahigh = a;

  for kk=1:length(a)

     ahigh(kk)=a(kk)+da(kk);

int_final,I_right]=get_int(a,lambda,k,lambda_o,step,int_data_fin,ad_conv,NL,lamb
da_data_fin,L1_tmp,theta);

     I1= int_final;

[int_final,I_right]=get_int(ahigh,lambda,k,lambda_o,step,int_data_fin,ad_conv,NL,
lambda_data_fin,L1_tmp,theta);
     I2 = int_final;

     dR(kk,1:NL)= (I2-I1)./da(kk); % derivative with respect to a(k)
     Beta(kk)=sum((int_data_fin-I1).*dR(kk,: ));
  end  % calculation of Beta, dR, I1 and I2

  %% calculation of alpha matrix
  alpha0 = zeros(length(a));
```

```
for p=1:length(a)
   for jj=1:length(a)
      for LL=1:NL
         alpha0(p,jj)=alpha0(p,jj)+dR(p,LL)*dR(jj,LL);
      end
   end
end

%% increasing the diagonal terms of the curvature matrix alpha by a
%% factor (1+scale)
  alpha=alpha0./4.95e-13;

[chi_sq_dA,delta,newa]=chisqaredA(a,alpha,Beta,scale,loop_step,lambda,k,lamb
da_o,step,int_data_fin,ad_conv,NL,lambda_data_fin,L1_tmp,theta);



a= newa;
%[int_final,gpts,conv_out,I_left]=
get_int(a,lambda,k,lambda_o,step,int_data_fin,ad_conv);


%chi_sq_dA= sum((int_data_fin-int_final).^2)
 chi_sq
 %cc=chi_sq_dA
 %newa
 while chi_sq_dA >chi_sq
```

```
    if scale >1000
       warning('Bad Fitting !!?? ')
       break
    end
    scale = 10*scale;

[chi_sq_dA,delta,newa]=chisqaredA(a,alpha,Beta,scale,loop_step,lambda,k,lamb
da_o,step,int_data_fin,ad_conv,NL,lambda_data_fin,L1_tmp,theta);
    a= newa;
    chi_sq_dA;
 end

 %a= a+loop_step*delta;
 scale = max(scale/10,1e-5);
 chi_sq=chi_sq_dA;
 chi_sq_old
 delta_chi_sq=(chi_sq-chi_sq_old) %% difference between the chi_sqare of this
loop and the last loop.
 chi_sq_old= chi_sq;
 num=num+1;

end %% end of outer while loop
format long
a;
```

```
[int_final,I_right]=get_int(a,lambda,k,lambda_o,step,int_data_fin,ad_conv,NL,lam
bda_data_fin,L1_tmp,theta);%[lamb_final,int_final,gpts,conv_lambda, conv_out,
I_left,norm_gauss,conv_pts]= get_int(a,
lambda,k,lambda_o,kpts,step,max_kpts,min_kpts,m,wl_start,wl_end,step1,PP,int
_data_fin);


figure(5)

plot(lambda_data_fin,int_data_fin,'r')

hold on;

plot(lambda_data_fin,int_final)

hold off;

grid on;

axis tight;



%% ----------------------------------------

function
[int_final,I_right]=get_int(a,lambda,k,lambda_o,step,int_data_fin,ad_conv,NL,lam
bda_data_fin,L1_tmp,theta);


miu=0;

d = 1.5695;

L1=390.2475;

L2=969.00011-3.4834+1.60643;


% this if else make the L1 +L2 constant
```

```
%if (L1 > L1_tmp)
   %L2= L2-(L1-L1_tmp);
   %else if (L1 < L1_tmp)
      %L2= L2 + (L1_tmp - L1);
      %end
      %end

R_seg = 0.55;

d_active = 0.55;
ridge_width= 2.8;

%% ------------------------index of refraction ----------------------------%%
n_gr_temp=3.494885;
n_shift = 0.007;
lambda_start= 1.649;
%n_shift = 0.068;
n_shift1 = 0.32;
n_shift2 = 0.32;
n_gr= n_gr_temp-(lambda-lambda_start).*n_shift-((lambda-
lambda_start).*n_shift1).^2 - ((lambda-lambda_start).*n_shift2).^3;

%%------------------------- end of index of refraction-------------------------- %%
```

```
%% gain profile calculation %%

lambda_p2 = 1.615;

lambda_p1 = 1.6232;

g_p1 = 0.00062995963637590;

g_p2 = 0.000406949374023;

delta_g_p= 0.6;

G_o1= 2.70313396673466;

G_o2 = 1.71141019459888;

G_o3= 3.95867646938180;

G_o4= 3.72096728646676;

G_o5 = 1.70513636890811;

G_o6 = 1.77587370522309;

G_o7= 0.87477752469995;

G_o8= 3.18546073842266;

g_m1 = (g_p1 - ((lambda_p1 - lambda)./G_o1).^2-((lambda_p1 -
lambda)./G_o2).^3-((lambda_p1 - lambda)./G_o3).^4-((lambda_p1 -
lambda)./G_o4).^5);

g_m2 = (g_p2 - ((lambda_p2 - lambda)./G_o5).^2-((lambda_p2 -
lambda)./G_o6).^3-((lambda_p2 - lambda)./G_o7).^4-((lambda_p2 -
lambda)./G_o8).^5);
```

```
%%------------------- end of gain calculation ----------%%

%%------------------- sponteneous emission profile calculation --%%

B1=2.1062e-8;
B2=4.9962e-7;

 % Calculates the effective transmission and effective reflective
% coeffecient (s11 and s12)

% sponteneous emission profile- its a bit blue shifted from gain peak and
% also a bit higher in magnitude than gain peak
G_o9= 0.01;
G_10 = 5.5;
G_11= 5.5;
G_12= 5.5;

G_13 = 0.01;
G_14 = 3.8;
G_15= 3.8;
G_16= 3.8;

delta_lambda = 0.55;
```

```
lambda_sp1 = lambda_p1- delta_lambda;

lambda_sp2 = lambda_p2- delta_lambda;


sp_1= g_p1.*delta_g_p;

sp_2= g_p2.*delta_g_p;


%spont_1 = (sp_1 - ((lambda_sp1 - lambda)./G_o9).^2);%-((lambda_sp1 -
lambda)./G_10).^3-((lambda_sp1 - lambda)./G_11).^4-((lambda_sp1 -
lambda)./G_12).^5);

%spont_2 = (sp_2 - ((lambda_sp2 - lambda)./G_13).^2);%-((lambda_sp2 -
lambda)./G_14).^3-((lambda_sp2 - lambda)./G_15).^4-((lambda_sp2 -
lambda)./G_16).^5);


spont_1=sp_1./(1+((lambda_sp1-lambda).^2)./abs((max(lambda)-min(lambda))));

spont_2=sp_2./(1+((lambda_sp2-lambda).^2)./abs((max(lambda)-min(lambda))));


%% ---------- end of spontemeous emission profile ---------- %%


%% ---------- calculation of sponteneous emission ----------  %%


G1= exp(g_m1.*L1);

G2= exp(g_m2.*L2);

Bm1= B1.*(spont_1./sp_1);

Bm2= B2.*(spont_2./sp_2);

beta =3.6e-4;
```

```
delta1 = sqrt((beta.*Bm1.*(G1-1))./g_m1);
delta2 = sqrt((beta.*Bm2.*(G2-1))./g_m2);

%% ---------- end of sponteneous emission calculation ---------- %%

%% defining end reflectivityies and transmission co-effs %%
n_l_1 = -g_m1./(2.*k);
n_l_3 = -g_m2./(2.*k);

%g = j*k_o*n_l;
n1 = n_gr+j*n_l_1;
n3 = n_gr+j*n_l_3;
n2=1;

%ng1=g_m1(1:100)
%ng2=g_m2(1:100)

%theta_i= pi*theta/180;
theta_t=(asin(real(n1).*sin(a(2)))./real(n2));
theta_i_1=theta_t-2*a(2);
theta_t_prime=asin((n2.*sin(theta_i_1))./real(n1));
theta_5=theta_t_prime+a(2);

%plot(lambda, n3)
```

```
r_01_tmp=(1-(n1))./((n1)+1);

r_12_tmp=((n1).*cos(a(2))-n2.*cos(theta_t))./((n1).*cos(a(2))+n2.*cos(theta_t));

r_21_tmp=(((n2.*cos(theta_i_1))-
((n1).*cos(theta_t_prime)))./((n2.*cos(theta_i_1))+((n1).*cos(theta_t_prime))));

r_23_tmp=(((n2.*cos(theta_i_1))-
((n3).*cos(theta_t_prime)))./((n2.*cos(theta_i_1))+((n3).*cos(theta_t_prime))));

r_32_tmp=((n3).*cos(a(2))-n2.*cos(theta_t))./((n3).*cos(a(2))+n2.*cos(theta_t));

r_34_tmp=((n3)-1)./((n3)+1);

%(2.*real(n2).*cos(theta_i_1))./((real(n2).*cos(theta_i_1))+(n3.*cos(theta_t_prime
)));

r_01= (r_01_tmp.*R_seg)./abs(r_01_tmp);

r_34= (r_34_tmp.*R_seg)./abs(r_34_tmp);

%r_01=r_01_tmp;

r_12=r_12_tmp;

r_21=r_21_tmp;

r_23=r_23_tmp;

r_32=r_32_tmp;


t_01= 1.0.*(1+r_01);

t_12= (2.*real(n1).*cos(a(2)))./(real(n1).*cos(a(2))+n2.*cos(theta_t));

t_21=
(2.*real(n2).*cos(theta_i_1))./((real(n2).*cos(theta_i_1))+(n1.*cos(theta_t_prime))
);

t_23= (2.*n2.*cos(theta_i_1))./(n2.*cos(theta_i_1)+real(n3).*cos(theta_t_prime));

t_32= (2.*real(n3).*cos(a(2)))./(real(n3).*cos(a(2))+n2.*cos(theta_t));
```

```
t_34= 1.0.*(1+r_34);

t_01=1.*t_01;

r_01=1.0*r_01;

%t_34=1.1.*t_34;


%% parameters of the angled facet interface matrices %%


%% beam spot calculation %%

%far_field_theta=20*pi/180;

omega_o_x= 0.5*d_active+0.14.*sqrt(lambda)./d_active; %% beam waist in
growth direction of x-y plane

omega_o_y= 0.5*ridge_width+0.14.*sqrt(lambda)./ridge_width;%% beam waist in
ridge width direction


x=a(1);


omega_x_air=omega_o_x.*sqrt(1+((2.*x)./(k.*omega_o_x.^2).^2));%%

omega_y_air=omega_o_y.*sqrt(1+((2.*x)./(k.*omega_o_y.^2)).^2);%% beam
waist in ridge width direction

R_x=x.*(1+(k.*omega_o_x.^2./(2.*x)).^2);

R_y=x.*(1+(k.*omega_o_y.^2./(2.*x)).^2);


tau_d_x=
2./(sqrt(((omega_o_x./omega_x_air)+(omega_x_air./omega_o_x)).^2+(2./(k.*ome
ga_o_x.*omega_x_air).^2.*x.^2)));
```

```
tau_d_y=
2./(sqrt(((omega_o_y./omega_y_air)+(omega_y_air./omega_o_y)).^2+(2./(k.*ome
ga_o_y.*omega_y_air).^2.*x.^2)));

tau_d=sqrt(tau_d_x.*tau_d_y);


theta_1=theta_t-a(2);

[tau_o]=get_tau(lambda,omega_o_x,omega_o_y,theta_1);

tau_o_2_theta_t_theta=tau_o.*1.00;

theta_3=2*a(2);

[tau_o]=get_tau(lambda,omega_o_x,omega_o_y,theta_3);

tau_o_2_theta_i= tau_o.*1.2;

theta_2= theta_i_1-a(2);

[tau_o]=get_tau(lambda,omega_o_x,omega_o_y,theta_2);

tau_o_theta_i_1_theta=tau_o.*0.9;

[tau_o]=get_tau(lambda,omega_o_x,omega_o_y,theta_5);

tau_o_theta_5=tau_o.*1.00;

T333= t_21.*tau_o_theta_5-
((r_12.*tau_o_2_theta_i.*r_21.*tau_o_theta_i_1_theta)./(t_12.*tau_o_2_theta_t_t
heta));

T555= t_32.*tau_o_2_theta_t_theta-
((r_32.*tau_o_2_theta_i.*r_23.*tau_o_theta_i_1_theta)./(t_23.*tau_o_theta_5));


%%%%%%%end of angled facet matrix
parameters%%%%%%%%%%%%%%%%%%%%

%plot(lambda, theta_2)
```

```
%%%% transfer matrices including cavities and interfaces %%


for iter=1:length(lambda)


   A7=[1/t_01(iter), r_01(iter)/t_01(iter),0;r_01(iter)/t_01(iter),1/t_01(iter),0;0,0,1];

   A6 =[exp(-j*k(iter)*n1(iter)*L1), 0, -delta1(iter);
0,exp(j*k(iter)*n1(iter)*L1),delta1(iter);0,0,1];

   A5=[1/(t_12(iter)*tau_o_2_theta_t_theta(iter)), -
r_21(iter)*tau_o_theta_i_1_theta(iter)/(t_12(iter)*tau_o_2_theta_t_theta(iter)),0;r_
12(iter)*tau_o_2_theta_i(iter)/(tau_o_2_theta_t_theta(iter)*t_12(iter)),T333(iter),0;
0,0,1];

   A4=[exp(j*k(iter)*x)/tau_d(iter),0,0;0,exp(-j*k(iter)*x)*tau_d(iter),0;0,0,1];

   A3=[1/(t_23(iter)*tau_o_theta_5(iter)), -
r_32(iter)*tau_o_2_theta_i(iter)/(t_23(iter)*tau_o_theta_5(iter)),0;r_23(iter)*tau_o
_theta_i_1_theta(iter)/(t_23(iter)*tau_o_theta_5(iter)),T555(iter),0;0,0,1];

   A2=[exp(-j*k(iter)*n3(iter)*L2), 0, -delta2(iter);
0,exp(j*k(iter)*n3(iter)*L2),delta2(iter);0,0,1];

   A1= [1/t_34(iter), r_34(iter)/t_34(iter),0;r_34(iter)/t_34(iter),1/t_34(iter),0;0,0,1];

   Af1=A2*A1;

   Af2=A3*Af1;

   Af3=A4*Af2;

   Af4=A5*Af3;

   Af5=A6*Af4;

   Af6=A7*Af5;


   Af11=A5*A4;
```

```
    Af22=Af11*A3;

    E_right(iter)=-Af6(1,3)/Af6(1,1);
    E_left(iter)=-Af6(2,1)*E_right(iter)+Af6(2,3);

 %% S parameters for the air gap matrix %%

    S11(iter)=Af22(2,1)/Af22(1,1);
    S12(iter)=1/Af22(1,1);
    S22(iter)=-Af22(1,2)/Af22(1,1);
    S21(iter)=(Af22(1,1)*Af22(2,2)-Af22(1,2)*Af22(2,1))/Af22(1,1);
end
I_right=abs(E_right).^2;%-0.15e-6;
I_left=abs(E_left).^2;

S11_abs=abs(S11).^2;
S12_abs=abs(S12).^2;
S21_abs=abs(S21).^2;
S22_abs=abs(S22).^2;

loss=1-S12_abs-S11_abs;
k_o= 2.*pi./lambda_o;
b_prop= (n1.*k_o)-j.*-g_m1./2;
```

```
t1=exp(2.*j.*b_prop.*L1);

%% calculation of effective reflectivity %%

R_eff= S22+(r_01.*t1.*S12.*S21)./(1-r_01.*t1.*S11);
R_eff=abs(R_eff);



%% convolution of the OSA response function with the spectral output%%
%% of the model%%

gpts= -50*step:step:50*step;
sigma = 0.07e-3/3.354;
gauss = 1/(sigma*sqrt(2*pi)).*exp(-((gpts-miu).^2)./(2*sigma.^2));
gs_sum = sum(gauss);
norm_gauss = gauss./gs_sum;
pp= sum(norm_gauss);
GL= length(gpts);
conv_out = conv(norm_gauss,I_right);
conv_length = length(conv_out);
index1=((GL-1)/2)+1+ad_conv;
index2= index1+length(int_data_fin)-1;
int_final= conv_out(index1:index2);
int_final= int_final+0.1e-6;
```

```
%int_final=conv_out((GL-1)/2+length(lambda)-1+1:


%int_final=conv_out((GL-1)/2+length(lambda)-1+1:


function
[chi_sq_dA,delta,newa]=chisqaredA(a,alpha,Beta,scale,loop_step,lambda,k,lamb
da_o,step,int_data_fin,ad_conv,NL,lambda_data_fin,L1_tmp,theta);


for mm=1:length(a)

   alpha(mm,mm)= (1+scale)*alpha(mm,mm);

end

delta= Beta*inv(alpha);

newa= a+loop_step*delta;

[int_final,I_right]=get_int(newa,lambda,k,lambda_o,step,int_data_fin,ad_conv,NL,
lambda_data_fin,L1_tmp,theta);


%chi_sq_dA = sum(((int_final-int_data_fin).^2)./(1e-12+int_data_fin.^2));

%chi_sq_dA=sum(((int_final-int_data_fin).^2).*(exp((-int_data_fin)./(0.2e-6))));

chi_sq_dA =sum((int_final-int_data_fin).^2);

sigma_sq=(((sum(int_final-int_data_fin).^2)/(length(int_final)-1)));


inv(alpha);

diag_inv_alpha=(diag(inv(alpha)));

uncert=sqrt(diag_inv_alpha)
```

```
%% function calculating the coupling efficiency between two interacting beams
%%


function [tau_o]=get_tau(lambda,omega_o_x,omega_o_y,theta);


theta_e_x= sqrt(2)./(pi.*sqrt((omega_o_x./lambda).^2 +
(omega_o_x./lambda).^2));

theta_e_y= sqrt(2)./(pi.*sqrt((omega_o_y./lambda).^2 +
(omega_o_y./lambda).^2));

tau_o= exp(-(((theta./theta_e_x).^2).*((theta./theta_e_y).^2)));
```

References

[1] Khan, F. K. and Cassidy D. T.: "*Widely tunable coupled cavity semiconductor laser*", Appl. Opt, 48(19), pp. 3809-3817, 2009.

[2] Khan, F. K., Wang, Jingcong and Cassidy, D. T.: "*Coupled cavity InGaAsP/InP laser for synthetic optical coherence tomography and other applications*", Institution of Engineering and Technology (IET) Optoelectron, 4(1), pp. 25-35, Feb, 2010.

[3] Basting, D., Pippet, K. and Stamm, U.: "*History and future prospects of excimer laser technology*," Int. symposium on laser precision and micro fabrication, pp. 14-22, 2001.

[4] Patel, C. K. N.: "*Continuous wave laser action on vibrational-rotational transitions of $C0_2$*," Phys. Rev., 136(5A), pp. 1187-1193, 1964.

[5] Brau, C.: "*Free-Electron Lasers*," Academic Press, Boston, 1990.

[6] Schäfer, F.P and. Drexhage, K. H.: "*Dye Lasers,*" 2nd rev. ed., vol. 1, Berlin ; New York: Springer-Verlag, 1977

[7] Hecht, J.: "*The Laser Handbook*," 2nd ed., Ch. 24, New York, McGraw-Hill, 1992.

[8] Amann, M. C. and Buus, J.: "*Tunable Laser Diodes*," Artec House, Boston, 1998.

[9] Koch, T. L. and Koren, U.: "*Semiconductor lasers for coherent optical fiber communications*," IEEE J. Lightwave Technol., 8, pp. 171-177, 1991.

[10] Dummer, M. M., Klamkin, J., Pedretti, T. A. and Coldren, L. A.: "*40 GB/s field-modulated wavelength converters for all-optical packet switching*", IEEE J. Select. Topics in Quantum Electron., 15 (3), pp. 494-503, 2009.

[11] Wree, C., Mohr, D., Becker, D. and Joshi, A.: "*Coherent optical receiver with widely tunable local oscillator*", Proc. SPIE, 6527, pp. 6572041-6572048, 2007

[12] Hanumegowda, N. M.: "*Development of label-free microsphere optical resonator bio/chemical sensor*" Proc. of the SPIE, Int. Soc. for Opt. Eng., 6004(1), pp. 6004011-12, 2005.

[13] Winneswisser, G., Drascher, T., Giesen, T., Pak, I., Schmulling, F. and Schieder, R.: "*The tunable diode laser; A versatile spectroscopic tool*", Spectrochemica Acta Part A: Molecular and Biomolecular Spectroscopy, 55(10), pp. 2121-2142, 1999.

[14] Enshasy, H. M. and Cassidy D. T.: "*Sub-micrometer distance measurements with a broadly tunable short- external- cavity InGaAsP/InP diode laser*", Institution of Engineering and Technology (IET) Optoelectron., 1(4), pp. 157-162, 2007.

[15] Gordon, E. I.: "*Optical maser oscillators and noise*", Bell Systems Tech. J., 43, pp. 507-539, 1964.

[16] Cassidy, D. T.: "*Analytic description of a homogeneously broadened injection laser*", IEEE J. Quantum Electron., 20(8), pp. 913-918, 1984.

[17] Delorme, F.: "*Widely tunable 1.55-μm lasers for wavelength- division-multiplexed optical fiber communication*," IEEE J. Quantum Electron., 34(9), pp. 1706-1716, 1998.

[18] Crowe, J. W. and Craig, R.M. Jr.: "*GaAs linewidth measurements by heterodyne detection*," Appl. Phys. Lett., 5(4), pp. 72-74, 1964.

[19] Salathe, R. P.: "*Diode lasers coupled to external resonators*", Appl. Phys. 20, pp. 1-18, 1979.

[20] Edmonds, H. D. and Smith, A. W.: "*Second-harmonic generation with the GaAs laser*", IEEE J. Quantum Electron., 6, pp. 356, 1970.

[21] Cassidy, D. T. and Hamp, M. J.: "*Diffractive optical element used in external feedback configuration to tune the wavelength of uncoated Fabry-Perot diode laser*", J. Modern Opt. 46, pp. 1071-1078, 1999.

[22] Uneishi, U. H. and Katagiri, Y.: "*Application of an extremely short strong-feedback configuration of an external-cavity laser diode system fabricated with GaAs-based integration technology*," Appl. Opt., 33, pp. 5557-5563, 1994.

[23] Berger, J. D., Zhang, Y., Grade, J. D., Lee, H., Hrinya, S., Jerman, H., Al Fennema, A., Tselikov, A. and Anthon, D.: "Widely *tunable external cavity diode laser using a MEMS electrostatic rotary actuator*," in Proc. LEOS, Summer Topic Meet., Copper Mountain, Co, USA, pp. 41-42, 2001.

[24] Pedrotti, F. L. and Pedrotti, L. S.: "*Introduction to Optics*," Ch. 20, Prantice hall, New Jersey, 1987.

[25] Liu, A. Q. and Zhang, X. M.: "*A review if MEMS external-cavity tunable lasers*," J. Micromech. and Microeng., 17, pp. 1-13, 2007.

[26] Connie J. Chang-Hasnain: "*Tunable VCSEL*," IEEE J. on Select. topics in J. Quantum Electron., 6(6), pp. 978-987, 2000.

[27] Chase, C., Zhou, Y., Huang, M.C.Y. and Chang-Hasnain, C.J.: "*NEMO Tunable VCSEL using Ultra Compact High Contrast Grating for High Speed Tuning,*" IEEE 21st Int. Semiconductor Laser Conf., Sorrento, Italy, pp. 161-162, 2008.

[28] Brerger, A.D., Drake J. D., Dutta, S., Fennema, A., Grade, J.D., Hrinya, S., Ilkov, F., Jerman, H., King, D., Lee, H., Tselikov, A. and Yasumura, K.: *"External cavity diode lasers tuned with silicon MEMS,"* Proc. OFC, Opt. Fiber Communication Conf., Exhibit, Anaheim, CL, USA, pp 97–98, 2002.

[29] Buus, J., Amann, M. and Blumenthal D. J.: "*Tunable Laser Diodes and related optical sources,*" Ch. 4, Wiley-Interscience, 2005.

[30] Bennet, B. R., Soref, R. A. and Alamo, J. A. D.: "*Carrier-Induced change in refractive index of InP, GaAs, and InGaAsP*", IEEE J. Quantum Electron., 26(1), pp. 113-122, 1990.

[31] Thomson, G. H. B.: "*Physics of Semiconductor Laser Devices,*" Chichester, U.K., Wiley, 1980.

[32] Kotaki, Y., Ogita, S., Matsude, M., Kuwahara, Y. and Ishikawa, H.: "*Tunable narrow-linewidth and high power λ/4 shifted DFB laser,*" Electron. Lett., 25, pp. 990-992, 1989.

[33] Chinen, C., Gen-ei, K., Suhara, H., Tanaka, A., Matsuyama, T., Konno, K. and Toshiba, Y. M.: "*Low- threshold 1.55μm InGaAsP/InP buried heterostructure distributed feedback lasers*," Appl. Phys. Lett., 51, pp.273-275, 1987.

[34] Natakeyama, N., Naniwae, K., Kudo, K., Suzuki, N., Sudo, S., Muroya, Y., Yashiki, K., Satoh, S., Morimoto, T., Mori, K. and Sasaki, T.: "*Wavelength-selectable microarray light sources for S, C, and L –band WDM systems*," IEEE Photon. Technol. Lett., 15, 903-905, 2003.

[35] Heanue, J., Vail, E., Sherback, M. and Pazeshki, B.: "*Widely tunable laser module using DFB array and MEM's selection with internal wavelength locker*," in Proc. OFC, 1, pp. 82-83, 2003.

[36] Yu, Y., and O'Dowd, R.: "Influence of mode competition on the fast wavelength switching of an SG-DBR laser", J. Lightwave Technol., 20, pp. 700-704, 2002.

[37] Manger, H. and Rothe, H.: "*Selection of axial modes in optical masers*", Phys. Lett., 7(5), pp. 330-331, 1963.

[38] Coldren, L. A. and Koch, T. L.: "*Analysis and design of coupled-cavity lasers-part 1: Threshold gain analysis and design guidelines*", IEEE J. Quantum Electron., 20(6), pp. 659-670, 1984.

[39] Tsang, W.T.: "*The Cleaved-Coupled-Cavity (C^3) lasers*", in Semiconductors and Semimetals, W. T. Tsang ed., (Academic, 1985) Vol. 22. Chap.5.

[40] Phelan, R. A., Wei-Hua, G., Qiaoyin, L., Byrne, D., Roycroft, B., Lambkin, P., Corbett, B., Smyth, F. , Barry, L. P., Kelly, B., O'Gorman, J., and Donegan, J. F.: "*A Novel Two-Section Tunable Discrete Mode Fabry-Perot Laser Exhibiting Nanosecond Wavelength Switching*", IEEE J. Quantum Electron., 44(4), pp.331-337, 2008.

[41] Muller, M., Bauer, A., Lehnherdt T. and Forchel, A.: "*Widely tunable photonic crystal coupled cavity lasers on GaSb*", IEEE Photon. Technol. Lett., 20(13), pp. 1100-1102, 2008

[42] Muller, M., Scherer, H., Lehnhardt, T., Rossner, K., M. Hummer, Werner, R. and Forchel, A.: "*Widely tunable coupled cavity lasers at 1.9μm on GaSb*", IEEE Photon. Technol. Lett., 29(8), pp. 592-594, 2007.

[43] Kononeko, V. K., Manak, L. S. and Nalivko, S. V.: "*Design and characteristics of widely tunable quantum-well lasers*", Spectrochimica Acta A. 55, pp. 2091–2096, 1999.

[44] Woodworth, S. C., Cassidy, D. T. and Hamp, M. J.: "*Experimental analysis of a broadly tunable InGaAsP laser with compositionally varied quantum wells*", IEEE J. Quantum Electron., 39(3), pp. 426-430, 2003.

[45] Trenado, N. and Palmier, J. F.: "*An efficient and accurate method for gain spectrum calculations in non-identical multiple quantum wells*", IEEE, J. Quantum Elect., 38, pp. 978-983, 2002.

[46] Morrison, G. B., Woodworth, S. C., Wang, H. and Cassidy, D. T.: "*Galerkin method for calculating valence band wavefunctions in quantum- well structures using exact envelope theory*", IEEE J. Quantum. Electron., 40 (3), 2004.

[47] Wang, H. and Cassidy, D. T.: "*Gain measurement of Fabry-Perot semiconductor lasers using a nonlinear least squares fitting method*", IEEE J. Quantum Electron., 41(4), pp. 532-540, 2005.

[48] Hamp, M. J. and Cssidy, D. T.: "*Experimental and theoretical analysis of carrier distribution in asymmetric multiple quantum-well InGaAsP lasers*", IEEE J. Quantum Electron., 37(1), pp. 92-99, 2001.

[49] Coldren, L. A., Furya, K., Miller, B. I. and Rentsheller, J. A.: "*Etched mirror and groove-coupled GaInAsP/InP laser devices for integrated optics*", IEEE J. Quantum Electron., 18(10), pp. 1679-1688, 1982.

[50] Bouchoule, S., Azouigui,S., Guilet, S., Patriarche, G., Largeau, L., Martinez, A., Gratiet, L. Lemaitre, G. and Lelarge, F. "*Anisotropic and smooth inductively coupled plasma etching of III-V laser waveguides using HBr-O2 chemistry*," J. Electrochem. Soc.,155(10), pp. 778-785, 2008.

[51] Rubanov, S. and Munroe, P. R.: "*Damage in III-V compounds during focused ion beam milling*," Microsc. Microanal., 11, pp. 446-455, 2005.

[52] Ren, Q., Zhang, B., Xu, J., Zhang, Z., Jin, Y. and Qian, D. Yu: "*Etched facet and semiconductor/air DBR facet of a AlGaInP laser diode prepared by focused ion beam milling*", Solid State Comm., pp. 130, 433-436, 2004.

[53] Khan, F. A., Zhou, L., Ping, A. T. and Adeside, I.: "*Inductively coupled reactive ion etching of $Al_xGa_{1-x}N$ for application in laser facet formation*", J. Vac. Sci. Tech. B, 17(6), 1999.

[54] Marinelli, C., Borodovsky, M., Sergeant, L. J., Gioannini, M., Rorison, J. M., Penty, R. V., White, I. H., Heard, P. J., Benyoucef, M., Kuball, M., Hasnain, G., Takeuchi T. and Schneider, R. P.: "*Design and performance analysis of deep-etch air/nitride distributed Bragg reflector gratings for AlInGaN laser diodes*", Appl. Phys. Lett., 79(25), pp. 4076-4078, 2001.

[55] Choi, H. K.: "*Analysis of Two-Section Coupled-Cavity semiconductor Lasers*", IEEE J. Quantum Electron., 20(4), pp. 385-393, 1984.

[56] Hamp, M.J. and Cassidy, D.T.: "*Critical design parameters for engineering broadly tuneable asymmetric multiple quantum-well lasers*", IEEE J. Quantum Electron., 36(8), pp. 978-983, 2000.

[57] Coldren, L. A. and Koch, T. L: "*Analysis and design of coupled-cavity lasers -- part I: Threshold gain analysis and design guidelines*," IEEE J. Quantum Elect., 20(6), pp. 659-670, 1984.

[58]Choi, H. K.: "*Analysis of two-section coupled-cavity semiconductor lasers*', IEEE J. Quantum Electron., 20(4), pp. 385-393, 1984.

[59] Lang, R.: "*Injection locking properties of a semiconductor laser*," IEEE J. Quantum Electron., 18(6), pp. 976-983, 1982.

[60] Coldren, L. A. and Corzine, S. W.: "*Diode Lasers and Photonic Integrated Circuits*", K. Chang eds., Wiley series in Microwave and Photonic Engineering, Ch. 3, 1995.

[61] Morrison, G. B. and Cassidy, D. T.: "*A probability-amplitude transfer matrix model for distributed feedback laser structures*", IEEE J. Quantum Electron., 36(9), pp. 633-640 2000.

[62] Joyce, W. B. and Deloach, B. C.: "*Alignment of Gaussian beams*", Appl. Opt., 23(23), pp. 4187-4196, 1984.

[63] Cassidy, D. T.: "*Analytic description of a homogeneously broadened injection laser*", IEEE J. Quantum Electron., 20 (4), pp. 913-918, 1984.

[64] Gnauck, P., Hoffrogge, P. and Schumann, M.: "*Introduction to Focused Ion Beams Instrumentation, Theory, Techniques and Practice*", Giannuzzi, L. A. and Stevie, F. A. eds., Springer US, Ch. 7, pp. 133- 142, 2005.

[65] Bevington, P. R. and Robinson, D. K.: "*Data Reduction and Error Analysis for Physical Sciences*," 2nd ed. New York: McGraw Hill, pp. 161-164, 1969.

[66]Fukushima, T. and Sakamoto, T.: "*Optical signal inverter using injection locking of coupled semiconductor lasers*", Japan. J. Appl. Phys, 36(3A), part 2, pp. 280-282, 1997.

[67] Cassidy, D. T.: "*Comparison of rate equation and Fabry-Perot approaches to modeling a diode laser*", Appl. Opt., 22(21), pp. 3321-3326, 1983.

[68] Griffiths, D. V. and Smith, I. M.: "*Numerical Methods for Engineers*", ch.7, First ed., CRC press, 1991.

[69] Kamatani, O. and Hotate, K.: "*Optical coherence domain reflectometry by synthesis of coherence function*", J. Lightwave Tech.,11, pp. 1701-1710, 1991.

[70] Huang, D., Swanson, E., Lin, C.P., Stinson, W.G., Chang, W., Hec, M.R., Hotte, T., Gregory, K., Puliafito, C.A. and Fujimoto, J.G.: "*Optical coherence tomography*", Science, 254, pp. 1178-1181, 1991.

[71] Yun, S. H., Tearney, G. J., Deboer, J. F., Iftimia, N. and Bouma, B. E.: "*High speed optical frequency domain imaging*", Opt. Express, 11 (22), pp. 2953-2963, 2003.

[72] Nassif, N., Cense, B., Hyle, P. B. and Yun, S. H.: "*In vivo retinal imaging by ultra high-speed spectral domain optical coherence tomography*", Opt., Lett., 29(5), pp. 480-482, 2004.

[73] Goodman, J. W.: "*Statistical Optics*", Ch. 5, Wiley, New York, 1985.

[74] Agrawal, A., Prakash, G., Jacob, S. and Kumar, D.A.: "*Fourier domain OCT scans faster reduces patient exam time*", Ocular surgery news, U.S. edition, Feb, 2009.

[75] Choma, M. A., Sarunic, M. V., Yang, C. and Izatt, J. A.: "*Sensitivity advantage of swept source and fourier domain optical coherence tomography*", Opt. Express, 11(18), pp. 2183-2189, 2003.

[76] He, Z. and Hotate, K.: '*Synthesized optical coherence tomography for imaging of scattering objects by use of a stepwise frequency-modulated tunable laser diode*', Opt. Lett., 24(21), 1999.

[77] Wang, J. and Cassidy, D.T.: "*Broadly tunable, short external cavity diode laser for optical coherence tomography*", IET. Optoelectron., 2 (1), pp. 46-54, 2008.

[78] Vandermeer, A. D and Cassidy, D.T.: "*Frequency response measurements for mirror image asymmetric multiple quantum well lasers*", IEEE J. Quantum Electron., 41(7), pp. 932-936, 2005.

[79] Schmitt, J. M.: 'Optical coherence tomography (OCT): A review', IEEE J. Sel. Topics in Quantum Electron., 5(4), pp. 1205-1215, 1999.

[80] Fercher, A. F., Drexler, W., Hitzenberger, C. K., and Lasser, T.: 'Optical coherence tomography-principles and applications', Reports on Prog. In Phys., 66, pp. 239-303, 2003.

[81] Jansson, P. A.: '*Deconvolution: with applications in spectroscopy*', Academic Press, INC, ch.3, pp. 67-92, 1984.

[82] Richardson, W. H.: '*Bayesian-based iterative method of image restoration*', J. Opt. Soc. Am., 62, pp. 55-59, 1972.

[83] Wang, J.: '*Asymmetric multiple quantum well light sources for optical coherence tomography*', Ph.D. thesis, Dept. of Eng. Phys., Mcmaster University, Ontario, Canada, 2008.

[84] Fouquet, J.E., Braun, D.M. and Trott, G.R.: '*Wavelength-dependant optimum output coupling enhanced performance of external-cavity-tuned semiconductor lasers at 1.5μm*', IEEE J. Quantum. Electron.,32, pp. 1777-1781, 1996.

[85] Ott, H. W.: 'Noise *reduction technique in electronic systems*', John Wiley & Sons, Ch.8, 1988.

[86] Tiziani, H. J., Franze, B. and Haible, P: '*Wavelength-shift speckle interferometry for absolute profilometry using a mode-hop free external cavity diode laser*', J. Mod. Opt.,44 (8), pp. 1485-1496,1997.